Defects in Colloidal Crystals

Identification, Characterization, and Manipulation

Defecten in Colloïdale Kristallen

Identificatie, Karakterisering en Manipulatie

(met een samenvatting in het Nederlands)

Proefschrift

ter verkrijging van de graad van doctor aan de Universiteit Utrecht
op gezag van de rector magnificus, prof.dr. G.J. van der Zwaan,
ingevolge het besluit van het college voor promoties
in het openbaar te verdedigen op

vrijdag 27 januari 2012

des ochtends te 10.30 uur

door

Jan Hilhorst

geboren op 10 november 1982 te Haarlem

Promotor:　　Prof. dr. H. N. W. Lekkerkerker

Co-promotor:　Dr. A. V. Petukhov

Contents

List of Publications

This thesis is based on the following publications:

Chapter 2:
- D. V. Byelov, J. Hilhorst, A. B. G. M. Leferink op Reinink, I. Snigireva, A. Snigirev, G. B. M. Vaughan, G. Portale, A. V. Petukhov; *Diffuse Scattering in Random-Stacking Hexagonal Close-Packed Crystals of Colloidal Hard Spheres,* Phase Transit., **2010**, *83*, 107.

Chapter 3:
- J. Hilhorst, V. V. Abramova, A. Sinitskii, N. A. Sapoletova, K. S. Napolskii, A. A. Eliseev, D. V. Byelov, N. A. Grigorieva, A. V. Vasilieva, W. G. Bouwman, K. Kvashnina, A. Snigirev, S. V. Grigoriev, A. V. Petukhov; *Double Stacking Faults in Convectively Assembled Crystals of Colloidal Spheres*, Langmuir, **2009**, *25*, 10408–10412.

Chapter 4:
- M. M. Van Schooneveld, J. Hilhorst, A. V. Petukhov, T. Tyliszczak, J. Wang, B. M. Weckhuysen, F. M. F. De Groot, E. De Smit; *Scanning Transmission X-Ray Microscopy as a Novel Tool to Probe Colloidal and Photonic Crystals,* Small, **2011**, *7*, 804.

Chapter 5:
- J. Hilhorst, M. M. van Schooneveld, J. Wang, E. de Smit, T. Tyliszczak, J. Raabe, A. P. Hitchcock, M. Obst, F. M. F. de Groot *and* A. V. Petukhov; *Three Dimensional Structure and Defects in Colloidal Photonic Crystals Studied with Tomographic Scanning Transmission X-ray Microscopy,* Submitted.

Chapter 6:
- J. Hilhorst and A. V. Petukhov, *Variable Dislocation Widths in Colloidal Crystals of Soft Thermosensitive Spheres,* Phys. Rev. Lett., **2011**, 107, 095501.

Chapter 7:
- J. Hilhorst, J. R. Wolters, A. V. Petukhov; *Slanted Stacking Faults and Persistent Face Centered Cubic Crystal Growth in Sedimentary Colloidal Hard Sphere Crystals*, CrystEngComm, **2010**, *12*, 3820–3826.

Chapter 8:
- J. Hilhorst, J. R. Wolters, D. A. M. de Winter, J. A. Post, A. V. Petukhov; To be Submitted.

Other publications by the author:

- D. J. Kraft, J. Hilhorst, M. A. P. Heinen, M. J. Hoogenraad, B. Luigjes, W. K. Kegel; *Patchy Polymer Colloids with Tunable Anisotropy Dimensions*, J. Phys. Chem. B, **2011,** 115, 7175.

- J. Gulden, O. M. Yefanov, A. P. Mancuso, V. V. Abramova, J. Hilhorst, D. Byelov, I. Snigireva, A. Snigirev, A. V. Petukhov, I. A. Vartanyants; *Coherent x-ray imaging of defects in colloidal crystals,* Phys. Rev. B, **2010**, 81, 224105.

- M. M. van Schooneveld, D. P. Cormode, R. Koole, J. T. van Wijngaarden, C. Calcagno, T. Skajaa, J. Hilhorst, D. C. 't Hart, Z. A. Fayad, W. J. M. Mulder, *A. Meijerink; A fluorescent, paramagnetic and PEGylated gold/silica nanoparticle for MRI, CT and fluorescence imaging,* Contrast Media Mol. I., **2010,** 5, 231.

- S. Mayilo, J. Hilhorst, A. S. Susha, C. Hoehl, T. Franzl, T. A. Klar, A. L. Rogach, J. Feldmann; *Energy Transfer in Solution-Based Clusters of CdTe Nanocrystals Electrostatically Bound by Calcium Ions,* J. Phys. Chem. C, **2008,** 112, 14589.

- R. Koole, M. M. van Schooneveld, J. Hilhorst, C. de Mello Donega, D. C. 't Hart, A. van Blaaderen, D. Vanmaekelbergh, A. Meijerink; *On the incorporation mechanism of hydrophobic quantum dots in silica spheres by a reverse microemulsion method,* Chem. Mater., **2008,** 20, 2503.

- R. Koole, M. M. van Schooneveld, J. Hilhorst, K. Castermans, D. P. Cormode, G. J. Strijkers, C. d. M. Donega, D. Vanmaekelbergh, A. W. Griffioen, K. Nicolay, Z. A. Fayad, A. Meijerink, W. J. M. Mulder; *Paramagnetic Lipid-Coated Silica Nanoparticles with a Fluorescent Quantum Dot Core: A New Contrast Agent Platform for Multimodality Imaging,* Bioconjugate Chem., **2008,** 19, 2471.

- M. Klokkenburg, J. Hilhorst, B. H. Erne; *Surface analysis of magnetite nanoparticles in cyclohexane solutions of oleic acid and oleylamine,* Vib. Spectrosc., **2007,** 43, 243.

Introduction

The central topic of this thesis is the observation and manipulation of crystallographic defects in colloidal crystals. In materials science, crystallographic defects are generally seen as a nuisance: they are imperfections that significantly alter the properties of any desired crystalline material, usually in unpredictable ways. Examples of this are metal fatigue, radiation damage and degradation of semiconductors.[1] In the pursuit of perfection, we tend to forget that defects can also have beneficial effects. For example, "impurity" dopants are essential to the functioning of integrated circuits, solar cells and virtually every other semiconductor device,[2] while dislocations can strengthen metals through a process called "work hardening".[1]

Both the beneficial and deleterious properties of crystallographic defects and the fact that they occur in any crystalline material warrant the intensive research that has been spent on the subject for close to a century. Long before that, the properties of defects were already unknowingly exploited by blacksmiths as early as the copper and bronze ages, hardening their tools and weapons by cold working. Still, investigations into the fundamental nature of crystallographic defects only date back to early work by, amongst others, Frenkel (1926),[3] Peierls (1940)[4] and Lawrence Bragg (1949).[5]

The study of defects in metals, ceramics, salts and other atomic crystals is challenging because of the range of scales that are involved. The properties of defects are determined by their structure on the single atom scale, *i.e.* angstroms to nanometers. The effects of defects on material properties, like plastic strength or conductivity, are measured on a macroscopic scale of millimeters. On this scale, most materials possess many defects of different types, complicating direct measurements of the relation between material properties and single

defect structures. In addition, the time scales at which dynamic processes like crystal growth or dislocation creep occur are too short to image them on a single particle level. It is for this reason, that in this thesis, colloids are used to study crystallographic defects.

1.1 COLLOIDS

1.1.1 Colloids as Model System

Colloids are particularly suited to study crystal defects in real-space on a single particle level. Colloids are particles with sizes roughly between 1 and 1000 nm.[6] In the upper range of this scale, particles are large enough to be observed with light microscopes, while thermal motion is still important for their behavior. In many ways, colloids behave very similar to atoms or small molecules, only at a much slower time scale. This, combined with their large size, makes colloids ideal for studying processes that happen too fast or at a too small scale to be observed in atomic or molecular systems. In addition, their interaction potential can be made-to-order: short- and long-range repulsions as well as attractions can be added as required.[7, 8] Recently, the addition of directionality to the interactions has gained more and more attention.[9, 10] Because of their size and their tunability, colloids are often labeled "model atoms".

The simplest colloidal system is the hard sphere system. In this system, particles have an infinitely large repulsive potential for interparticle distances closer than their diameter. Beyond that, interactions are absent. This system has no atomic equivalent; the closest analog being the noble gases. Despite their simple interactions, hard spheres do exhibit a fluid-solid phase transition. Since Alder and Wainwright[11] and Wood and Jacobsen[12] predicted hard sphere crystallization in their simulations, experimentalists have striven to study this process in experiments. This has led to a wealth of studies on phase behavior,[13] crystal nucleation,[14, 15] crystal structure[16-19] and growth dynamics.[20-24]

Recently, the abundance of defects in colloidal crystals has prompted studies into the fundamentals of defect behavior, employing the size and slow dynamics of the particles to study defects in real-space and –time.[25-29] Investigating the properties of defects in colloidal crystals on a fundamental level, characterizing different types of defects and comparing their properties to those of defects in atomic crystals makes up a substantial part of this thesis.

1.1.2 Colloids for Photonic Crystals

In addition to their value as model systems, colloidal crystals have been found to be promising candidates for the production of cheap photonic crystals.[30] Photonic crystals are materials with periodic variations in refractive index in which

photons of a certain energy cannot propagate. These materials show promise for applications as low-loss optical fibers,[31, 32] low-threshold lasers[33] and even optical circuitry.[34]

Although colloidal photonic crystals can be grown quickly and cheaply, there are several hurdles to be taken to optimize their properties. Firstly, a method has to be found to reproducibly grow structures with a robust, full band gap. Secondly, control over the inclusion of defects has to be obtained to reduce unwanted disorder and add functionality where it is required.

For the first point, it is important to realize that none of the direct colloidal crystal structures that have been obtained up until this moment possesses a full photonic band gap. The structure that shows the most promise is the fcc structure, but for a band gap to open up in this structure, the crystal voids have to be infiltrated with a high refractive index material and the colloidal particles etched away.[35-38] The resulting inverted fcc structure has been calculated to have a full optical band gap, but this is extremely sensitive to disorder.[39] Several non close packed structures have been calculated to have full band gaps that are more resistant against deformations. These structures are much harder to grow with colloids, as they require a directionality in their interactions[9] or an external restriction such as a growth template.[40] Among the wide-gap structures are the diamond and pyrochlore lattices. Colloidal realizations of these structures have not been obtained in experiments and will therefore not be investigated in this thesis. Nonetheless, many types of defects in these structures have a large degree of similarity with the faults discussed here for fcc crystals and results obtained here will therefore also be applicable to these more complex structures.

The second hurdle, on the road to functional colloidal photonic crystals is gaining control over the inclusion of defects, as even wide-gap materials suffer from degradation of their optical properties by defects. With this goal, chapters 3, 4 and 5 focus on the characterization of defects in dried colloidal crystals. On the other hand, selective growth of faults into photonic structures can positively influence their properties, much like selective doping of semiconductors. Therefore, in chapters 7 and 8 the aim is to investigate the role of defects in the growth of sedimentary colloidal crystals and to influence their inclusion.

1.2 DEFECT TYPES

As defects are the main topic of this thesis, common types of defects and their characteristics will be discussed below.

Four classes of defects are generally distinguished, based on their dimensionality: 0D point defects, 1D line defects, 2D planar defects and 3D bulk defects. Each of these will be discussed below.
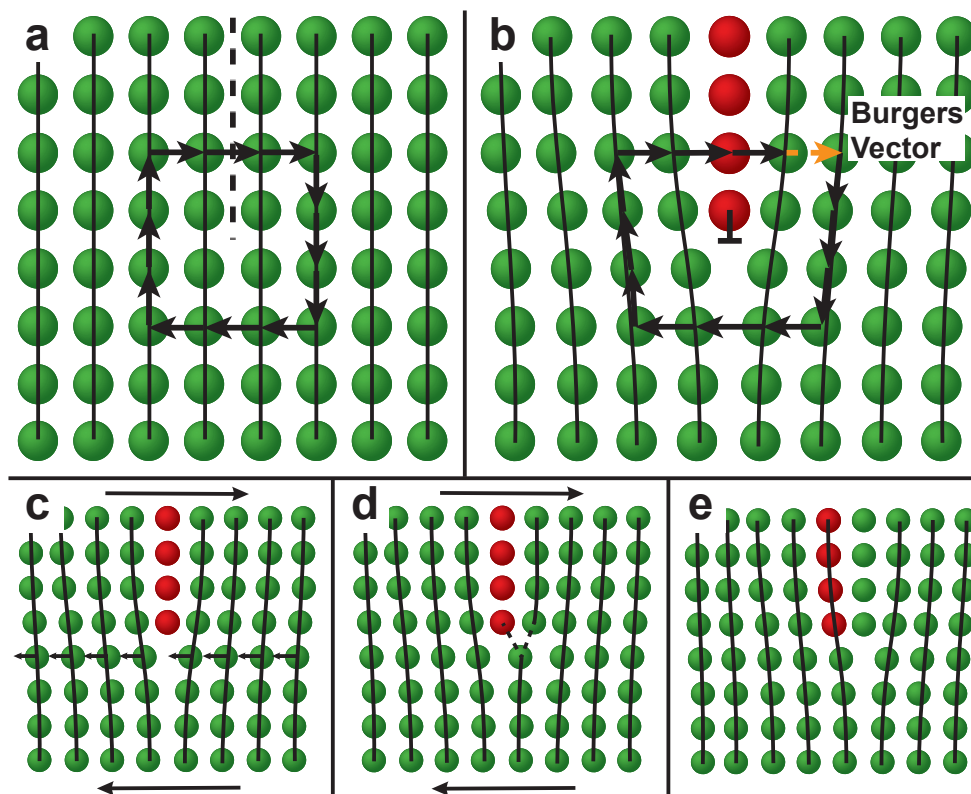
Figure 1.1. Panel (a) shows a perfect cross-section of a simple cubic lattice. If the crystal is cut halfway along the dashed line and a half plane is inserted, the structure in (b) results. This is an edge dislocation. The arrows in (a) and (b) show the Burgers circuit, with the lighter arrow in (b) the Burgers vector that is required to close the circuit. Panels (c)-(e) show the glide mechanism as explained in the main text.

1.2.1   Point Defects

Point defects can be divided into several types. The most well-known is the vacancy, where a single atom is removed from its lattice site to create a void. Its counterpart is the self-interstitial, where an extra atom of the same type as the host crystal is added to the lattice. This interstitial has to take up a position between lattice sites, thus distorting the surrounding structure. A closely spaced vacancy-interstitial pair in an ionic crystal is called a Frenkel defect. Point defects occur in all crystals due to thermal excitations, with vacancy concentrations in for example copper ranging from 10^{-5} at its melting temperature to 10^{-22} at room temperature.[1]

Further important point defects are impurities. These are atoms or ions of an element that is alien to the host lattice. Substitution impurities replace the original material at its lattice site, while interstitial impurities infiltrate the space between lattice sites. In semiconductor materials impurities may be added as dopants to

4

add extra electrons or holes to the material and create n- or p-type semiconductors respectively. In steel, carbon doping is used to increase hardness, although concentrations may be high enough that alloying would be a better description.

1.2.2   Line Defects

The most important line defects occurring in crystals are dislocations. Dislocations form an extensive class of defects with important implications for macroscopic crystal properties. The concept of dislocations was introduced as a solution to the problem that the theoretical shear strength of a lattice exceeded the experimental shear strength by orders of magnitude.[41-43] The values obtained by calculations made before the notion of dislocations originated from the assumption that under shear, whole crystallographic planes would have to slide with respect to each other.[44] This would require the simultaneous breaking of bonds for all particles in a layer and a simultaneous climbing of the activation barrier for all particles, resulting in a very high activation energy. In 1934 the concept of dislocations was introduced by Orowan, Polanyi and Taylor in three independent publications, [41-43] explaining the low plastic strength of real crystals compared to the values predicted by Frenkel.[44] To clarify the mechanism by which dislocations soften a material, figures 1.1a and 1.1b show a schematic cut through a simple cubic lattice in which the simplest possible dislocation is produced. This is created by incising the lattice along the dashed line (figure 1.1a) and inserting an extra half-plane (figure 1.1b), resulting in a defect line running into the paper at the position of the inverted T in figure 1.1b. The dislocation structure has a very low activation barrier against movement, as shown in figures 1.1c, 1.1d and 1.1e. Instead of moving a whole layer at once, bonds have to be broken along a single line of particles in order to move a dislocation through a lattice to a neighboring position, a process called glide.

For the characterization of dislocations, one of the most essential quantities is the Burgers vector, named after the Dutch physicist Jan Burgers.[45] The Burgers vector is a measure for the extent of the deformation of the lattice. It is obtained by considering a perfect crystal lattice, such as in figure 1.1a. Here, a closed circuit can be drawn by starting at a random particle and taking n steps of one lattice constant to the right, n down, n left and n up, as illustrated in figure 1.1a. If the same steps are drawn around a dislocation, as in figure 1.1b, a gap remains in the circuit. The vector that is required to close this gap is the Burgers vector. In this case, the Burgers vector is perpendicular to the dislocation line, which is characteristic of an edge dislocation. Note that the direction of the Burgers vector depends on the choice of Burgers circuit. In these images the circuit runs clockwise, but the direction is not important for the description of dislocations, as long as it is applied consistently.

The relation between the structure of the dislocation core, *i.e.* the region of

strongest deformations around the inserted plane, and crystal strength was first obtained by Rudolph Peierls in 1940.[4] In his paper, he derived the deformation profile, *U(x)*, of a dislocation in a simple cubic lattice, assuming a periodic sinusoidal interplanar potential. This deformation is given by

$$U(x) = \frac{b}{\pi}\arctan\frac{x}{w} - \frac{b}{2} \qquad (1.1)$$

where *b* is the dislocation Burgers vector and 2*w* is the size of the region in which half of the deformation is contained, also called dislocation width. Peierls determined that the parameter *w* is of paramount importance for the crystal shear strength according to

$$\sigma_p = \frac{2\mu}{1-\nu}e^{-4\pi w/b} \qquad (1.2)$$

Here, σ_p is the stress required to move a dislocation through the lattice, now called the Peierls stress. μ is the bulk shear modulus of the material and *v* the Poisson ratio. Although this expression has undergone several slight modifications over time,[46, 47] the implications have largely remained the same: crystal hardness strongly depends on dislocation width.

Dislocation Types

Apart from edge dislocations, several types of dislocations are of importance to the crystals discussed in this thesis. The first is the screw dislocation. Together with edge dislocations, these form the simplest dislocations one can find in any lattice. The difference between edge and screw dislocations is the direction of the Burgers vector with respect to the dislocation line. In figure 1.1b, if one imagines the crystal to consist of similar layers stacked on top of each other, the dislocation runs into the plane, while the Burgers vector points to the right, *i.e.* perpendicular to the dislocation line. This is characteristic for an edge dislocation. Together, the dislocation line and Burgers vector define a plane. This is the only plane in which the dislocation can glide, as shown for example in figures 1.1c-e. For a screw dislocation, Burgers vector and dislocation line run parallel and any plane containing both vectors can in principle act as a glide plane.

In close-packed crystals such as many metals or colloidal crystals, full edge and screw dislocations hardly occur. The reason for this is the availability of multiple (meta-)stable positions for particles on a hexagonal crystal plane. Any basic dislocation on such planes will split up in partial dislocations, *i.e.* dislocations with Burgers vectors smaller than a lattice constant. This is shown in figures 1.2a and 1.2b. Figure 1.2a shows a full edge dislocation contained between two hexagonal planes. The dislocation line runs vertically, while the Burgers vector points to the right. Figure 1.2b shows the splitting of this edge dislocation into two partial dislocations. If face centered cubic (fcc) lattice indices are used, it can be seen that
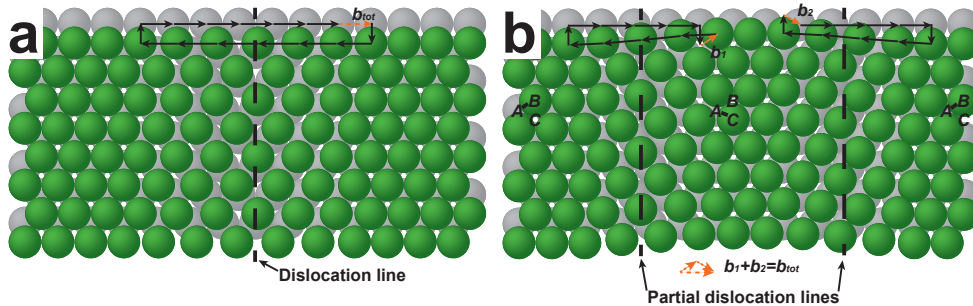
Figure 1.2. In a hexagonal lattice, an edge dislocation along <110> looks as presented in (a). The configuration in (a) is not stable and will dissociate to form two partial dislocations separated by a stacking fault, as shown in (b).

a full dislocation with Burgers vector $\frac{1}{2}[110]$ splits into two partials with Burgers vector $\frac{1}{6}[211]$ and $\frac{1}{6}[12\bar{1}]$. As dislocations can only be created or terminated at the edge of a crystal, dislocation reactions within a crystal must preserve the total Burgers vector; by summing the partial Burgers vectors, the original Burgers vector is obtained. The total magnitude of the partial Burgers vectors is therefore equal to or larger than the full Burgers vector. Dislocation line energy, however, is proportional to the square of the magnitude of the Burgers vector. Therefore, the partial dislocations mentioned here have a 33% lower line energy than the full dislocation. A stacking fault (discussed in the next section) that is created between the partials leads to an additional energy term counteracting the splitting process. The degree of dislocation splitting therefore depends on the magnitude of this stacking fault energy.

Dislocations with Burgers vectors $\frac{1}{6}\langle 112 \rangle$, as discussed above, are called Shockley partial dislocations. These constitute one of the most abundant types of dislocations in close packed crystals. They can exist both in screw and edge configuration, but the configurations displayed in figure 1.2b contain a bit of both. These are called mixed dislocations. Shockley partials are the most mobile dislocations in close packed crystals, due to the fact that their glide planes are always $\{111\}$ planes. These are the planes with the lowest glide barriers and are in practice the only planes to accommodate glide in close packed crystals. The properties of Shockley partials in colloidal crystals will be studied in detail in chapter 6 of this thesis.

Another important type of partial dislocation is the Frank partial. These partials have a burgers vector of $\frac{1}{3}\langle 111 \rangle$ with dislocation lines usually lying along the $\langle 110 \rangle$ directions perpendicular to this. They are therefore of edge type, with $\{112\}$ glide planes. As the activation energy for glide is very high in these planes, these dislocations will not glide easily. Such dislocations are called sessile. They can still move, but only in a process assisted by the emission or absorption of vacancies,
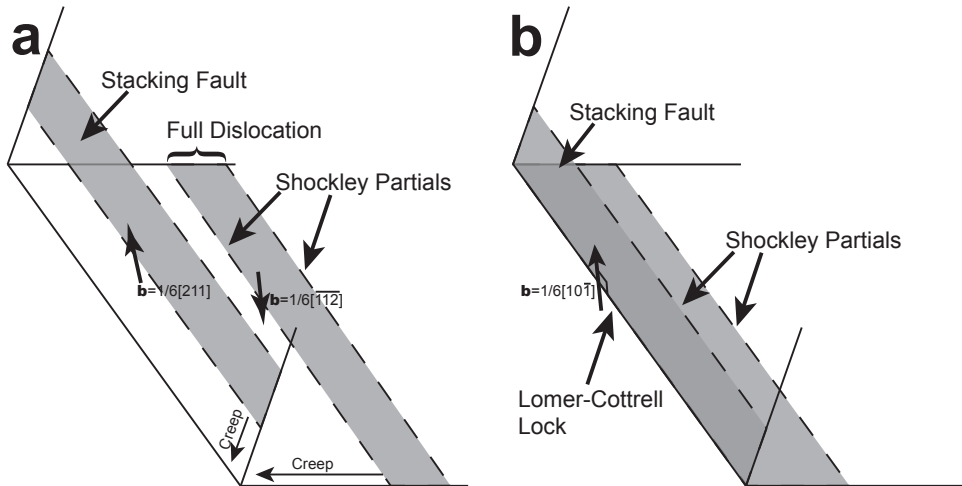
Figure 1.3. The formation of a Lomer Cottrell lock is displayed. In (a) two dissociated dislocations on two different {111} planes diffuse towards each other. This leads to a reaction between the partial dislocations of which the Burgers vector is shown (Burgers vectors are in-plane here). In (b), the partials have reacted to form the lock. The Burgers vector is perpendicular to the dislocation line. The dislocation is still accompanied by the original stacking faults and remaining Shockley partials.

called climb. Dislocations of this type hardly occur in colloidal crystals, but are important for the formation of stacking fault tetrahedra, as will be discussed in chapter 8.

A final type of partial dislocation that is important in both metals and colloidal crystals is the Lomer-Cottrell lock or stair-rod sessile dislocation. These dislocations occur when two Shockley partials with parallel dislocation lines on different $\{111\}$ planes glide to the same position and associate to form a dislocation with Burgers vector $\frac{1}{6}\langle 110 \rangle$ (see the schematic in figure 1.3). This results in a six fold decrease in line energy (b^2 is equal to 2x1/6 before the reaction and 1/18 after it) and is therefore strongly favored. Lomer-Cottrell locks are sessile edge dislocations and are important in work hardening: Deformation of metals results in the creation of more and more dislocations that can glide through the crystal until the formation of Lomer-Cottrell locks blocks further movement and deformation becomes harder. [1] As Shockley partials in atomic crystals are always accompanied by intrinsic stacking faults, Lomer-Cottrell locks border two stacking faults on different $\{111\}$ planes. Hence the name stair-rod dislocation, as they resemble the rods used to lock a stair carpet in place. The role of Lomer-Cottrell locks in colloidal crystals will be discussed in chapters 3 and 7, while their properties will be employed to selectively incorporate stacking faults in colloidal crystals in chapter 8.
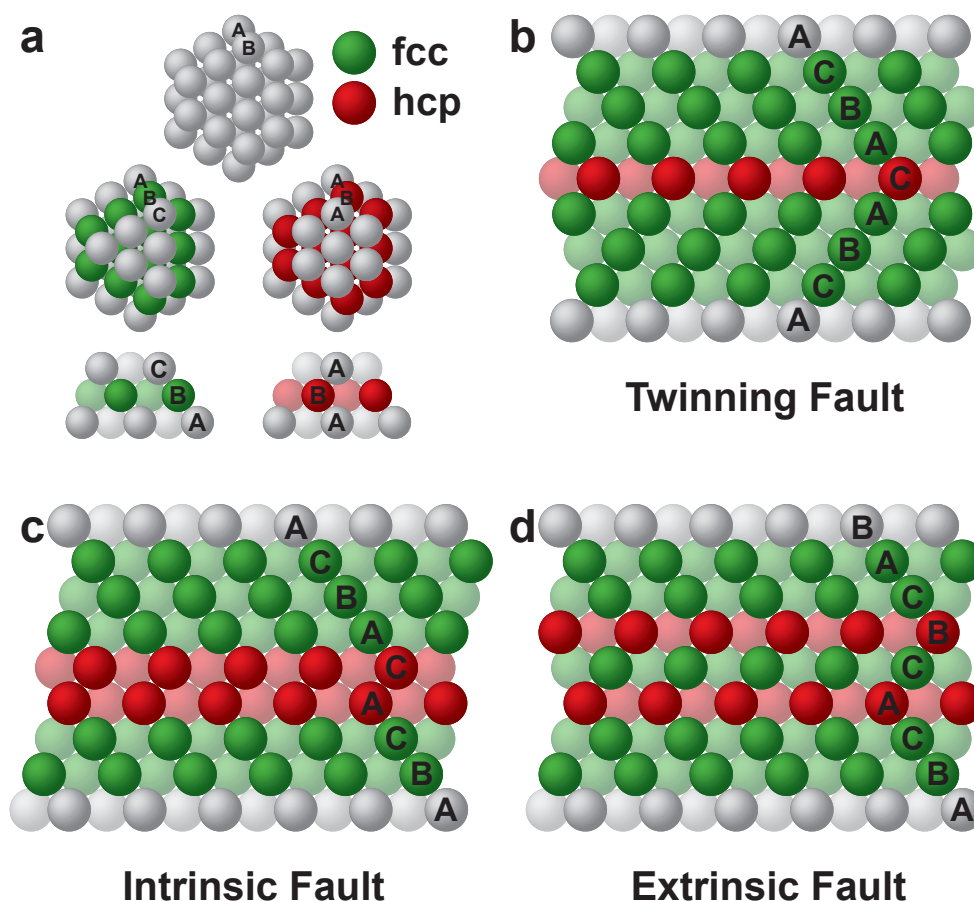
8

Figure 1.4. Panel (a) displays the formation of fcc and hcp structure by stacking hexagonal layers in ABC or ABA fashion, respectively. (b)-(d) Several types of stacking disorder as described in the main text.

1.2.3 Planar Defects

The most studied defects in colloidal crystals are planar defects called stacking faults. Stacking faults can occur when two crystalline layers can assume more than one (meta-)stable position with respect to each other. This is illustrated for hexagonal crystals in figure 1.4a. If the first hexagonal layer of a hexagonal lattice is placed in an A position, the next layer can be positioned at either a B or a C position. For a two layer system, these two positions are equivalent. If the second layer is stacked in a B position, the next layer can assume either a C or an A position, resulting in an ABC (fcc) or an ABA (hexagonal close packed, hcp) stacking, respectively. Depending on the interaction potential between crystal building blocks, crystals can either have a full hcp structure of continued ABABAB stacking or an fcc

ABCABC structure. Stacking faults occur when a layer is positioned such that it breaks the stacking sequence, resulting in the inclusion of an hcp layer in the fcc structure and vice versa.

Several types of stacking faults can be distinguished. These will be discussed for the fcc structure, as this is the dominating crystal structure in this thesis. The first type is the twinning fault (figure 1.4b). This consists of a single hcp layer in an fcc crystal that changes the stacking from ABC to CBA. The second type is called an intrinsic stacking fault and is created by removing an arbitrary layer from the stacking sequence, as in figure 1.4c. This results in two hcp layers bordering each other, while the direction of the fcc stacking is preserved over the rest of the crystal. The same deformation can be achieved by shifting half of the crystal from a B to a C position. A final type of stacking fault is the extrinsic stacking fault (figure 1.4d). This is created by inserting a layer at an arbitrary position and creates two hcp layers separated by a single fcc layer. Stacking faults and their effects on crystal growth will be discussed in chapters 3, 7 and 8.

Another type of 2D defect is the grain boundary. This is the surface between differently oriented crystallites and in that sense is an extracrystalline defect. This is the only place, apart from the crystal edge, where dislocations, vacancies and interstitials can be annihilated without reacting with their counterpart.

1.2.4   Bulk Defects

Bulk defects form the remainder of crystallographic defects. These can be large impurities, vacancy agglomerates, or interstitial precipitates. Such defects can serve to annihilate vacancies or interstitials, as they form a kind of internal grain boundary. Dislocations, however, are generally much longer than the extent of a bulk defect and cannot be annihilated there. Instead, they can undergo reactions with it. Usually, this results in dislocation pinning; locally increasing the resistance against dislocation movement, making a moving dislocation bend around the impurity and curving the dislocation between bulk defects. Bulk defects will not be discussed further in this thesis.

1.3   CHARACTERIZATION

As mentioned earlier, colloid are slow and large and can therefore serve as model systems that are relatively easy to study. In some cases, these model systems can indeed be observed at the single particle level and in real time, leading to the understanding of fundamental processes at the smallest scale. A valuable tool here is confocal microscopy, a technique that will be explained below. Sometimes, colloidal systems are unsuited for such measurements due to their small size or strong scattering. In order to characterize such systems, X-ray techniques have
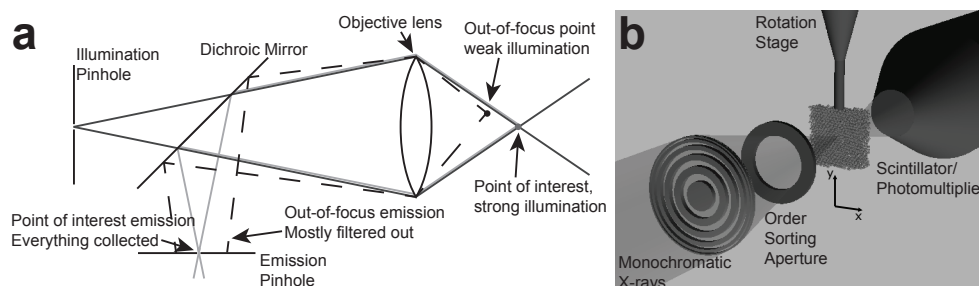
Figure 1.5. (a) The essence of a confocal microscope: the use of two pinholes through which the light from only a single focal point in the sample is illuminated and detected. (b) A schematic of the essential components of a STXM.

been the method of choice for much of the work presented here. Below, the X-ray diffraction and X-ray microscopy setups that have been used are presented.

1.3.1 Confocal Microscopy

Confocal scanning laser microscopy (CSLM) has been a very valuable tool for the understanding of fundamental crystallization processes. Since the demonstration of this technique for colloids [48-51] it has been used to investigate the structure of critical nuclei,[14] nucleation around impurities,[15] equilibrium crystal structures [16-19] and the nucleation of misfit dislocations.[26] The strengths of this technique, compared to conventional microscopy, are its improved resolution and, more importantly, its superior contrast. By illuminating a single spot in a sample through a pinhole and objective lens and imaging this same focal point again through another pinhole, almost all of the light that was not emitted in the point of interest is filtered out, as shown schematically in figure 1.5a. This way of imaging strongly improves the contrast in the out-of-plane imaging direction, enabling three dimensional imaging of a sample.

As only a single spot of the sample is illuminated at one time, the sample has to be raster scanned to obtain an image. By scanning in the in-plane and out-of-plane directions, a full 3D scan of a sample can be made. Such volume scans of a colloidal crystal can reveal the complete crystal structure, including all defects.

CSLM is a fluorescence technique and therefore requires the use of dyed particles. Since the aim is to investigate materials in three dimensions, the fluorescence signal has to be obtained from within a sample. Hence, strongly attenuating samples are unsuited for confocal imaging. For this reason, the refractive index of the solvent used to disperse colloids is matched to the refractive index of the colloidal material. This has the added benefit that Van der Waals interactions are minimized and hard sphere behavior is mimicked more closely.

1.3.2 X-Ray Microscopy

For studying dried crystals, using CSLM is not always an option. This is mainly due to the large refractive index contrast between the particles and the air that has replaced the solvent. In chapters 4 and 5 the possibility of using scanning transmission X-ray microscopy (STXM) as characterization method for such systems is investigated.

Figure 1.5b shows a schematic of the STXM setup as used in chapters 4 and 5. One of the major advantages of STXM over other X-ray microscopy techniques is the possibility to accurately tune the X-ray energy to an absorption edge of a particular element present in the sample. By measuring X-ray transmission through a sample at energies just below and just above the absorption edge and subtracting the resulting optical density images from each other, phase contrast can be eliminated and element-specific absorption images are obtained. This greatly facilitates the interpretation of images.

For this energy tunability, synchrotron radiation is a requirement. The desired photon energies are selected by a diffraction grating before the STXM setup, resulting in a monochromatic beam. The whole STXM setup is shown in figure 1.5b. The monochromatic beam is shown on the left of this image. The X-rays are subsequently focused by a Fresnel zone plate. This is a piece of optics that focuses through diffraction rather than refraction. As this type of focusing produces more than one focal point, an order sorting aperture is added to the setup to filter out all light that is focused into secondary focal points, as well as unfocused light. The focused beam illuminates the sample in a single spot, with a resolution determined by the width Δr_n of the outer ring of the zone plate: $R \approx 1.2 \Delta r_n$. The transmitted intensity is detected by a detector consisting of a scintillator and a photomultiplier tube. By scanning the sample in the x-y plane, perpendicularly to the beam, images of a sample can be obtained. In chapter 5, a rotation stage is employed to rotate the sample and obtain a tomogram, creating a 3D image of the full crystal.

1.3.3 X-Ray Diffraction

One drawback of microscopy techniques is limited field of view, resulting in a lack of statistics. While it is extremely valuable to have information on the smallest scale, it is hard to draw solid conclusions about a sample based on a few microscopy images. Different regions of the sample may have completely different characteristics that have been ignored by chance. Moreover, microscope images are prone to prejudice: we tend to focus on information we expect or hope to see. X-ray diffraction is a technique that provides averaged information on large areas of a sample. Despite the loss of local information in X-ray diffractograms, the offered statistics are invaluable for the characterization of colloidal crystals.

The difficulty of X-ray diffraction on colloids is the large difference in scale

between X-ray wavelength (~1Å) and particle size (~1µm). Because of this, scattering angles are extremely small. More convenient wavelengths, in the optical or UV regime, have too strong interactions with the sample to be of use. Even the much weaker interacting X-rays suffer from effects of multiple diffraction in high quality crystals, as is shown in chapter 2. Nonetheless, X-ray diffraction can shed light on the average structure of a sample, resulting in valuable information, as shown in chapter 3.

1.4   OUTLINE OF THIS THESIS

This thesis focuses on the identification, characterization and manipulation of various defects in colloidal crystals. Confocal microscopy and X-ray methods will be employed for the identification and characterization of defects, while lithography will be employed to create templates for the manipulation of defects. In chapters 2 to 5, focus will lie on X-ray techniques for the characterization of colloidal crystals. Chapters 2 and 3 go into the use of X-ray diffraction methods for characterizing stacking faults. Chapter 2 focuses mostly on measurement artifacts that have to be accounted for when analyzing diffraction data. Chapter 3 focuses on the presence of stacking faults in dried crystals, determining the average concentration of faults in such crystals and discussing the implications of their presence. In chapters 4 and 5 STXM is applied for the first time on dried colloidal crystals in an attempt to access their internal structure. In chapter 4 the details of the technique and its possibilities for characterizing colloidal materials are discussed. In chapter 5 a tomogram of a crystal is recorded and its internal structure is discussed.

In chapter 6 a different approach is taken. This chapter takes defect characterization to a more fundamental level. The properties of Shockley partial dislocations are investigated as a function of temperature on a single particle level in crystals of thermosensitive particles.

Finally, in chapters 7 and 8, the influence of Shockley partials and Lomer-Cottrell locks on the growth of sedimentary colloidal crystals is discussed (chapter 7) and the proposed mechanisms of influence are employed to selectively incorporate defects in crystals (chapter 8).

1.5   REFERENCES

[1] D. Hull, D. J. Bacon, Introduction to Dislocations, fourth edn., Elsevier Ltd., Oxford**, 2001**.
[2] R. S. Muller, T. I. Kamins, Device Electronics for Integrated Circuits, 3rd edn., Wiley**, 2002**.
[3] J. Frenkel, *Z. Phys.,* **1926**, 35, 652.

[4] R. Peierls, *Proc. Phys. Soc.*, **1940**, 52, 34.

[5] L. Bragg, W. M. Lomer, *Proc. R. Soc. London, Ser. A*, **1949**, 196, 171.

[6] International Union for Pure and Applied Chemistry; *http://goldbook.iupac.org/C01172.html*, **2011**.

[7] A. Yethiraj, A. van Blaaderen, *Nature,* **2003**, 421, 513.

[8] R. Tuinier, J. Rieger, C. G. de Kruif, *Adv. Colloid Interf. Sci.,* **2003**, 103, 1.

[9] S. C. Glotzer, M. J. Solomon, *Nature Mater.,* **2007**, 6, 557.

[10] D. J. Kraft, J. Groenewold, W. K. Kegel, *Soft Matter,* **2009**, 5, 3823.

[11] B. J. Alder, T. E. Wainwright, *J. Chem. Phys.,* **1957**, 27, 1208.

[12] W. W. Wood, J. D. Jacobson, *J. Chem. Phys.,* **1957**, 27, 1207.

[13] P. N. Pusey, W. Vanmegen, *Nature,* **1986**, 320, 340.

[14] U. Gasser, E. R. Weeks, A. Schofield, P. N. Pusey, D. A. Weitz, *Science,* **2001**, 292, 258.

[15] V. W. A. de Villeneuve, R. P. A. Dullens, D. G. A. L. Aarts, E. Groeneveld, J. H. Scherff, W. K. Kegel, H. N. W. Lekkerkerker, *Science,* **2005**, 309, 1231.

[16] P. N. Pusey, W. Van Megen, P. Bartlett, B. J. Ackerson, J. G. Rarity, S. M. Underwood, *Phys. Rev. Lett.,* **1989**, 63, 2653.

[17] W. K. Kegel, J. K. G. Dhont, *J. Chem. Phys.,* **2000**, 112, 3431.

[18] V. C. Martelozzo, A. B. Schofield, W. C. K. Poon, P. N. Pusey, *Phys. Rev. E,* **2002**, 66.

[19] J. Zhu, M. Li, R. Rogers, W. Meyer, R. H. Ottewill, STS-73 Space Shuttle Crew, W. B. Russel, P. M. Chaikin, *Nature,* **1997**, 387, 883.

[20] Z. D. Cheng, P. M. Chaikin, J. X. Zhu, W. B. Russel, W. V. Meyer, *Phys. Rev. Lett.,* **2002**, 88, 015501.

[21] S. Martin, G. Bryant, W. van Megen, *Phys. Rev. E,* **2003**, 67, 061405.

[22] K. Schatzel, B. J. Ackerson, *Phys. Rev. E,* **1993**, 48, 3766.

[23] K. Schatzel, B. J. Ackerson, *Phys. Rev. Lett.,* **1992**, 68, 337.

[24] Y. M. He, B. J. Ackerson, W. vanMegen, S. M. Underwood, K. Schatzel, *Phys. Rev. E,* **1996**, 54, 5286.

[25] J. M. Meijer, V. W. A. De Villeneuve, A. V. Petukhov, *Langmuir,* **2007**, 23, 3554.

[26] P. Schall, I. Cohen, D. A. Weitz, F. Spaepen, *Science,* **2004**, 305, 1944.

[27] A. Pertsinidis, X. S. Ling, *Nature,* **2001**, 413, 147.

[28] A. Pertsinidis, X. S. Ling, *Phys. Rev. Lett.,* **2001**, 87, 098303.

[29] W. Lechner, C. Dellago, *Soft Matter,* **2009**, 5, 2752.

[30] P. Jiang, J. F. Bertone, K. S. Hwang, V. L. Colvin, *Chem. Mater.,* **1999**, 11, 2132.

[31] P. Russell, *Science,* **2003**, 299, 358.

[32] J. C. Knight, *Nature,* **2003**, 424, 847.

[33] O. Painter, R. K. Lee, A. Scherer, A. Yariv, J. D. O'Brien, P. D. Dapkus, I. Kim, *Science,* **1999**, 284, 1819.

[34] M. Soljacic, C. Luo, J. D. Joannopoulos, S. Fan, *Opt. Lett.,* **2003**, 28, 637.

[35] O. D. Velev, T. A. Jede, R. F. Lobo, A. M. Lenhoff, *Nature,* **1997**, 389, 447.

[36] J. E. G. J. Wijnhoven, W. L. Vos, *Science,* **1998**, 281, 802.

[37] A. Blanco, E. Chomski, S. Grabtchak, M. Ibisate, S. John, S. W. Leonard, C. Lopez, F. Meseguer, H. Miguez, J. P. Mondia, G. A. Ozin, O. Toader, H. M. Van Driel, *Nature,* **2000**, 405, 437.

[38] Y. A. Vlasov, X. Z. Bo, J. C. Sturm, D. J. Norris, *Nature,* **2001**, 414, 289.

[39] J. D. Joannopoulos, S. G. Johnson, J. N. Winn, R. D. Meade, Photonic Crystals: Molding the Flow of Light, Princeton University Press, Princeton**, 2008**.

[40] A. Hynninen, J. H. J. Thijssen, E. C. M. Vermolen, M. Dijkstra, A. Van Blaaderen, *Nature Mater.,* **2007**, 6, 202.

[41] G. I. Taylor, *Proc. R. Soc. London, Ser. A,* **1934**, 145, 362.

[42] M. Polanyi, *Z. Phys.,* **1934**, 89, 660.

[43] E. Orowan, *Z. Phys.,* **1934**, 89, 634.

[44] J. Frenkel, *Z. Phys.,* **1926**, 37, 572.

[45] J. M. Burgers, *Proc. K. Akad. Wet. Amst.,* **1939**, 42, 293.

[46] F. R. N. Nabarro, *Mater. Sci. Eng. A-Struct,* **1997**, 234, 67.

[47] F. R. N. Nabarro, *Philos. Mag. A,* **1997**, 75, 703.

[48] A. Van Blaaderen, P. Wiltzius, *Science,* **1995**, 270, 1177.

[49] A. Van Blaaderen, A. Imhof, W. Hage, A. Vrij, *Langmuir,* **1992**, 8, 1514.

[50] A. Van Blaaderen, *Adv. Mater.,* **1993**, 5, 52.

[51] H. Yoshida, K. Ito, N. Ise, *Phys. Rev. B,* **1991**, 44, 435.

Diffuse X-ray Scattering in Random-Stacking Hexagonal Close-Packed Crystals of Colloidal Spheres

Microradian X-ray diffraction from sedimentary colloidal crystals is studied using synchrotron radiation with photon energies of 12.4, 27, and 38 keV. Stacking disorder in these hard-sphere crystals leads to diffuse X-ray scattering along Bragg scattering rods normal to the randomly stacked layers. Diffuse scattering, shown to be induced by multiple scattering, is observed along secondary Bragg rods in between the stacking-independent true Bragg reflections. This effect can be reduced by measuring at higher X-ray energies.

17

2.1   INTRODUCTION

Diffraction studies on periodic materials are generally interpreted based on their Bragg peaks; these provide important information about the general crystal structure and the average positioning of crystal building blocks with respect to each other. When using diffraction for studies on material defects, however, Bragg peaks do not reveal any information. Still, information about defects can be obtained by investigated the distribution of diffuse scattering in diffractograms.

Even for perfect crystals, where only sharp Bragg scattering is expected, the ever present thermal vibrations of the atoms lead to thermal diffuse scattering. The thermal motion of the atoms around their average position on an ideal lattice causes the well-known Debye–Waller effect, which reduces the intensity of the Bragg peaks and increases the background between them.[1-3] The distribution of this diffuse scattering intensity can be used to study the phonon dispersion in atomic crystals[4-7] or liquid-like molecular dynamics in protein crystals.[8] Moreover, in the case that a crystal possesses structural defects, a most crystals do, diffuse scattering can be employed to gain understanding of the nature of the defects.[1, 9]

The recovery of the defect structure from the diffuse intensity is still much less developed than the determination of average crystal structure from the Bragg intensities. Thanks to the advent of bright synchrotron radiation sources and fast area detectors, diffuse scattering experiments are now possible for a diverse set of materials including large scale structures, such as colloidal and photonic crystals. [10, 11]

Such experiments are particularly suitable for characterizing stacking disorder, as the theory behind this is well established. Stacking disorder is one of the most abundant and therefore most studied types of disorder in colloidal crystals. Although the stable crystal structure for hard spheres has been determined to be the face centered cubic (fcc) structure, the energy difference between the hexagonal close packed (hcp) and fcc structures is so small (of the order of 10^{-3} $k_B T$),[12, 13] that fast crystallization usually results in randomly stacked crystals with 50% fcc layers and 50% hcp layers.[14, 15] Over time, this gradually rearranges to the stable fcc structure, but large concentrations of stacking faults usually remain.[16-18] The structure and evolution of the stacking of colloidal crystals has been studied in reciprocal space using light scattering, small angle X-ray and neutron scattering.[10, 11, 19, 20] In the scattering domain the stacking disorder smears out some of the Bragg reflections along so-called Bragg scattering rods in the direction perpendicular to the planar stacking faults. However, reflections common to both fcc and hcp crystals are stacking-independent and remain true sharp Bragg spots. The 3D structure in reciprocal space of an rhcp crystal is illustrated schematically in figure 2.1a. Using the three basis vectors introduced in the figure, the diffraction vector **q**

can be written as

$$\mathbf{q} = h\mathbf{b}_1 + k\mathbf{b}_2 + l\mathbf{b}_3 \tag{2.1}$$

The true Bragg spots are positioned at integer values of $(h\text{-}k)/3$ and l. The rods are found at all the other linear combinations of h and k and are continuous in the $\mathbf{b}_3$ direction, that is, l can have any real value. By using Wilson's theory for the intensity distribution along a Bragg rod, information about the fraction of fcc material in the crystal (usually described by the parameter α) can be obtained[9, 18, 21, 22] and one can even discriminate between different crystallites in samples with coexisting rhcp and fcc crystals.[18] Additionally, the presence of a significant concentration of partial dislocations in the samples, creating islands of different stacking within each hexagonal close-packed plane, can be deduced from the difference in width between the Bragg rods and spots.[23, 24] In this chapter, the effects of multiple scattering on the distribution of diffuse scattering intensity in colloidal crystals are studied. It is shown that these can lead to spurious effects such as the appearance of strong secondary Bragg rods at values of $\mathbf{q}$ at which no scattered intensity should be present in the absence of multiple scattering. The strength of multiple scattering is reduced for higher energy X-ray photons, which interact more weakly with the sample. The effects of multiple scattering should be taken into account for proper interpretation of experimental data.[25, 26]

2.2   EXPERIMENTAL

The samples consist of sterically stabilized silica spheres with a diameter of 224 nm[27] and polymer depletant with a radius of gyration of 14 nm. These samples form large single crystals and have been employed in earlier studies.[11, 18] Although large single crystals are present in the samples, their diffraction patterns contain reflections of many different crystals. This is due to the large beam size at the sample (about 0.5 mm diameter).

The X-ray diffraction experiments were performed at the European synchrotron radiation facility (ESRF) in Grenoble at two beamlines: the Dutch–Belgian beamline BM-26[28] and the high-energy materials science beamline ID-11.[29] For the experiments a microradian X-ray diffraction setup was used.[30-32] This setup differed in some details between these two beamlines. In general a monochromatic X-ray beam was focused on a CCD detector (Photonic Science, 4008x2671 pixels of 9x9 mm²) by a set of compound refractive lenses (CRLs).[33] At beamline BM-26, an individual set of seven beryllium lenses was selected to focus the beam at 12.4 keV on the detector at approximately 8 m distance. The samples were placed just after the CRLs. The beam diameter on the sample was about 0.5 mm. At beamline ID-11 an X-ray transfocator based on aluminum CRLs[34] is installed. The device consists of a set of lenses whose focal distance can be continuously adjusted by
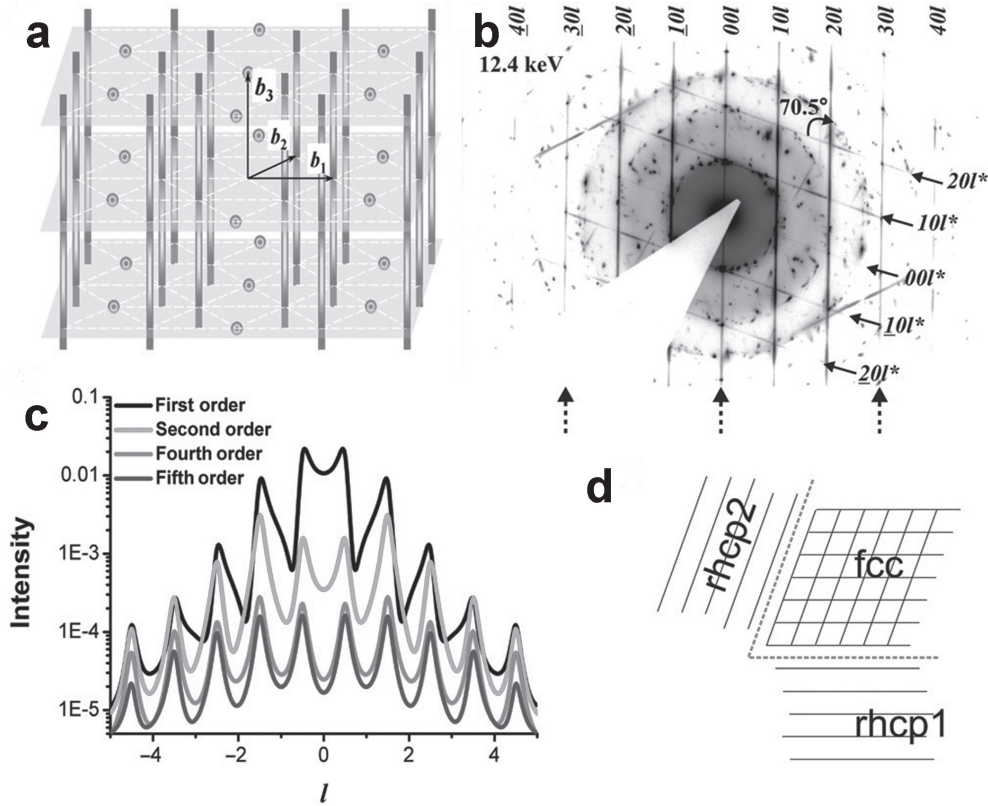
Figure 2.1. (a) Reciprocal lattice of rhcp consisting of Bragg rods and Bragg spots. The grey planes are meant to guide the eye. (b) Diffraction pattern measured at photon energy of 12.4 keV. The labels are explained in the text. (c) Calculated diffraction intensity $I(q) \propto S(q) * F(q)$ along 10l, 20l, 40l, 50l rods. (d) Schematic representation of the possible configuration of two rhcp crystals connected by an fcc crystallite. The thin lines schematically represent close-packed hexagonal layers of colloidal spheres. Both rhcp crystals cause the Bragg rods at an angle of 70.5 with respect to each other.

the mechanical movement of one or more groups of individual lenses. This option allowed us to switch easily from 27 to 38 keV energies at fixed setup geometry. The samples were placed at ~1.5 m after the transfocator and at a distance of about 5m from the detector. The beam diameter on the sample was about 0.5 mm.

2.3   RESULTS & DISCUSSION

In figure 2.1b, a diffractogram taken at a photon energy of 12.4 keV is displayed. The sample was positioned in an orientation such that several different sets of diffuse Bragg rods are clearly visible in the image. Their presence can be explained by stacking disorder in the colloidal crystals. The vertical rods in figure 2.1b are produced by making a cut through the plane defined by the vectors $\mathbf{b}_1$ and $\mathbf{b}_3$ in

20

figure 2.1a, that is, by measuring along the axis perpendicular to this plane. The intensity modulation along the diffuse scattering Bragg rods can be described by Wilson's theory.[9, 21] The calculated intensity profiles for the 10l, 20l, 40l and 50l rods are shown in figure 2.1c. The indices correspond to the h, k and l in equation 2.1. Here it was assumed that the crystal is formed by uniform spheres with size polydispersity of 5%. The fraction of fcc planes in the crystal was assumed to be 0.5. One can see in both theoretical (figure 2.1c) and experimental (figure 2.1b) results that the structure factor leads to modulations of the intensity along the rod with maxima at around half-integer l values. Form factor effects also contribute to the signal. These reduce the overall intensity for higher-order rods and for larger l values. The oscillations of the form factor can distort the intensity modulation and shift the position of the maxima.

In addition to the set of vertical Bragg rods, one can see contributions from other crystallites within the beam. Some of these form groups that spread over circles with a well-defined **q**-value. These signals can mostly be assigned to true Bragg spots, which have a fixed distance from the origin of reciprocal space (i.e., position of the direct beam closed by the beamstop). There are also spots and streaks that are not positioned on specific **q**-rings. These reflections with continuously varying **q** values are the Bragg rods of other crystallites, which intersect the Ewald sphere. It is interesting that in this pattern one can also see the presence of a (much weaker) set of diffuse scattering rods (denoted with 00l*, 10l*, etc in figure 2.1b), that are at an angle of 70.5° relative to the sequence of the vertical Bragg rods. This very specific relation between the reflections can be explained by the symmetry of the fcc crystal. While in an rhcp crystal there is a unique axis along which close-packed planes are stacked, fcc crystals contain four equivalent <111> axes, each of which is prone to stacking disorder. When a small fcc crystal is present from which rhcp crystals grow in different <111> directions, and this crystal is measured along a specific direction that is perpendicular to two of these <111> axes (as depicted schematically in figure 2.1d), the disorder along both axes will be visible in the diffractogram in the form of two sets of Bragg rods. As two different hexagonal close-packed planes always make an angle of 70.5° with each other, the same angle is observed between the rods.

As explained above, the stacking-disorder-induced Bragg rods should not occur if the diffraction vector corresponds to integer values of (h-k)/3. However, in figure 2.1b, one can also see diffuse scattering along 00l, 30l, etc. ''rods'', indicated by the dashed arrows. The presence of these rods cannot be explained by stacking disorder. Previously, their presence has been discussed (in colloidal crystals of different types) in the context of deformations around Lomer–Cottrell partial dislocations[22] or strong multiple diffraction.[11] To investigate the effect of multiple scattering on these secondary Bragg rods, experiments at photon energies of 27 and 38 keV were
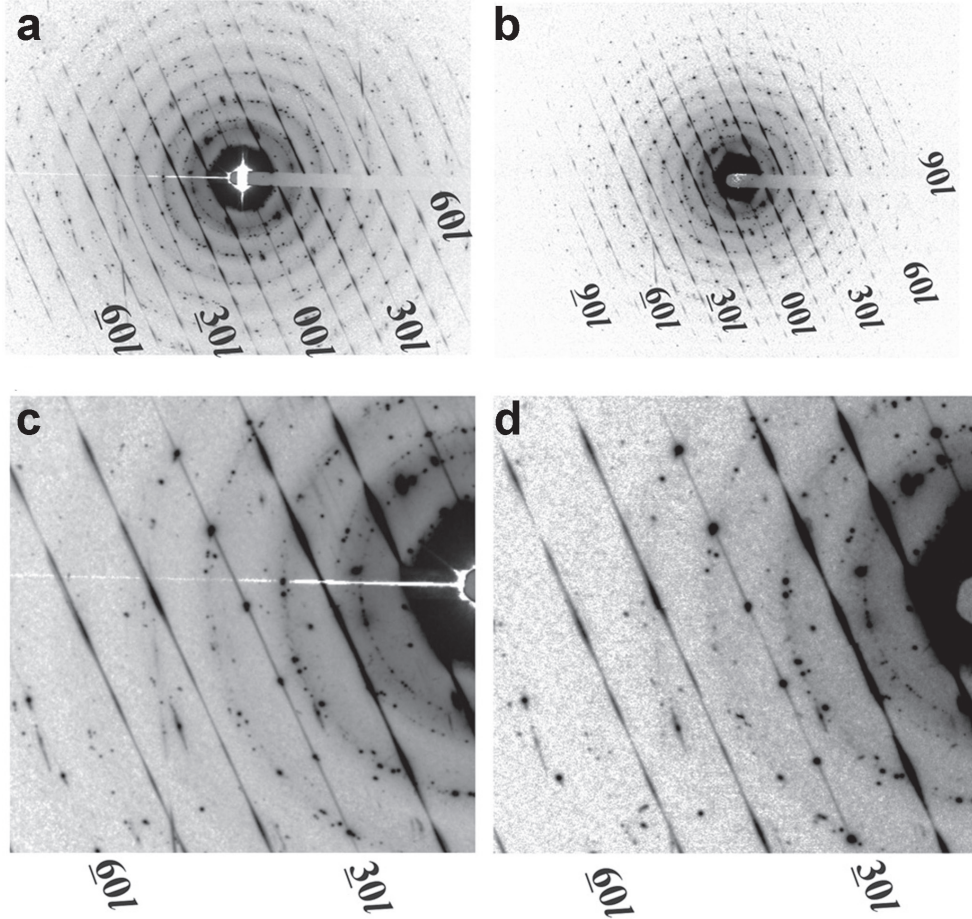
Figure 2.2. Diffraction patterns taken from the same crystal at 27 keV ((a) and (c)) and 38 keV ((b) and (d)). The same area on the detector is presented in the overall views ((a) and (b)). The close-ups of the diffraction patterns ((c) and (d)) present comparable areas of the reciprocal space. The white horizontal stripe in (a) and (c) is an artifact of background subtraction.

performed on the same system, in order to compare with the experiments carried out at 12.4 keV (figure 2.1b). With higher energies, the scattering cross-section of particles rapidly decreases. For any of the Bragg spots, it can be shown that in the kinematic (*i.e.* single scattering) approximation the diffracted power is inversely proportional to the square of the photon energy according to[35]

$$P_{hkl} = \frac{L\Lambda}{L_{hkl}^2} P_0 \qquad (2.2)$$

where Λ is a measure of the range of positional correlations in the crystal, L is the crystal depth along the beam and

$$L_{hkl} = \left[\lambda n r_0 Z \sqrt{F\left(\mathbf{q}_{hkl}\right)} \right]^{-1} \qquad (2.3)$$

22

is a characteristic length that is a measure for the diffraction power. Here, λ is the X-ray wavelength, n is the colloid number density, r_0 is the Thompson radius, which describes the strength of the scattering by a single electron, Z is the excess number of electrons per particle relative to the solvent and $F(\mathbf{q}_{hkl})$ is the normalized particle form factor at the Bragg spot. For a Bragg rod, where diffraction is more spread out than in a Bragg spot, it can be shown that a similar relation holds[11] for the power scattered into a certain portion of the rod (e.g., between l and l+1). The main difference is that the length of the positional correlations, Λ, is now governed by the typical size of islands of the same stacking rather than by the size of the whole crystal.[23, 24] If the power of the diffracted beam, P_{hkl}, is considered to be the source of further diffraction, the following relation between the intensity of primary diffraction P_{hkl} *versus* secondary diffraction P_{sec} is obtained in the case that only one diffraction channel contributes.
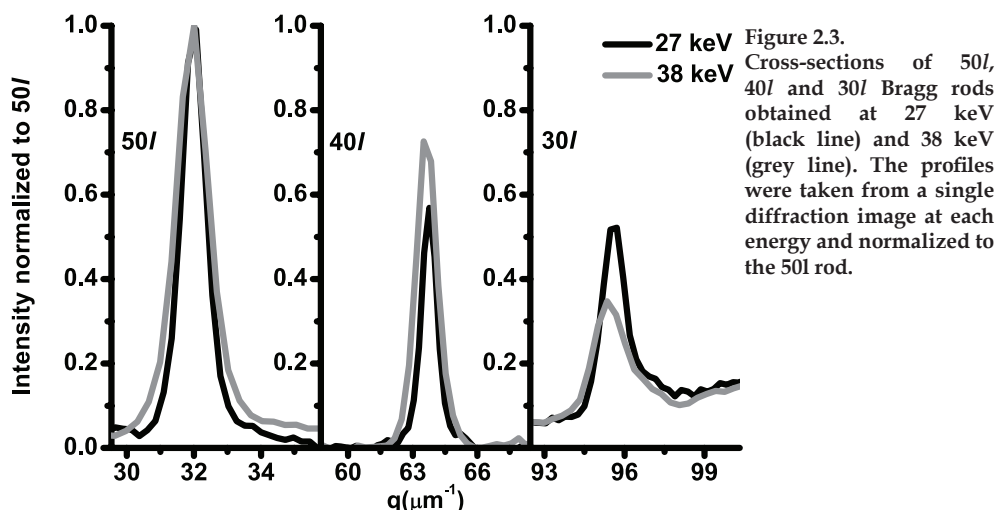
$$P_{sec} = \frac{1}{2} \frac{L\Lambda}{L_{hkl}^2} P_{hkl} = \frac{1}{2} \left(\frac{L\Lambda}{L_{hkl}^2} \right)^2 P_0 \tag{2.4}$$

Because of the dependence of the characteristic length L_{hkl} on the photon energy, the ratio between the secondary and the primary diffraction should decrease with the square of the energy.

In the present case of small-angle X-ray diffraction the Ewald sphere is very flat, so that numerous reflections are simultaneously present. In this case, one would need to sum over multiple diffraction channels, although the wavelength dependence remains the same. When the secondary Bragg Rods are indeed due to multiple diffraction, their intensity should be reduced by a factor of almost 10 upon increasing the photon energy from 12.4 to 38 keV. Figure 2.2 shows diffraction patterns recorded at 27 (Figure 2a and c) and 38 keV (figure 2.2b and 2.2d). Both patterns were measured on the same crystal with the same orientation. The separation between the peaks is slightly larger for the lower energy picture, as the angle of diffraction scales with the inverse of the energy. In both pictures, the 00l, 30l rods are still visible, but their intensities have significantly decreased with respect to the pattern measured at 12.4 keV. A quantitative comparison with figure 2.1b is, however, not possible, because the patterns were not recorded in the same crystal. The parameters L and Λ in equation 2.2, which represent crystal size and positional correlation length, respectively, may differ between crystals, resulting in significant changes in secondary diffraction. Still, the same capillaries were used for different measurements, keeping L approximately constant. The patterns in figure 2.2 are measured from the same crystal. Figure 2.3 shows cross-sections of the 50l, 40l and 30l rods displayed in figure 2.2c and 2.2d. Both 50l and 40l rods are generated through diffuse scattering from stacking disorder in the measured crystal. To investigate the origin of the 30l rod, the intensities of the three rods

Figure 2.3.
Cross-sections of 50*l*, 40*l* and 30*l* Bragg rods obtained at 27 keV (black line) and 38 keV (grey line). The profiles were taken from a single diffraction image at each energy and normalized to the 50l rod.

were compared as function of photon energy. The intensities were normalized by setting the maximum intensity of the 50*l* rod to 1. The width of the rods recorded at 38 keV is slightly larger than at 27 keV due to the limited resolution of the detector. When resolution limited data is obtained at both energies, the rescaling of data to the same **q**-scale enlarges the width of the 38 keV data with respect to the 27 keV data. After rescaling, the intensities of the 40*l* rods and the 20*l* rods (not shown) correspond well with each other. The intensity of the 30*l* rod, however, is clearly smaller for the high energy data. According to equation 2.4, the 30*l* rod should lose 50% intensity upon increasing the energy from 27 to 38 keV. Although the measurements are not accurate enough to be quantitative, the reduction is of the right order of magnitude. This result indicates that the secondary Bragg rods are, at least in part, due to multiple scattering.

2.4   CONCLUSIONS

In addition to the commonly discussed Bragg rods that give information about the stacking order in the close-packed crystal structures, the diffuse scattering is also observed along the secondary Bragg rods at ''forbidden'' **q**-values. By recording the diffraction patterns at several photon energies it was shown that their presence can, at least partly, be explained by multiple scattering. The intensities of these multiple-scattering-induced secondary Bragg rods can be reduced by using higher X-ray photon energies. Our results indicate that multiple scattering has to be taken into account in the analysis of the X-ray diffraction patterns in highly ordered colloidal crystals despite the small scattering cross section of a single sphere.

2.5   REFERENCES

[1] A. Guinier, X-Ray Diffraction in Crystals, Imperfect Crystals, and Amorphous Bodies, Dover Publications, New York **1994**.

[2] M. Holt, M. Sutton, P. Zschack, H. Hong, T. C. Chiang, Phys. Rev. Lett., **2007**, 98.

[3] B. T. M. Willis, A. W. Pryor, Thermal Vibrations in Crystallography, Cambridge University Press, London **1975**.

[4] P. Olmer, *Acta Crystallogr.,* **1948**, 1, 57.

[5] R. Q. Xu, T. C. Chiang, *Z. Kristallogr.,* **2005**, 220, 1009.

[6] A. Bosak, D. Chernyshov, *Acta Crystallogr. A,* **2008**, 64, 598.

[7] A. Bosak, M. Hoesch, M. Krisch, D. Chernyshov, P. Pattison, C. Schulze-Briese, B. Winkler, V. Milman, K. Refson, D. Antonangeli, D. Farber, *Phys. Rev. Lett.,* **2009**, 103.

[8] M. E. Wall, S. E. Ealick, S. M. Gruner, *P. Natl. Acad. Sci. USA,* **1997**, 94, 6180.

[9] A. J. C. Wilson, X-Ray Optics, Methuen & Co. Ltd., London **1949**.

[10] W. L. Vos, M. Megens, C. M. Van Kats, P. Bosecke, *Langmuir,* **1997**, 13, 6004.

[11] A. V. Petukhov, I. P. Dolbnya, D. G. A. L. Aarts, G. J. Vroege, H. N. W. Lekkerkerker, *Phys. Rev. Lett.,* **2003**, 90, 028304.

[12] P. G. Bolhuis, D. Frenkel, S. C. Mau, D. A. Huse, *Nature,* **1997**, 388, 235.

[13] S. C. Mau, D. A. Huse, *Phys. Rev. E,* **1999**, 59, 4396.

[14] P. N. Pusey, W. Van Megen, P. Bartlett, B. J. Ackerson, J. G. Rarity, S. M. Underwood, *Phys. Rev. Lett.,* **1989**, 63, 2653.

[15] J. Zhu, M. Li, R. Rogers, W. Meyer, R. H. Ottewill, STS-73 Space Shuttle Crew, W. B. Russel, P. M. Chaikin, *Nature,* **1997**, 387, 883.

[16] W. K. Kegel, J. K. G. Dhont, *J. Chem. Phys.,* **2000**, 112, 3431.

[17] V. C. Martelozzo, A. B. Schofield, W. C. K. Poon, P. N. Pusey, *Phys. Rev. E,* **2002**, 66.

[18] I. P. Dolbnya, A. V. Petukhov, D. G. A. L. Aarts, G. J. Vroege, H. N. W. Lekkerkerker, *Europhys. Lett.,* **2005**, 72, 962.

[19] C. Dux, H. Versmold, *Phys. Rev. Lett.,* **1997**, 78, 1811.

[20] H. Versmold, *Phys. Rev. Lett.,* **1995**, 75, 763.

[21] A. J. C. Wilson, *Proc. Roy. Soc. London, Ser. A,* **1942**, 180, 277.

[22] J. Hilhorst, V. V. Abramova, A. Sinitskii, N. A. Sapoletova, K. S. Napolskii,

A. A. Eliseev, D. V. Byelov, N. A. Grigorieva, A. V. Vasilieva, W. G. Bouwman, K. Kvashnina, A. Snigirev, S. V. Grigoriev, A. V. Petukhov, *Langmuir,* **2009**, 25, 10408–10412.

[23] J. M. Meijer, V. W. A. De Villeneuve, A. V. Petukhov, *Langmuir,* **2007**, 23, 3554.

[24] P. S. Miedema, V. W. A. de Villeneuve, A. V. Petukhov, *Phys. Rev. E,* **2008**, 77.

[25] J. M. Cowley, Diffraction Physics, North Holland, Amsterdam **1981**.

[26] A. G. F. de Beer, A. V. Petukhov, *J. Appl. Crystallogr.,* **2007**, 40, 144.

[27] N. A. M. Verhaegh, D. Asnaghi, H. N. W. Lekkerkerker, *Physica A,* **1999**, 264, 64.

[28] M. Borsboom, W. Bras, I. Cerjak, D. Detollenaere, D. G. van Loon, P. Goedtkindt, M. Konijnenburg, P. Lassing, Y. K. Levine, B. Munneke, M. Oversluizen, R. van Tol, E. Vlieg, *J. Synchrotron Radiat.,* **1998**, 5, 518.

[29] *http://www.esrf.fr/usersandscience/experiments/structmaterials/id11*.

[30] M. Drakopoulos, A. Snigirev, I. Snigireva, J. Schilling, *Appl. Phys. Lett.,* **2005**, 86.

[31] V. Kohn, I. Snigireva, A. Snigirev, *Opt. Commun.,* **2003**, 216, 247.

[32] A. V. Petukhov, J. H. J. Thijssen, D. C. 't Hart, A. Imhof, A. Van Blaaderen, I. P. Dolbnya, A. Snigirev, A. Moussaid, I. Snigireva, *J. Appl. Crystallogr.,* **2006**, 39, 137.

[33] A. Snigirev, V. Kohn, I. Snigireva, B. Lengeler, *Nature,* **1996**, 384, 49.

[34] A. Snigirev, I. Snigireva, G. Vaughan, J. Wright, M. Rossat, A. Bytchkov, C. Curfs, *9th International Conference on X-Ray Microscopy,* **2009**, 186.

[35] A. V. Petukhov, I. P. Dolbnya, D. G. A. L. Aarts, G. J. Vroege, *Phys. Rev. E,* **2004**, 69.

3

Intrinsic Stacking Faults in Convectively Assembled Crystals of Colloidal Spheres

Using microradian X-ray diffraction, the crystal structure of convectively assembled colloidal photonic crystals was investigated over macroscopic (0.5 mm) distances. Through adaptation of Wilson's theory for X-ray diffraction, certain types of line defects that are often observed in scanning electron microscopy images of the surface of these crystals are shown to be intrinsic stacking faults at 70.5° angles with the substrate. These defects consist of two parallel hexagonal close packed planes in otherwise face centred cubic crystals. Measurements indicate that these stacking faults cause at least 10 percent of stacking disorder.

3.1   INTRODUCTION

Synthesis of high quality colloidal crystals by convective assembly is a promising pathway towards the fast, cheap production of 3D photonic crystals.[1-3] In this process, a dispersion containing a low concentration of monodisperse colloids is slowly evaporated. This causes the colloids to self-assemble onto a substrate that is standing or suspended in the dispersion.

Because the crystal structure is of vital importance to the optical properties of the material, much effort has been spent on finding equilibrium crystal structures[4-8] and the mechanisms of crystal growth.[9-12] It is generally accepted that for convectively assembled crystals the dominant structure resulting from experiments is face centered cubic (fcc),[2, 9, 10] although the growth mechanism is still under investigation.[3, 9, 13]

Just as vital as the crystal structure is the presence of defects in a crystal. On the one hand, uncontrolled incorporation of defects can easily degrade the optical properties. [14-17] On the other hand, defect engineering allows one to gain control of light propagation.[18, 19] Despite the importance of defects for crystal properties, few studies focus on the intrinsic disorder in colloidal crystals.[10, 12, 15]

As discussed in chapter 1, several types of defects common to colloidal crystals can be distinguished. First of all, the crystals contain a high concentration of point defects. The absence of an attractive interparticle potential and the presence of polydispersity[20] cannot fully account for experimentally observed densities of vacancies and interstitials so that the kinetics of crystal growth should be involved. [10] Secondly, dislocations are also present in large quantities.[12, 21] Due to the low stacking fault energy (on the order of 10^{-3} k_BT per particle[5] in the thermodynamic limit) these linear defects often split up in Shockley partial dislocations accompanied by stacking faults, a third type of defect. Both the lattice distortions around a (partial) dislocation and the presence of stacking faults affect the optical properties of colloidal crystals.[15, 17] It is therefore necessary to fully characterize these types of disorder in order to find ways to control them.

Up until recently, the structure of convectively assembled crystals was mostly addressed using electron[8-12, 22] or confocal optical[9, 10] microscopy, which can be applied to rather limited sample volumes and have limitations in sample penetration depth. The micro-optical spectroscopy technique[11, 12, 23] is able to unravel the stacking order parallel to the substrate over a macroscopically large sample but was only applied to thin crystals consisting of a few layers and does not provide information about other stacking directions. Laser diffraction is often complicated by a high refractive index contrast. Moreover, it can only be applied to the study of periodic structures with a sufficiently large periodicity,[24, 25] as the laser wavelength has to be less than twice as small as the lattice periodicity in order

to fulfil the Bragg condition in diffraction measurements.

In order to be able to characterize large crystalline areas and have access to a broad **q**-range X-ray diffraction with microradian resolution is the method of choice in this study. Using this technique, the presence of a previously undefined type of defect is demonstrated in convectively assembled crystals of polystyrene spheres. The diffraction data are supplemented by electron and atomic force microscopy.

3.2   EXPERIMENTAL

Colloidal crystals made of 425 nm polystyrene microspheres (relative standard deviation < 5%) were grown by the convective assembly technique.[1-3, 9-12] The spheres were synthesized by emulsifier-free emulsion polymerization of styrene using potassium persulphate as initiator.[26] Glass microscope slides were immersed in an aqueous suspension of microspheres with a volume fraction of about 0.5%. The growth temperature was 50 °C and the obtained crystal thickness was about 15-20 layers.

Ni photonic crystals with an inverse opal structure were fabricated by using similar colloidal crystals as templates.[27] These were assembled onto a thin conductive gold layer evaporated on a mica substrate. Convective assembly of colloids was followed by electrochemical deposition of nickel into the voids between the spheres in a three-electrode cell at room temperature. The counter electrode was a Pt wire and the reference electrode was a saturated Ag/AgCl electrode connected to the cell via a Luggin capillary; 0.1 M $NiCl_2$, 0.6 M $NiSO_4$, 0.3 M H_3BO_3 and 3.5 M C_2H_5OH solution was used for potentiostatic Ni deposition at a potential of E_d = –0.9V versus the Ag/AgCl reference electrode. The polystyrene microspheres were subsequently dissolved in toluene.

Scanning electron micrographs of polystyrene and Ni crystals were recorded on a LEO Supra VP 50 instrument. Atomic force microscopy (AFM) images were recorded in tapping mode using a Digital Instruments Nanoscope IIIa atomic force microscope and Nanosensors Point Probe Plus NCH 50 silicon tips.

X-ray studies were performed at the Dutch-Belgian beamline BM-26 DUBBLE of the European synchrotron radiation facility (ESRF) in Grenoble, France. A microradian X-ray diffraction setup similar to the one described in Refs.[28] and [29] was used. In brief, to achieve maximum transverse coherence length of the beam at the sample, any focusing of the beam before the experimental hutch was avoided. Instead, a set of beryllium compound refractive lenses (CRLs)[30] was positioned only just before the sample, in the experimental hutch, to focus the X-ray beam. Focal point was the phosphor screen of the CCD (charge-coupled device) X-ray detector (Photonic Science, 4008x2671 pixels of 22 µm squared) located at a distance of 8 m from the lens. Using computer-controlled motorized rotation and

translation stages the sample orientation (around two axes orthogonal to the beam) and its position (in two directions orthogonal to the beam) could be remotely changed. An X-ray photon energy of 13 keV (wavelength λ=0.095 nm) was used. The beam diameter in the sample was 0.5 mm. This setup allows achieving an angular resolution (full-width-at-half-maximum) of the order of 5 microradians, corresponding to $3.3 \cdot 10^{-4}$ nm^{-1} in reciprocal space.

3.3   THEORY

To model the recorded data a model similar to the one described by Paterson was employed.[31] It is assumed that a crystal consists of hexagonal close-packed planes contained in the (x, y) plane, that are stacked in the z direction to form a close-packed structure. The interlayer separation is therefore $d\sqrt{2/3}$, where d is the nearest-neighbor distance equal to the particle diameter. We also assume that with a probability β every subsequent layer is shifted by a distance $d/\sqrt{3}$ in the positive x-direction relative to the layer below. Correspondingly, $(1-\beta)$ is the chance of shifting the layer in the negative x-direction. This is illustrated schematically in figure 3.1a. For β = 0.5 this model is equivalent to the model of Wilson[32] with α = 0.5 (random stacking with equal chances of fcc and hcp sequences). The two limiting cases of small β and β close to 1 correspond to a small density of intrinsic stacking faults and a dominating fcc stacking of either the ABCABC or the ACBACB type. In the reciprocal space we introduce basis vectors

$$\mathbf{b}_1 = \frac{2\pi}{d}\left(\sqrt{1/3}, 1, 0\right),$$

$$\mathbf{b}_2 = \frac{2\pi}{d}\left(-\sqrt{1/3}, 1, 0\right), \qquad\qquad (3.1)$$

$$\mathbf{b}_3 = \frac{2\pi}{d}\left(0, 0, \sqrt{3/2}\right)$$

and represent any diffraction vector $\mathbf{q}$ using the h, k and l indices:
$$\mathbf{q} = h\mathbf{b}_1 + k\mathbf{b}_2 + l\mathbf{b}_3 \qquad\qquad (3.2)$$

Note that these hkl indices do not correspond to the usual notations for face centered cubic crystals, but indicate directions along the basis vectors in reciprocal space (as shown in equation 3.1). The plane defined by $\mathbf{b}_1$ and $\mathbf{b}_2$ is parallel to the x, y plane, while $\mathbf{b}_3$ lies parallel to the z-direction. Due to the periodic intralayer hexagonal structure, diffraction can only be observed for integer values of h and k. In the direction along $\mathbf{b}_3$, intensity can be found for every real value of l. In structures containing stacking faults, this results in extended rods of scattered intensity along b_3 at integer h and k values, with a structure factor $S_{hk}(l)$. These are
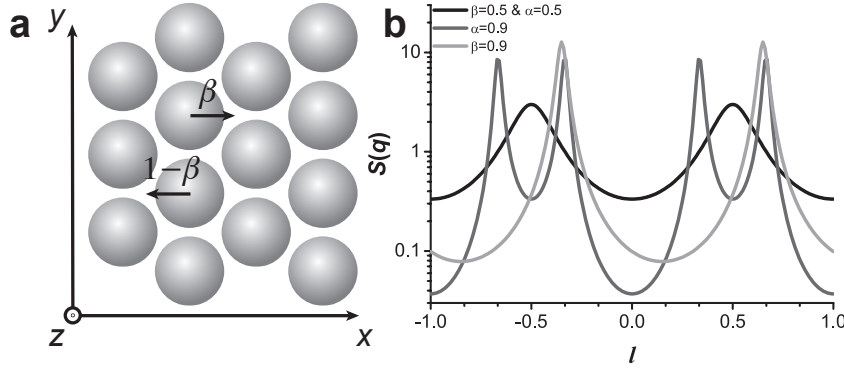
Figure 3.1. (a) Illustration showing the stacking directions as described in the main text. Layers are stacked to the right with a probability β and to the left with a probability 1 - β. Panel (b) shows the structure factor profiles S10(l) along the (10) Bragg rod calculated within Wilson's theory for α = 0.9 (dark grey) and within the present model for β = 0.9 (light grey). For comparison the profile for $\alpha = \beta = 0.5$ is also presented (black).

referred to as Bragg rods.

The diffracted intensity $I(\mathbf{q}) \propto F(\mathbf{q})S(\mathbf{q})$ is proportional to the product of the form factor $F(\mathbf{q})$ (scattering by individual particles without positional correlations) and the structure factor $S(\mathbf{q})$ (arising from the interparticle positional correlations). In the model, each layer is assumed to contribute equally to the total structure factor. The absolute value of the contribution of every single layer to $S(\mathbf{q})$ is set to unity. The variation of the structure factor along a Bragg rod is a result of interference of the contributions of different layers. The phase of the contribution of the n-th layer

$$\Delta\varphi_n = \mathbf{q}_{xy}\rho_n + q_z z_n \qquad (3.3)$$

depends on the lateral position ρ_n and its position in the direction perpendicular to the layers, z_n. The structure factor can be written as

$$S_{hk}(l) = \frac{1}{N}\left|\sum_n e^{i\Delta\varphi_n}\right|^2 = \frac{1}{N}\sum_n\sum_m e^{i\Delta\varphi_n}e^{-i\Delta\varphi_{n+m}} = \left\langle\sum_m e^{i\Delta\varphi_m}\right\rangle_n \qquad (3.4)$$

where $\Delta\varphi_m = \Delta\varphi_n - \Delta\varphi_{n+m}$ and the angular brackets $<...>_n$ denote averaging over possible layer arrangements around a (randomly chosen) layer n. Using equations 3.1, 3.2 and 3.3 one can show that the phase shift between n-th and ($n+m$)-th layer is given by

$$\Delta\varphi_m(j) = \frac{2\pi}{3}(h-k)(m-2j) + 2\pi l m \qquad (3.5)$$

where j is the number of shifts in the negative x-direction. For a given value of β such a situation occurs with the probability

$$\binom{m}{j}(1-\beta)^j\beta^{m-j} \qquad (3.6)$$

31

where

$$\binom{m}{j} = \frac{m!}{j!(m-j)!} \tag{3.7}$$

is the number of possible realizations of having j and $(m-j)$ shifts in the negative and positive x-direction, respectively. For $m \geq 0$ the average contribution to the structure factor of a layer m steps away from a randomly chosen layer n is thus given by

$$S_{hk}^{(m)}(l) = \sum_{j=0}^{j=m} \binom{m}{j}(1-\beta)^j \beta^{m-j} \exp\left[\frac{2\pi i}{3}(h-k)(m-2j)\right]\exp[2\pi i l m]$$

$$= \left\{(1-\beta)\exp\left[-2\pi i\frac{(h-k-3l)}{3}\right] + \beta\exp\left[2\pi i\frac{(h-k+3l)}{3}\right]\right\}^m \tag{3.8}$$

For $m < 0$ one can use the fact that $S_{hk}^{(m)}(l) = \left[S_{hk}^{(-m)}(l)\right]^*$

The total structure factor along the Bragg rod is thus

$$S_{hk}(l) = \sum_{m=-\infty}^{m=\infty} S_{hk}^{(m)}(l) = 2\,\mathrm{Re}\left[\sum_{m=0}^{m=\infty} S_{hk}^{(m)}(l)\right] - 1 \tag{3.9}$$

Since $S_{hk}^{(m)}(l)$ form a simple geometrical series, the sum in equation 3.9 can be calculated to yield

$$S_{hk}(l) = \mathrm{Re}\left\{\frac{1+\exp\{2\pi i[l-(h-k)/3]\}\{1-\beta+\beta\exp[4\pi i(h-k)/3]\}}{1-\exp\{2\pi i[l-(h-k)/3]\}\{1-\beta+\beta\exp[4\pi i(h-k)/3]\}}\right\} \tag{3.10}$$

For $(h-k)$ divisible by 3 equation 3.10 yields δ-function-like Bragg spots at integer values of l independently of the value of β. These reflections are independent of the stacking sequence and are not broadened by stacking disorder. For $(h-k)$ not divisible by 3 the $S_{hk}(l)$ profile sensitively depends on β. This is further illustrated in figure 3.1b for the $S_{10}(l)$ rod. As expected, the present model with $\beta = 0.5$ yields exactly the same result as Wilson's theory with $\alpha = 0.5$. In this case both models predict

$$S_{50\%}(l) = \frac{3}{5+4\cos(2\pi l)} \tag{3.11}$$

The result of Wilson's theory for $\alpha = 0.9$ (10% of hcp planes) is compared with the outcome of the present model with $\beta = 0.9$ (approximately the same average size of the fcc domains). Note that in the latter case ($\beta = 0.9$) the percentage of hcp planes, which equals $2\beta(1-\beta) = 18\%$, is almost twice as high as in the Wilson theory with $\alpha = 0.9$ because every slip defect creates two hcp planes unless two slip
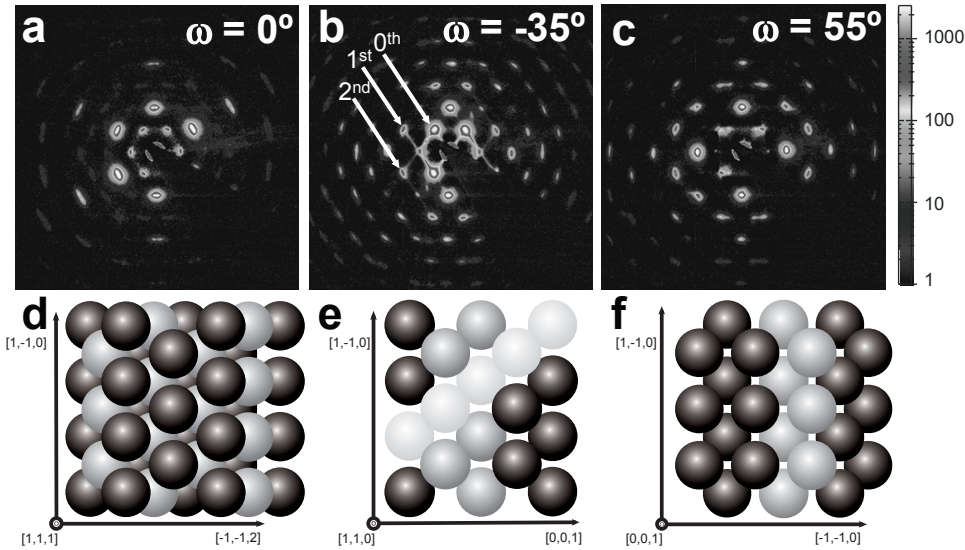
Figure 3.2. Microradian X-ray diffraction patterns measured with X-ray beam orthogonal to the substrate ($\omega = 0°$) and after a sample rotation around the vertical axis by $\omega = -35°$ and $\omega = 55°$ are shown in panels (a)-(c). The arrows in (b) point onto a set of Bragg rods of different order. A similar set of rods runs from the bottom left to the top right of the same image. The intensity scaling is explained in the scale bar next to panel (c). (d)-(f) represent real space fcc crystals with orientations corresponding to the diffraction images above them. Note that the real space structures correspond to perfect fcc lattices, while panels (a)-(c) represent measurements on real (faulted) crystals. The grey spheres form a (111) plane parallel to the substrate in panels (d)-(f). The light grey spheres in (e) highlight a (1-11) plane on which the stacking disorder in (b) is measured.

defects occur one after the other.

3.4   RESULTS & DISCUSSION

Figure 3.2a-c present examples of microradian diffraction patterns measured for different orientations of as-grown crystals of polystyrene spheres, corresponding to incidence of the X-ray beam along the [111], [110] and [001] crystallographic fcc directions, respectively, where the [111] direction runs perpendicular to the substrate. The corresponding views of a perfect fcc crystal in real space are shown in figure 3.2d-f. The dark grey spheres packed between the black spheres in all three images are particles belonging to a single (111) plane parallel to the substrate.

In the diffraction patterns, one can clearly identify a large number of reflections, that can be assigned to the reciprocal lattice of the ideal fcc crystal structure. The four-fold symmetry of the pattern in figure 3.2c and the equal intensity of the four reflections of the 220 family suggest that a single fcc domain is illuminated. Visual inspection of the crystals revealed the vertical stripe pattern that is typical for convectively assembled crystals. These stripes originate from single fcc domains[33,
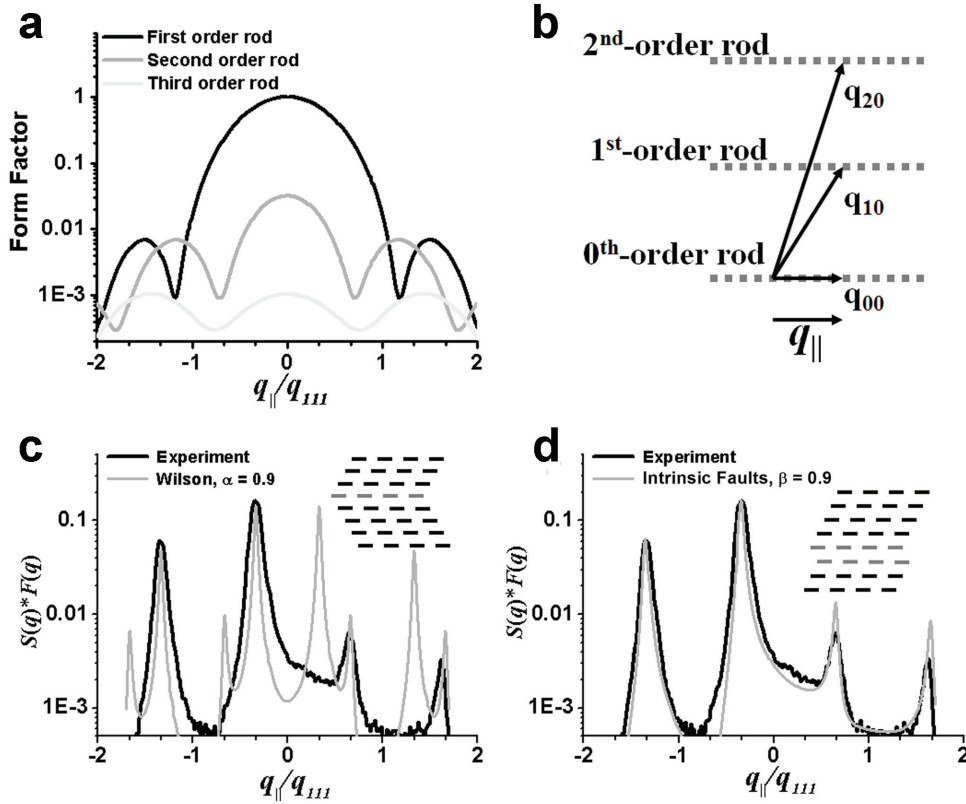
33

Figure 3.3. Panel (a) shows the variation of the form factor of 5% polydisperse spheres along the Bragg rods. The difference in the length of the wavevector for the same value of $q_\parallel$ for different Bragg rods is illustrated in (b). Panel (c) presents the profile of the scattering intensity along a first order Bragg rod. The experimental result (black) is compared with a profile calculated within Wilson's theory (grey). In (d), the same result is compared to a profile calculated within the model discussed in the main text, which allows only for intrinsic stacking faults. The possible layer sequences in Wilson's theory and the present model are shown in the insets of (c) and (d), respectively.

[34] and have a width of approximately the same size as the X-ray beam, confirming the possibility of obtaining diffraction data from a single domain.

In addition to the sharp Bragg peaks, one can also see two sets of Bragg rods in figure 3.2b, which do not fit the ideal fcc crystal structure. These rods are parallel to <111> crystallographic directions and indicate the presence of planar defects, *i.e.* stacking faults in hexagonal layers making an angle of 70.5° with the substrate. One of these close packed {111} planes is indicated in light grey in figure 3.2e.

As discussed in chapter 2, the 0th-order rods passing through the origin of the reciprocal space can at least in part be explained by multiple diffraction. It was shown that the intensity of multiple diffraction increases with the square of the crystal thickness. As the crystals investigated here are ~10 times thinner than the

ones in chapter 2, the intensity of 0th-order rods should be two orders of magnitude smaller. The fact that they are still clearly visible indicates that there may be another factor contributing to their intensity. It is possible that they are induced by distorted periodicity between the {111} planes, for example by lattice distortions around a dislocation line or small cracks in the crystals. The visibility of the 0th-order rods is further enhanced by a large form factor *F(q)* relative to the 1st and 2nd-order rods (figure 3.3a), indicating an even smaller contribution from the structure factor. They are therefore not related to the strongest type of disorder in between the {111} planes. The form factor of the 1st- and the 2nd-order Bragg rods is much smaller (figure 3.3a), due to larger value of the scattering vector (figure 3.3b). Their relatively high intensity therefore originates from a high structure factor, caused by stacking disorder in between the close-packed planes of colloidal spheres.[35, 36]

From the intensity distribution along the 1st and 2nd order Bragg rods, information can be obtained about the structure of the crystal under investigation. This intensity distribution is usually described by Wilson's theory,[32] which assumes that a crystal consists of an arbitrary sequence of close packed layers in A, B and C position, with a probability *α* of finding an fcc layer. The value of *α* uniquely determines the distribution of scattering intensity along a Bragg rod. Figure 3.3c shows the measured intensity profile along a 1st-order Bragg rod as highlighted in figure 3.3b. It also shows a profile that was calculated within Wilson's theory for a crystal with dominant fcc stacking (*α* = 0.9). It is clear that the theory predicts two times as many maxima as observed experimentally. The reason for this discrepancy is related to the fact that in the Wilson model a single hcp layer causes twinning of a crystal (figure 3.3c, inset), giving rise to an additional set of Bragg reflections along the Bragg rod. The measurements, however, suggest that only one growth direction dominates. This can only happen if stacking disorder is caused by pairs of hcp layers. Such intrinsic stacking faults are in fact equivalent to sliding one part of a perfect fcc crystal relative to the other part along a {111} slip plane, creating two hcp layers bordering this plane (figure 3.3d, inset).

To fit the data correctly, Wilson's theory was modified to account for intrinsic stacking faults only.[31] As described in detail in the theory section, it is assumed that with respect to a reference layer, every subsequent layer is stacked in the positive *x*-direction with a certain probability *β* (as shown in figure 3.1a). For high values of *β* (or analogously, 1-*β*), the majority of layers will be stacked in the positive (negative) *x*-direction, with only a small fraction of layers stacked the other way, creating the intrinsic stacking faults.

A summation over the scattering contributions of all layers averaged over all possible stacking realizations yields the statistically-averaged structure factor profile along a 1st-order Bragg rod in the form

$$S_{10}(z) = \text{Re}\left(\frac{1+z}{1-z}\right) \hspace{3cm} (3.12)$$

where $z = \exp\left[2\pi i\left(q_{\parallel}/q_{111} - 1/3\right)\right]\left[1 - \beta + \beta \exp\left(4\pi i/3\right)\right]$. The intensity profile along the first-order Bragg rod, calculated with the modified theory for $\beta = 0.9$ (figure 3.3d), closely follows the experimental result. This fit confirms the predominant fcc stacking found by others,[3, 9, 11] albeit with a significant amount of stacking disorder in directions other than perpendicular to the substrate.

The presence of pairs of hcp layers in hexagonal planes at an angle with the substrate should lead to apparent line defects with a square sphere arrangement in the hexagonal layers parallel to the substrate as illustrated in figure 3.4. This exactly corresponds to the observation in figure 3.5a, where an electron micrograph of the top surface of a colloidal crystal is displayed. One can clearly see the lines of square-like particle arrangement, that are typically observed at the surface of convectively assembled colloidal crystals.[15, 22] The diffraction data suggest that these lines are in fact manifestations of planar defects.

In figure 3.5b a top view of a nickel inverted crystal is shown.[27] It is not surprising that the defects are also found here. Through the cavities a similar defect is observed in the layer below the top layer, confirming the conclusion that the line defects at the surface of colloidal crystals are in fact manifestations of intrinsic stacking faults. Their presence in inverted crystals is also supported by X-ray results (not shown). The X-ray data obtained from the inverted crystal are similar to that presented in figure 3.3, with similar sets of Bragg rods at $\omega=\pm35°$.

The slip vector for formation of the hcp planes not only moves the particles along the substrate to the positions of square coordination, but also has a component perpendicular to the surface (figure 3.4), leading to a height difference of 1/3 of the interplanar spacing in the
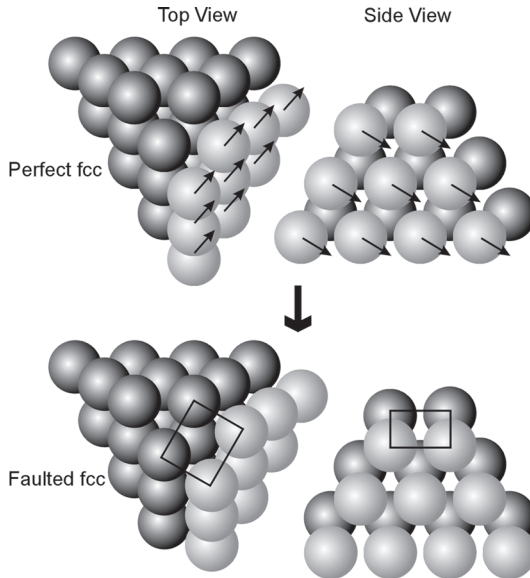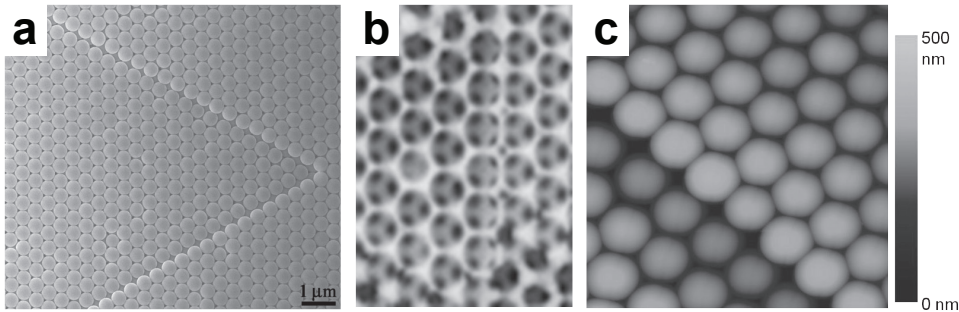

Figure 3.4. The top figures show a perfect fcc crystal, with the arrows indicating the direction of movement of the light grey {111} plane in the slip direction. The bottom figures illustrate the resulting structure. In the top view, the square packing of the particles can be observed. The side view shows the structure along the <111> direction perpendicular to the slip plane, illustrating that the resulting structure is still close-packed.

Figure 3.5. Panel (a) shows a scanning electron microscopy (SEM) image of a colloidal crystal with the same orientation as during growth: The gravity direction runs from the top to the bottom of the figure. Two merging "line" defects can be observed, forming a locked stair-rod dislocation. Panel (b) is a zoom into the region of an intrinsic stacking fault in a SEM image of the surface of a Ni inverted crystal. Notice the square arrangement of the air voids in the top layer and in the layer below with a lateral shift in between them. In an AFM image (c), the surface step at a defect is clearly visible. The vertical bar gives the height scale. The periodicity in (b) and (c) is the same as that of the colloidal crystal shown in (a).

direction along the surface normal. This height difference was confirmed by AFM measurements (figure 3.5c). The square configuration of the particles at a defect, as well as the height step can be seen very clearly in this picture.

The fact that a height difference between two parts of a crystal is observed at their surface is not trivial. This difference must originate either at the substrate, or somewhere in the crystal. Since height variations on a substrate are typically much smaller than the diameter of the colloids used for growing a crystal, it is unlikely that the stacking fault originates there; it would either generate a large void underneath the crystal or cause strong lattice distortions. Both are energetically unfavourable. The second option is that the faults originate inside the crystal. In this case, they would have to originate at a dislocation. A crystal starting out from a perfect fcc structure in the bottom layers, could form a transition to a stacking fault via a Shockley partial dislocation.[37] The first few layers of a convectively assembled crystal are predominantly hcp stacked[9, 10] and contain a substantial concentration of Shockley partials influencing the stacking parallel to the substrate. [12] These Shockley partials could well be the nucleation point for the slanted faults, combining to a stair-rod dislocation, i.e. two stacking faults on different {111} planes meeting on a single dislocation line, as described in section 1.2. This is a structure that is regularly observed in crystals with low stacking fault energy, as the line energy of the dislocation is smaller than that of a single Shockley partial.[38] In chapter 7 the existence of these structures in sedimentary colloidal crystals will be further investigated.

3.5 CONCLUSIONS

In summary, colloidal crystals grown by convective assembly were studied with microradian X-ray diffraction, supported by scanning electron microscopy and atomic force microscopy. Cubic stacking order was found to be accompanied by intrinsic stacking faults at an angle of 70.5° with the substrate, which manifest themselves as line defects on the crystal surface. The presence of up to 10 percent of stacking disorder in at least two out of four <111> directions may cause a significant degradation of the crystal properties, which was previously neglected in characterizations of the structure of convectively assembled crystals.

3.6 REFERENCES

[1] P. Jiang, J. F. Bertone, K. S. Hwang, V. L. Colvin, *Chem. Mater.*, **1999**, 11, 2132.

[2] Y. A. Vlasov, X. Z. Bo, J. C. Sturm, D. J. Norris, *Nature,* **2001**, 414, 289.

[3] D. J. Norris, E. G. Arlinghaus, L. Meng, R. Heiny, L. E. Scriven, *Adv. Mater.*, **2004**, 16, 1393.

[4] P. G. Bolhuis, D. Frenkel, S. C. Mau, D. A. Huse, *Nature,* **1997**, 388, 235.

[5] S. C. Mau, D. A. Huse, *Phys. Rev. E,* **1999**, 59, 4396.

[6] P. N. Pusey, W. Van Megen, P. Bartlett, B. J. Ackerson, J. G. Rarity, S. M. Underwood, *Phys. Rev. Lett.,* **1989**, 63, 2653.

[7] J. Zhu, M. Li, R. Rogers, W. Meyer, R. H. Ottewill, STS-73 Space Shuttle Crew, W. B. Russel, P. M. Chaikin, *Nature,* **1997**, 387, 883.

[8] H. Miguez, F. Meseguer, C. Lopez, A. Mifsud, J. S. Moya, L. Vasquez, *Langmuir,* **1997**, 13, 6009.

[9] L. Meng, H. Wei, A. Nagel, B. J. Wiley, L. E. Scriven, N. D. J., *Nano Lett.,* **2006**, 6, 2249.

[10] H. Wei, L. Meng, Y. Jun, D. J. Norris, *Appl. Phys. Lett.,* **2006**, 89, 241913.

[11] X. Checoury, S. Enoch, C. Lopez, A. Blanco, *Appl. Phys. Lett.,* **2007**, 90, 161131.

[12] E. Vekris, V. Kitaev, D. D. Perovic, J. S. Aitchison, G. A. Ozin, *Adv. Mater.*, **2008**, 20, 1110.

[13] D. D. Brewer, J. Allen, M. R. Miller, J. M. de Santos, S. Kumar, D. J. Norris, M. Tsapatsis, L. E. Scriven, *Langmuir,* **2008**, 24, 13683.

[14] Z. Y. Li, Z. Q. Zhang, *Phys. Rev. B,* **2000**, 62, 1516.

[15] R. Rengarajan, D. Mittleman, C. Rich, V. Colvin, *Phys. Rev. E,* **2005**, 71, 016615.

[16] Y. A. Vlasov, V. N. Astratov, A. V. Baryshev, A. A. Kaplyanskii, O. Z. Karimov, M. F. Limonov, *Phys. Rev. E,* **2000**, 61, 5784.

[17] V. Yannopapas, N. Stefanou, A. Modinos, *Phys. Rev. Lett.,* **2001**, 86, 4811.

[18] P. V. Braun, S. A. Rinne, F. Garcia-Santamaria, *Adv. Mater.,* **2006**, 18, 2665.

[19] S. A. Rinne, F. Garcia-Santamaria, P. V. Braun, *Nature Photonics,* **2008**, 2, 52.

[20] S. Pronk, D. Frenkel, *J. Chem. Phys.,* **2004**, 120, 6764.

[21] J. M. Meijer, V. W. A. De Villeneuve, A. V. Petukhov, *Langmuir,* **2007**, 23, 3554.

[22] A. S. Sinitskii, P. E. Khokhlov, V. V. Abramova, T. V. Laptinskaya, Y. D. Tretyakov, *Mendeleev Commun.,* **2007**, 17, 4.

[23] H. J. Schöpe, A. Barreira Fontecha, H. Konig, J. Marques Hueso, R. Biehl, *Langmuir,* **2006**, 22, 1828.

[24] R. M. Amos, J. G. Rarity, P. R. Tapster, T. J. Shepherd, S. C. Kitson, *Phys. Rev. E,* **2000**, 61, 2929.

[25] A. Sinitskii, V. Abramova, T. Laptinskaya, Y. D. Tretyakov, *Phys. Lett. A,* **2007**, 366, 516.

[26] J. W. Goodwin, J. Hearn, C. C. Ho, R. H. Ottewill, *Colloid Polym. Sci.,* **1974**, 252, 464.

[27] K. S. Napolskii, A. Sinitskii, S. V. Grigoriev, N. A. Grigorieva, H. Eckerlebe, A. A. Eliseev, A. V. Lukashin, Y. D. Tretyakov, *Physica B,* **2007**, 397, 23.

[28] A. V. Petukhov, J. H. J. Thijssen, D. C. 't Hart, A. Imhof, A. Van Blaaderen, I. P. Dolbnya, A. Snigirev, A. Moussaid, I. Snigireva, *J. Appl. Crystallogr.,* **2006**, 39, 137.

[29] J. H. J. Thijssen, A. V. Petukhov, D. C. 't Hart, A. Imhof, C. H. M. Van der Werf, R. E. I. Schropp, A. Van Blaaderen, *Adv. Mater.,* **2006**, 18, 1662.

[30] A. Snigirev, V. Kohn, I. Snigireva, B. Lengeler, *Nature,* **1996**, 384, 49.

[31] M. S. Paterson, *J. Appl. Phys.,* **1952**, 23, 805.

[32] A. J. C. Wilson, *Proc. Roy. Soc. London, Ser. A,* **1942**, 180, 277.

[33] J. H. J. Thijssen, Ph. D. Thesis, Utrecht University, **2007**.

[34] L. C. Andreani, A. Balestreri, J. F. Galisteo-Lopez, M. Galli, M. Patrini, E. Descrovi, A. Chiodoni, F. Giorgis, L. Pallavidino, F. Geobaldo, *Phys. Rev. B,* **2008**, 78.

[35] H. Versmold, *Phys. Rev. Lett.,* **1995**, 75, 763.

[36] A. V. Petukhov, I. P. Dolbnya, D. G. A. L. Aarts, G. J. Vroege, H. N. W. Lekkerkerker, *Phys. Rev. Lett.,* **2003**, 90, 028304.

[37] P. Schall, I. Cohen, D. A. Weitz, F. Spaepen, *Science,* **2004**, 305, 1944.

[38] D. Hull, D. J. Bacon, Introduction to Dislocations, fourth edn., Elsevier Ltd., Oxford **2001**.

Scanning Transmission X-Ray Microscopy as a Novel Tool to Probe Colloidal and Photonic Crystals

Photonic crystals consisting of nano- to micrometer-sized building blocks, such as multiple sorts of colloids, have recently received widespread attention. It remains a challenge, however, to adequately probe the internal crystal structure and the corresponding deformations that inhibit the proper functioning of such materials. It is shown that scanning transmission X-ray microscopy (STXM) can directly reveal the local structure, orientations, and even deformations in polystyrene and silica colloidal crystals with 30-nm spatial resolution. Moreover, STXM is capable of imaging a diverse range of crystals, including those that are dry and inverted, and provides novel insights complementary to information obtained by benchmark confocal fluorescence and scanning electron microscopy techniques.

Chapter 4: STXM for Probing Colloidal and Photonic Crystals

4.1   INTRODUCTION

The self-assembly of monodisperse colloidal particles is a promising method for fast and cheap production of photonic materials.[1-4] These materials hold promise for applications in telecommunications, solar-energy harvesting, and low-threshold lasing.[5] The convective assembly technique[1, 3, 4] is a well-established method to produce macroscopic colloidal crystals with a face-centered cubic (fcc) structure. Colloidal crystals obtained in this manner can be used as a template for making inverted photonic crystals of materials with a desired refractive index.[6] The inverted structure can then serve as a photonic crystal. In order to obtain crystals with a full photonic band gap, however, the fcc structure needs to be controlled since the photonic band gap is highly sensitive to stacking faults, dislocations, and other deformations.[7] To achieve perfect crystals, detailed knowledge about the crystal growth mechanism and resulting defect structures is required. The growth mechanism has received widespread attention over the last decade,[4, 8, 9] resulting in the proposal of several growth models, but experimental evidence supporting these models is lacking. Moreover, the defect structures themselves have hardly been investigated and the few reported studies indicate that the dominant fcc crystals still possess a significant degree of disorder resulting in disadvantageous effects on the properties of photonic crystals.[10, 11]

A serious obstacle in the study of defect structures is the absence of appropriate techniques that probe the internal structure of photonic crystals in three dimensions. The most widely applied technique is scanning electron microscopy (SEM) but this technique is inherently surface specific. The only possibility for studying parts of the crystal internal structure by SEM is through physically cutting crystals apart and studying their cut edges.[1] This, however, introduces the risk of modifying the crystal structure in the cutting process. The application of transmission electron microscopy (TEM) to the study of these materials is limited since the technique's probing depth is a few hundred nanometers at best.[12] Another commonly applied technique is confocal scanning laser microscopy (CSLM). CSLM is excellent for the in situ investigation of immersed, fluorescent, and refractive-index matched colloidal crystals with particle diameters on the order of a micrometer.[13] However, convectively assembled crystals and their inverted crystals are dry and in contact with air, which implies that the structures and their surroundings are not refractive-index matched. CSLM imaging is then restricted to the first one or two crystal layers, also preventing the study of the crystal internal structure. One way to overcome this is by infiltrating the crystal with a refractive index-matching fluid before imaging the structure[14] but capillary forces acting on the crystal during this process may very well change the structure, resulting in unreliable characterization. In addition, CSLM has the disadvantage that many particle sizes used for colloidal

42

crystals are too small to be imaged, although, for example, the recently developed stimulated emission depletion (STED) microscopes may circumvent this problem. [15] Alternatively, as in chapters 2 and 3, the internal crystal structure may be studied in reciprocal space by small-angle X-ray diffraction (SAXD),[16-18] which is a powerful tool to investigate the crystal structure and planar defects on large length scales, but the local structure important to crystal growth is irresolvable by this technique. This chapter discusses the first study of convectively assembled colloidal crystals by scanning transmission X-ray microscopy (STXM). The technique uses soft X-rays ($E < 2$ keV) that have a smaller penetration depth than hard X-rays ($E > 2$ keV), used in, for example, the recently proposed high resolution transmission X-ray microscopy (HRTXM).[19] However, STXM has the advantage that an even-higher spatial resolution is accessible, richer chemical information can be obtained due to a superior energy resolution, and lighter elements can be studied at their specific X-ray absorption edges, such as the carbon K- and silicon K-edge in the here-presented polystyrene (PS) and silica (SiO_2) colloidal crystals. Compared to coherent X-ray diffraction imaging (CXDI), the characterization of local defect structures is more straightforward in STXM since it is real-space X-ray microscopy. Our results illustrate that STXM offers information on the internal, local structure of such crystals, inaccessible by and complementary to the techniques mentioned above. The chapter is concluded with a detailed comparison of STXM, CSLM, and SEM imaging for the study of photonic and colloidal materials.

4.2 EXPERIMENTAL

Materials

Potassium persulphate (KPS; 99 +%) was obtained from Acros Organics, sodium dodecyl sulphate (SDS; specially pure, >99%) from Brunswig, styrene (for synthesis, >99%) from Merck, and divinylbenzene (technical grade, 55%) and vinyl acetate (>99%) from Aldrich. Millipore water (resistivity: 18 MΩ·cm) was used and 100-nm-thick silicon nitride (Si_3N_4) windows were obtained from Silson Ltd.

Synthesis of Polystyrene and Silica Colloids and Convectively Assembled Colloidal Crystals

Polystyrene seed particles with a cross-linking density of 3 wt% divinylbenzene were synthesized by emulsion polymerization as described by Mock et al.[20] In short, water (400 mL) was heated to 80 °C in a round-bottom flask (1 L). Subsequently, styrene (50 mL) and aqueous SDS solution (100 mL; 5 g L^{-1}) were added, followed by divinylbenzene cross-linker (1.39 mL). The reaction mixture was allowed to equilibrate for 1 h, before adding an aqueous solution of KPS initiator (75 mL; 20.67 g L^{-1}). The reaction was kept at 80 °C for 24 h. The particles were subsequently

coated with vinyl acetate in order to render them more hydrophilic. Therefore, the seed solution (200 mL) was heated to 80 °C for 1 h, after which vinyl acetate (1.70 mL) was added in four aliquots (0.425 mL) with 15-min intervals. Directly after the first addition, aqueous KPS solution (5.05 mL; 0.67 wt%) was added. After the final addition, the reaction was allowed to continue for 24 h. Particles were purified at least three times by centrifugation and subsequent redispersion steps before use. The average colloid diameter was determined to be 194 nm with a polydispersity of 3.7% by TEM measurements on a Philips Tecnai 12 operated at 120 kV. Silica colloids with a diameter of 492 nm and a polydispersity of 3.2% were synthesized according to the Stöber method. These particles were subsequently covered by a layer of 3-methacryloxypropyltrimethoxysilane using a method described by Philipse and Vrij.[21] Colloidal crystals were grown by immersing a clean, 100-nm thick silicon nitride window into a 1% v/v aqueous dispersion of polystyrene colloids or a 0.2% v/v aqueous dispersion of silica colloids and slowly evaporating the solvent in an oven at 50 °C.[1] The absorption by thin silicon nitride windows is negligible, preventing significant attenuation of the X-ray signal by the substrate. SEM pictures of colloidal structures grown on glass slides using this growth procedure are shown in figure 4.1.

STXM Imaging

Investigation of the polystyrene colloidal crystals by STXM was performed at beamline 11.0.2 of the Advanced Light Source synchrotron facility at the Lawrence Berkeley National Laboratory, California, USA.[22] The silica colloidal crystals were studied with the STXM microscope at beamline 10ID-1 (SM) at the Canadian Light Source (CLS), University of Saskatchewan, Canada.[23] A 240-µm-diameter zone plate (ZP) with a central stop of 95 μm and an outermost zone width Δr of 25 nm was used to focus the light with a Rayleigh-criterion spatial resolution $\Delta r_{Rayleigh}$ of 30 nm ($\Delta r_{Rayleigh} \approx 1.22 \cdot \Delta r$). The ZP's central stop and an order-sorting aperture (OSA) were used to select the first-order diffracted X-rays for spectroscopy and imaging. The colloidal crystals on silicon nitride windows were mounted on a piezoelectric sample stage to enable x, y and z translations. As a result, the sample could be focused (Δz) and raster scanned (Δx, Δy). Transmitted light was detected by a scintillator screen combined with a photomultiplier tube (PMT).[24, 25] The setup is shown schematically in figure 4.2a. Typical images were acquired in a point-by-point mode with a 1 ms dwell time per pixel, a 5 µm x 5 µm field of view (FOV), and a 10 nm x 10 nm pixel size. Taking dead time between the acquisition of different pixels into account, the recording of a single transmission image typically took 6 min.
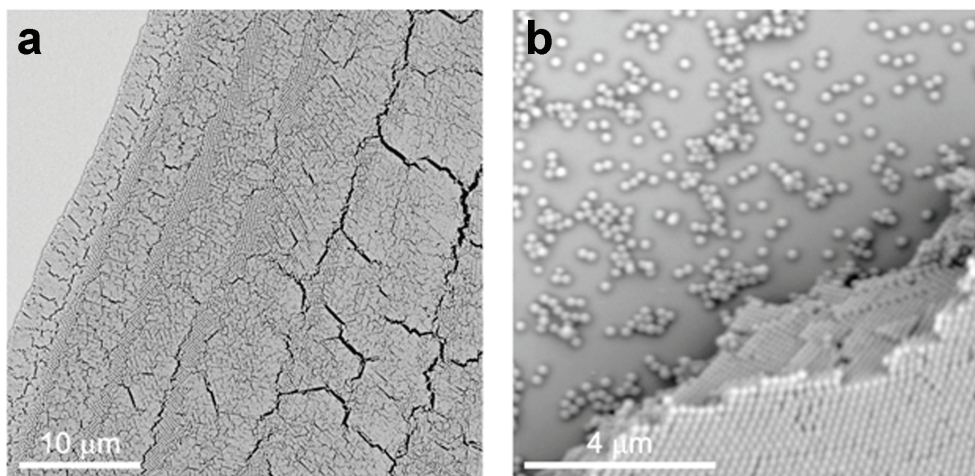
Figure 4.1. SEM micrographs of the polystyrene colloidal crystal that was studied by scanning transmission X-ray microscopy as discussed in this chapter.

4.3   RESULTS & DISCUSSION

SEM images of the crystals of 192 nm polystyrene particles are shown in figure 4.1. The measured periodicity of the lattice was 200 nm, slightly larger than the particle diameter obtained by TEM. From the presence of two differently oriented {111} planes in figure 4.1b, it can be deduced that the dominant crystal structure at those locations is face centered cubic, although some disorder is clearly present. The exact internal crystal structure, however, cannot be deduced from SEM images. [1] The polystyrene and silica colloidal crystals were subsequently studied along their X-ray absorption edges with interferometer controlled STXM.[22, 23, 26] The size of the STXM beam spot is mainly determined by the distance between the two outer gold rings within the zone plate, provided that the rest of the optics, such as the order-sorting aperture and slit sizes are well aligned and set. Here, a zone plate with an outermost zone width, Δr, of 25 nm was used, limiting the Rayleigh-criterion spatial resolution Δr Rayleigh to 30 nm ($\Delta r_{Rayleigh} \approx 1.22 \cdot \Delta r$) for the presented data. The depth of focus, Δz, is given by $\pm 2\Delta r^2/\lambda$ and is thus theoretically ≈ 600 nm at 300 eV and ≈ 3700 nm at 1845 eV, the typical photon energies used here.[24] By measuring X-ray absorption at varying positions and energies, it is possible to acquire an image of a region of interest in which every pixel contains an X-ray absorption spectrum that allows detailed chemical specification (for example the type of element, oxidation state, and coordination number can be deduced).[27, 28] A single-energy X-ray transmission image can, however, contain novel information by itself, as shown in figure 4.2b. Two pictures taken at 315 eV are shown of two different spots in the same polystyrene colloidal crystal. The images
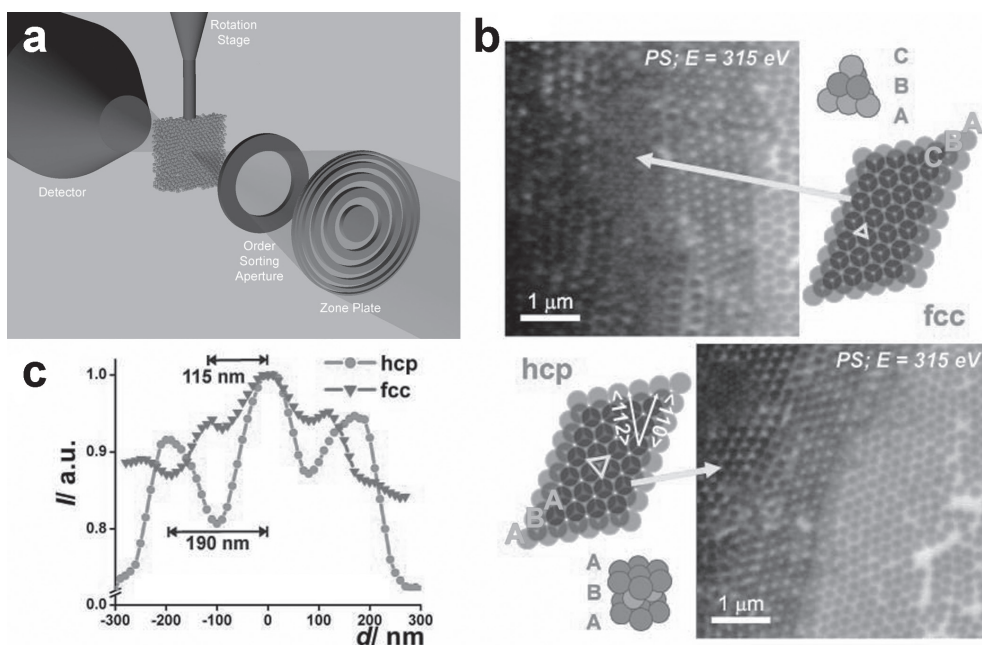
Figure 4.2. (a) Schematic representation of the STXM set-up. Monochromatic X-rays are focused onto the colloidal crystal through a Fresnel zone plate. Unfocused X-rays as well as higher order focal points are filtered out by an order sorting aperture. The transmission of X-rays through the sample is detected with a photomultiplier tube (PMT). (b) Two X-ray transmission images acquired at 315 eV on the carbon K-edge show the presence of one (right side) to three (left side) polystyrene (PS) colloidal layers. The transmission spatial profile is highly different for fcc and hexagonal close packed (hcp) crystal structures, as indicated in the upper and lower panels, respectively. Note that the <110> and <112> directions are indicated in the hcp crystal. (c) Radial intensity distributions of the most X-ray intense points in the three-layered regions of the panels in (b) indicate that the distance, d, between the most transparent regions is 190 nm (circles) and 115 nm (triangles) for the hcp and fcc structures, respectively.

were taken above the carbon K-edge and a large part of the revealed absorption is thus specifically due to the carbon present in polystyrene $((-C_8H_8-)_n)$. A single layer of colloids is clearly resolved on the right side of both images, while multiple colloidal layers were found towards the left of the micrographs. On scanning from right to left, the monolayer changes into a bilayer, which is similar in both images. Further to the left, a third layer revealed an fcc and a hexagonal close-packed (hcp) crystal structure in the two different images. As explained in chapter 1, the fcc and hcp stackings differ in the way the subsequent colloidal layers are positioned on top of each other. A hcp phase has an ABA stacking, in which the third colloidal layer is located directly above the first, while the fcc phase has an ABC stacking, in which the third layer has a different position from both the first and second layers. This yields crystal structures that are completely closed (fcc) and partly open (hcp) in the direction perpendicular to the three colloidal layers, as depicted in the

46

schematic representations in figure 4.2b. The difference between the open and closed structures can be readily observed in the X-ray transmission images, where the open holes in the hcp structure are more transparent than the most transparent, but closed, parts of the fcc structures. Also, the theoretical distance between the most-transparent regions in a hcp structure is equal to the particle diameter σ, while the most-transparent points are $\sigma/\sqrt{3}$ apart in fcc structures. Figure 4.2c shows radial intensity distributions around single X-ray transparent points in the hcp and fcc packed regions of the images. The distributions were obtained using the aXis2000 STXM data processing software[29] and give the average distance from one hole in the colloidal layer to its nearest neighbor hole for hcp (and from one most transparent region to another in fcc). Indeed, it was deduced that the average length between these most transparent regions is 190 and 115 nm in the hcp and fcc structures, respectively, which match the theoretical values of σ = 194 nm in the hcp and $\sigma/\sqrt{3}$ = 112 nm in the fcc structures. Both the differences in absolute intensity in the crystal layers and the distances between the most transparent regions allow for the assignment of the crystal structure being hcp or fcc. Moreover, spatially resolved and quantitative determination of the crystal thickness is possible with STXM if an X-ray transmission image is measured below and on an element-specific X-ray absorption edge. These transmission images can both be converted into optical density (*OD*) maps with $OD = -\ln(I/I_0)$, where I_0 is taken as the intensity of the image background. The difference between the *OD* maps on and below the X-ray absorption edge yields an *OD* map that is element specific and corrected for differences in X-ray attenuation at different energies. This map is subsequently converted into a material-thickness map using $OD=\mu\rho t$, where μ is the photo-absorption cross-section or mass-absorbance coefficient, ρ the material density, and t is the material thickness. Two material thickness maps are displayed in figure 4.3a and 4.3b for the exact same crystal areas that were shown in figure 4.2b. The images used for calculation of the *OD* were taken below and above the carbon K-edge at 278 and 315 eV, since carbon is the principal constituent of polystyrene. Here, the polystyrene density was taken to be 1.05 g cm^{-3}[20] and the mass-absorbance coefficient for polystyrene was estimated to be 36 000 cm^2 g^{-1} using the aXis2000 software that allows for the calculation of μ (calculate X-ray parameters SF package). Figure 4.3c shows the X-ray transmittance at 278 and 315 eV, and the corresponding *OD* as a function of polystyrene thickness, calculated from semi-empirical atomic scattering factors.[30] In the regime of approximately 0.2 < *OD* < 2.1, the material thickness scales linearly with *OD* (or $OD=\mu\rho t$ holds) and the thickness can be quantified in this regime. For polystyrene measured at the carbon K-edge, this means that the material thickness can be quantitatively determined for layers that are 50–550 nm thick. Thickness histograms of the crystals displayed in figure 4.3a and 4.3b are presented in figure 4.3d and clearly show the presence of up to three
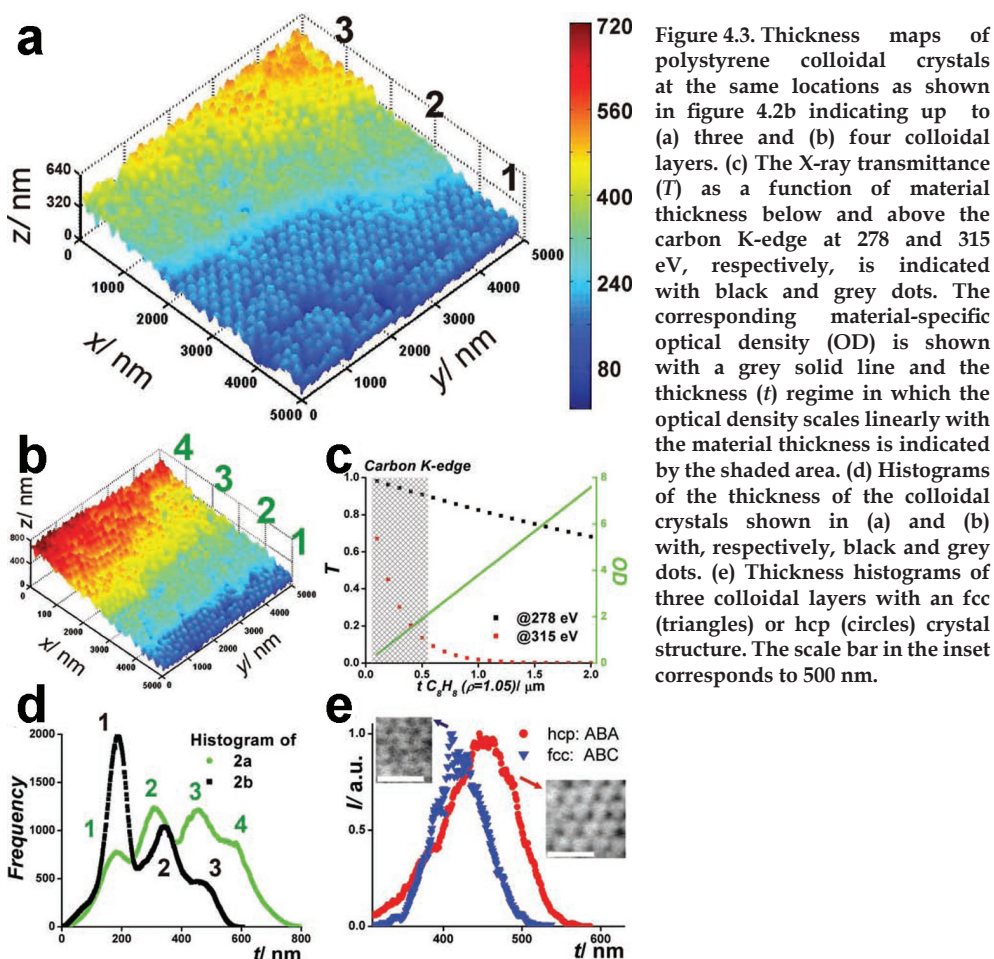
Figure 4.3. Thickness maps of polystyrene colloidal crystals at the same locations as shown in figure 4.2b indicating up to (a) three and (b) four colloidal layers. (c) The X-ray transmittance (*T*) as a function of material thickness below and above the carbon K-edge at 278 and 315 eV, respectively, is indicated with black and grey dots. The corresponding material-specific optical density (OD) is shown with a grey solid line and the thickness (*t*) regime in which the optical density scales linearly with the material thickness is indicated by the shaded area. (d) Histograms of the thickness of the colloidal crystals shown in (a) and (b) with, respectively, black and grey dots. (e) Thickness histograms of three colloidal layers with an fcc (triangles) or hcp (circles) crystal structure. The scale bar in the inset corresponds to 500 nm.

and four colloidal layers, respectively. In addition, when regions of interest were studied that contain only three colloidal layers in a hcp or fcc stacking, the thickness histograms, as given in figure 4.3e, confirm the presence of these phases. The widest distribution of crystal thicknesses was found in the thickness histogram of the hcp structure. It becomes clear that the thickest and thinnest crystal parts are present in the hcp stacking when considering projections in hcp and fcc structures along, for example, <112> and <110> directions, as shown in figure 4.4a and 4.4b, respectively. Note that the fcc coordinate system is used to define crystallographic directions and that the directions are indicated in the insets next to the graphs. Model calculations of the crystal heights for 200 nm diameter spheres along these directions within the two crystal types show the large variation in height within an hcp crystal compared to an fcc structure. Next to theoretical predictions, the experimentally found thickness projections along the <112> and <110> directions
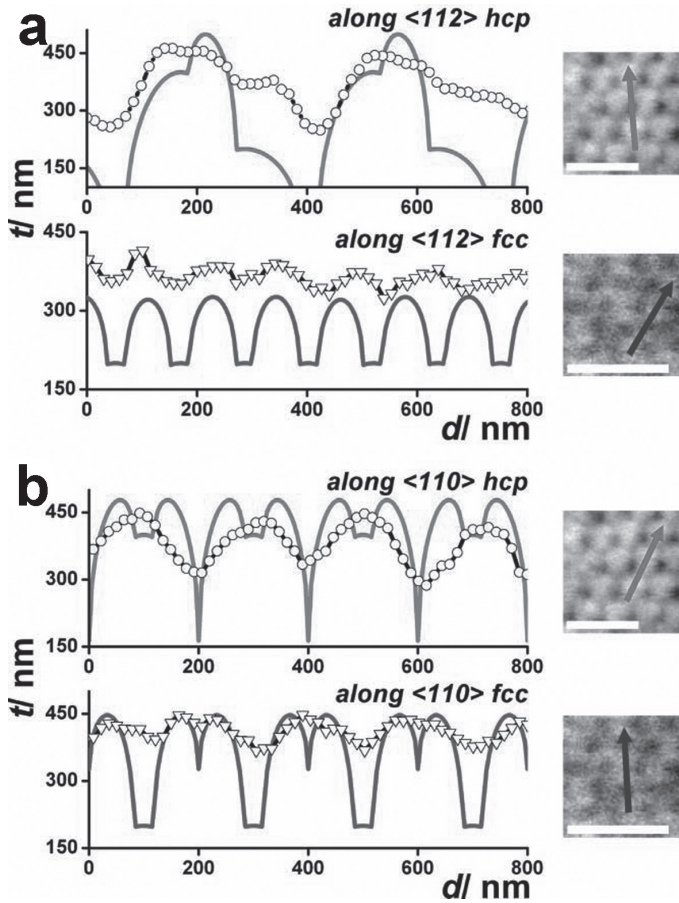
Figure 4.4. (a) Theoretical (solid line) and experimental (symbol and solid line) thickness (*t*) line projections along the <112> direction in hcp (upper panel) and fcc (lower panel) crystal types. **(b)** Identical projections as in (a), but along the <110> direction. Note that STXM-image insets on the right correspond to the indicated crystal type and that the arrows indicate the corresponding crystal directions.

are shown. The experimental projections are averaged over 4 or more line profiles that were taken from images with a short dwell time of 1 ms per pixel. One can appreciate that the general shape and relative intensities of the line profiles match the theoretically predicted profiles. The absolute intensities are in good agreement for the thick parts of the crystal but the thinner parts of the hcp and fcc structures appear too thick, mainly due to the limited lateral resolution. However, in figure 4.3a the determined thickness along the <112> direction in hcp varies stronger than in fcc and even the shape of the experimental hcp <112> projection shows a characteristic structure that roughly matches the theoretical one. Increasing the statistics of such line profiles by taking longer dwell times during image acquisition will significantly improve the quality of such line projections. Nevertheless, it is shown here that STXM has the capacity to discriminate between different directions within a crystal structure from X-ray optical-density images. Figure 4.5a is not a thickness material map but a single transmission image of a large area of a silica
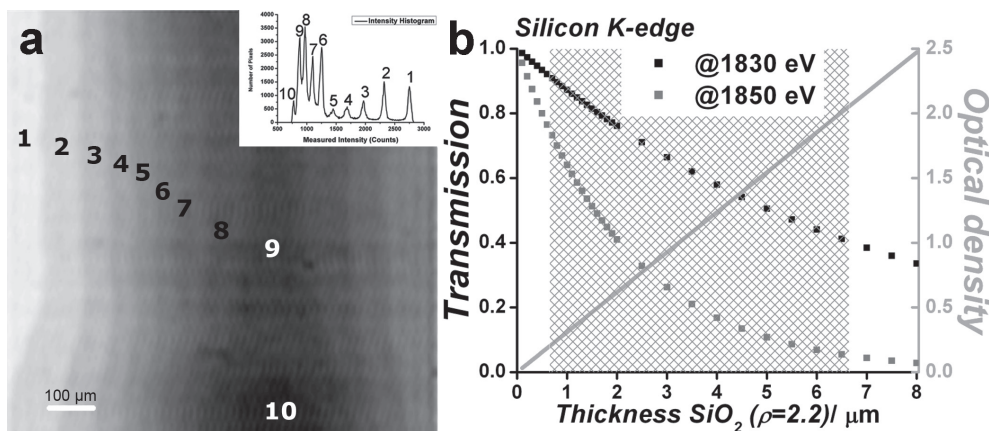
Figure 4.5. (a) Large field-of-view X-ray transmission image acquired at 1845 eV on the silicon K-edge showing the presence of up to 10 colloidal silica (SiO$_2$) layers. The corresponding histogram is shown as an inset. The arrow indicates the direction in which the number of crystal layers on top of each other increases. (b) Black and grey dots indicating the transmittance (T) of X-rays through silica before and on the silicon K-edge, as a function of silica thickness (t). The grey solid line indicates the corresponding optical densities (OD) at those thicknesses and the shaded area shows the regime where the silica thickness can be quantified.

colloidal crystal, taken on the silicon K-edge at 1845 eV. The intensity histogram of figure 4.5a indicates the presence of up to 10 colloidal layers (shown as an inset) and illustrates that STXM is also capable of quantitatively imaging thicker silica-based crystals, where the application of rotation tomography as applied in chapter 5 can reveal the exact location of, for example, crystal defects. Figure 4.5b shows that the thickness of silica-based materials up to 6.5 µm can be quantitatively studied at their silicon K-edge. Figure 4.6a and 4.6b are exemplifications of the chemical sensitivity of STXM. A measured carbon K-edge spectrum of polystyrene is shown in figure 4.6a with an energy resolution of 0.2 eV. By varying the photon energy of the microscope's light over the carbon K-edge, the presence of transitions from C 1s to C=C 1π* and 2π* orbitals was observed at 285 and 288.8 eV, respectively, as well as the transitions to C–H* and C–C σ* unoccupied molecular orbitals, which identifies the measured carbon as being present in polystyrene.[31] The X-ray transmission images acquired at 278 and 315 eV respectively show that the X-ray absorption contrast is specifically due to the presence of carbon. Figure 4.6b shows the silicon K-edge X-ray absorption spectrum of the amorphous silica colloids. The silicon K-edge spectrum reveals the local projected density of empty Si p orbitals (p local density of states)[32] and the main peak at 1845.1 eV corresponds to the Si 3p conduction band. In principle, the discrimination between different chemicals in every pixel, or even voxel, would allow for the study of more complex crystals that are built from more than a single constituent, like, for example, a binary ionic–colloidal crystal.[33] As shown in the presented data, the application of STXM to the
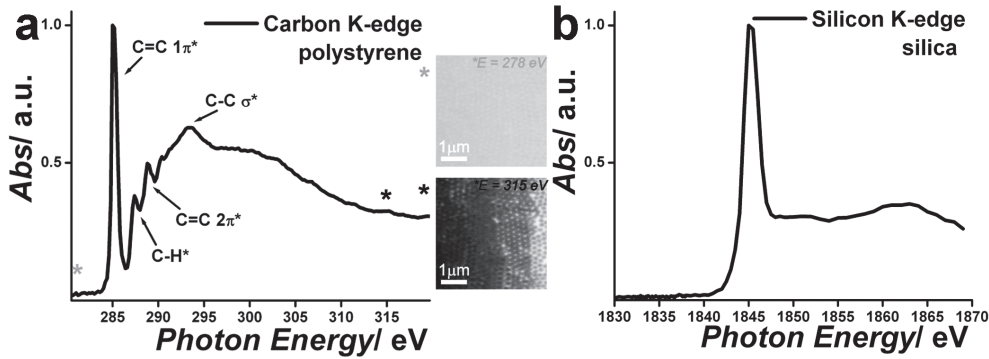
50

Figure 4.6. (a) A carbon K-edge X-ray absorption spectrum of the polystyrene colloids indicating the presence of C 1s to, amongst others, C=C 1π* and 2π* transitions. The STXM images on the right taken at 278 (up) and 315 eV (down) show that the X-ray absorption contrast is specific for the carbon presence. Making use of the carbon K-edge spectral fine structure could give molecular contrast. (b) The silicon K-edge X-ray absorption spectrum of the silica colloids reflects the local projected density of empty Si p orbitals.

characterization of photonic and colloidal crystals can yield novel information on the local crystal structure, especially when combined with tomography, as will be shown in chapter 5. In order to better comprehend why STXM is favorable for this purpose, the technique is compared to CSLM and SEM, which are commonly used for the study of colloidal crystals. A comparison will be made on the basis of three important microscope properties: the lateral Rayleigh-criterion spatial resolution, $\Delta r_{Rayleigh}$, the depth of field, Δz (which is related to the axial spatial resolution), and the penetration depth of the microscope's probe (photons for STXM and CSLM, electrons for SEM).

4.3.1 Comparison of the capabilities of CSLM, STXM, and SEM for colloidal crystal imaging

The discussion is limited to real space microscopy techniques that can provide information on the local crystal structure and thus excludes the reciprocal space techniques, such as SAXD, that generate information on the long range order of crystals.

For CSLM the lateral resolution is diffraction-limited and given by $\Delta r_{Rayleigh} \sim 0.61\lambda / NA$ with λ being the photon wavelength and NA the numerical aperture of the focusing lenses (assuming the condenser and objective lens have equal NA).[34] In order to achieve magnifications that allow for colloidal crystal imaging, lenses with a NA of 0.5 to 1.4 are necessary. The CSLM lateral resolution is better for larger photon energies and higher NA, with a maximal lateral resolution on the order of 10^{-1} µm. For STXM the lateral resolution is given by $\Delta r_{Rayleigh} \sim 1.22*\Delta r$ and the focusing of light occurs through diffraction (and not by refraction as in CSLM).

[24] In this case, the spatial resolution is independent of the incident photon energy and is limited by the distance between the zone plate outer rings Δr. In practice, zone plates with a Δr of 10 to 40 nm are at present readily available and suitable for photonic crystal imaging with a lateral resolution of approximately 10^{-2} μm.[35] In SEM the lateral resolution $\Delta r \sim d$, with d being the diameter of the electron beam spot.[36] Since SEMs are generally operated at 1 to 30 kV, with spot sizes typically ranging from 10 nm for low voltage machines and up to 1 nm for high voltage machines, their lateral resolution is in the 10^{-3} μm range.

The second microscope property discussed here is the depth of field. The depth of field Δz is defined as the distance over which the object plane (with the sample) can be varied while keeping the object in acceptable focus.[36] For CSLM $\Delta z \sim n\lambda/NA^2$ and for STXM $\Delta z \sim \pm 2\Delta r^2/\lambda$.[24] Note that the depth of field decreases with photon energy for CSLM, while it increases with energy for STXM. Nevertheless, the range of accessible depths of field is similar for both techniques and lies in the 10^{-1} to 10^1 μm range. The main difference here is that in confocal microscopy, the depth of field needs to be as small as possible to obtain high resolution in the axial direction and to enable 3D imaging. For STXM, depth of field has to be large, keeping the whole sample in focus, in order to enable tomographic reconstruction. For SEM the depth of field is $\Delta v \sim d/\alpha$, with d being again the electron beam spot diameter and α the convergence half-angle of the electron beam cone.[36] Scanning electron microscopes have nearly parallel electron beams and α therefore varies between 1 and 0.01 mrad, resulting in a very large depth of field of 10^0 to 10^3 μm. The consequence of this large depth of field is that several layers at the exterior of a colloidal crystal can be simultaneously imaged in focus, as depicted in SEM micrographs in figure 4.1. Finally the penetration power of the photons and electrons used in the three techniques is considered. For CSLM and STXM the attenuation length, defined as the distance over which the intensity I falls to $1/e$ of its initial value I_0, is given by Lambert-Beer relations. Standard SEM imaging is done through secondary electron imaging (SEI) in which only electrons with a kinetic energy of <50 eV are used for image formation.[36] This implies that not the electron penetration range (which can be up to 5-10 μm) in the specimen must be considered here, but the electron inelastic mean free path (IMFP) of scattered electrons that generate the SEM images. For CSLM the attenuation length l is given by $l = \log e/(\varepsilon c)$, with c being the molar concentration and ε the molar extinction coefficient. For confocal imaging the polystyrene colloids need to be colored with a fluorescent dye and the total ε is estimated to be 10^1 mol L^{-1} cm^{-1} for the dye-colored polystyrene colloids, while c can be calculated from the polystyrene density $\rho = 1.05$ g cm^{-3} and monomer molecular weight $M_w = 104.11$ g mol^{-1}. The resulting attenuation length is in the 10^1-10^2 μm range for CSLM. For strongly scattering samples, this value strongly decreases and the attenuation length can be as small
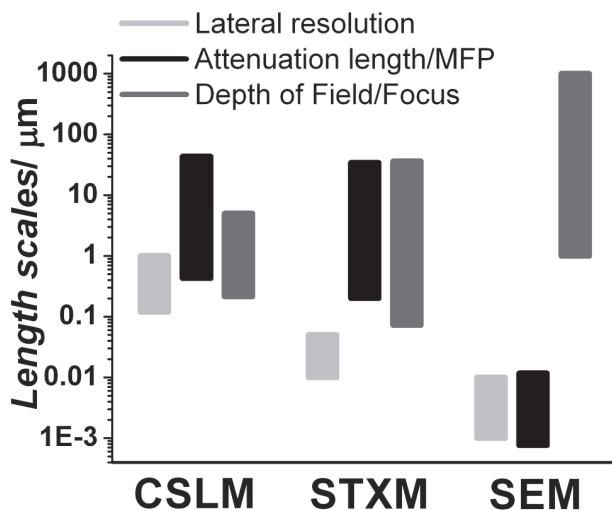
Figure 4.7. Characteristic length scales of three important microscope properties compared for CSLM, STXM, and SEM. The lateral resolution Δr Rayleigh , the depth of focus Δz (in CSLM and STXM) or depth of field Δv (in SEM), and the photon-attenuation length (l in CSLM, t in STXM) or electron mean free path (MFP) in SEM are compared as a function of the photon or electron energy.

as one micrometer. For STXM the attenuation length t is given by $t = 1/\mu\rho$, with μ being the mass absorbance coefficient and ρ the material density. Using the values as given for the maps in figure 4.2b, the attenuation length is in the order of 10^{-1} to 10^{2} µm for STXM. It must be noted here that X-ray attenuation is strongly influenced by the presence of X-ray absorbing edges such as the carbon K-edge in polystyrene around 285 eV. This element specific X-ray absorption is at the same time the basis for the chemical contrast that STXM can provide. In SEM the MFP in nm for organics λ_{org} can be described by an empirical relation

$$\lambda_{org} = \frac{10^3}{\rho}\left(49E^{-2} + 0.11E^{\frac{1}{2}}\right)$$

where E is kinetic energy of the detected electrons in eV.[37] For electrons with an energy <50 eV as detected in SEI-SEM the mean free path is 10^{-3} to 10^{-2} µm, signifying that only the outer few nanometers of the material are being visualized.

The outcomes of this comparison are summarized in figure 4.7. The best obtainable lateral resolution for the techniques are $10^{-1} > 10^{-2} > 10^{-3}$ μm for CSLM, STXM, and SEM, respectively. The depth of focus is very large for SEM ($10^0 – 10^3$ μm) and smaller, but comparable, for CSLM and STXM ($10^{-1} –10^1$ µm). SEM probes a very limited region of $10^{-3} – 10^{-2}$ µm under the material surface, while $10^0 – 10^2$ and $10^{-1} – 10^2$ µm-thick samples are accessible by CSLM and STXM, respectively. It is the unique combination of a large and comparable depth of focus and attenuation length, in combination with an improved spatial resolution compared to CSLM, which is, moreover, independent of the incident photon energy, that makes STXM very useful for the study of colloidal and photonic crystals. Only with STXM it is possible to look through micrometer-thick materials, which are acceptably focused over their full thickness, with a lateral resolution of up to 10 nm. This allows for

the study of crystals built from relatively small building blocks. The fact that STXM does not require luminescent and refractive-index-matched materials, as is necessary for CSLM imaging, is another major advantage of the technique. This allows the internal structures of all colloidal crystals to be probed by STXM: from dry to wet crystals, from refractive-index-matched crystals to non index-matched inverted crystals, and from dye-containing to non-luminescent crystals. The rich chemical characterization that is feasible through the acquisition of X-ray absorption spectra and the quantification of the material thickness are final additional STXM advantages. The following chapter will discuss the use of a rotation stage to enable STXM tomography[38, 39] in which the beneficial, small lateral resolution and large depth of focus are fully exploited. The study of binary colloidal crystals (as, for example, shown with electron tomography for nanocrystals[40]), large-area printed colloidal layers,[41] colloidal gels,[42] and liquid crystals made of anisotropic particles[43] could all benefit from STXM imaging, while the application of in situ STXM microscopy[44-48] to study, for example, more complex colloidal phase behavior is another possibility.

4.4   CONCLUSION

It was shown that STXM can discriminate between fcc and hcp colloidal crystal structures from X-ray transmission images on the basis of relative intensities, the spatial distribution of such intensities, and thickness histograms of the different crystal structures. STXM is also capable of quantitatively determining the colloidal crystal thickness. Line projections within the crystal transmission images allow further for the differentiation of various crystal directions, such as, for example, the fcc <112> and <110> directions. X-ray absorption spectra permit the possibility of combining all of the above with rich chemical contrast for the localization of different crystal building blocks. It is the unique combination of the X-ray depth of focus and attenuation length, which can simultaneously extend to tens of micrometers, in combination with a lateral spatial resolution of up to 10 nm that is independent of the photon energy, that makes STXM highly favorable for the study of the local internal crystal structure over the present benchmark CSLM and SEM techniques. We foresee that STXM can play a major role in the elucidation of problems concerning colloidal and photonic crystal disorder and deformations, which up to now frequently hamper the proper functioning of such materials.

Wang (CLS) are thanked for valuable help with the experiments. Frank de Groot is acknowledged for valuable discussions.

4.5 REFERENCES

[1] P. Jiang, J. F. Bertone, K. S. Hwang, V. L. Colvin, *Chem. Mater.*, **1999**, 11, 2132.

[2] A. Blanco, E. Chomski, S. Grabtchak, M. Ibisate, S. John, S. W. Leonard, C. Lopez, F. Meseguer, H. Miguez, J. P. Mondia, G. A. Ozin, O. Toader, H. M. Van Driel, *Nature,* **2000**, 405, 437.

[3] Y. A. Vlasov, X. Z. Bo, J. C. Sturm, D. J. Norris, *Nature,* **2001**, 414, 289.

[4] D. J. Norris, E. G. Arlinghaus, L. Meng, R. Heiny, L. E. Scriven, *Adv. Mater.*, **2004**, 16, 1393.

[5] E. Yablonovitch, *Sci. Am.,* **2001**, 285, 46.

[6] J. E. G. J. Wijnhoven, W. L. Vos, *Science,* **1998**, 281, 802.

[7] R. Rengarajan, D. Mittleman, C. Rich, V. Colvin, *Phys. Rev. E,* **2005**, 71, 016615.

[8] L. Meng, H. Wei, A. Nagel, B. J. Wiley, L. E. Scriven, N. D. J., *Nano Lett.,* **2006**, 6, 2249.

[9] D. D. Brewer, J. Allen, M. R. Miller, J. M. de Santos, S. Kumar, D. J. Norris, M. Tsapatsis, L. E. Scriven, *Langmuir,* **2008**, 24, 13683.

[10] E. Vekris, V. Kitaev, D. D. Perovic, J. S. Aitchison, G. A. Ozin, *Adv. Mater.,* **2008**, 20, 1110.

[11] J. Hilhorst, J. R. Wolters, A. V. Petukhov, *CrystEngComm,* **2010**, 12, 3820–3826.

[12] F. Wang, H. Zhang, M. Cao, R. Nishi, A. Takaoka, *Micron,* **2010**, 41, 769.

[13] A. Van Blaaderen, P. Wiltzius, *Science,* **1995**, 270, 1177.

[14] H. Wei, L. Meng, Y. Jun, D. J. Norris, *Appl. Phys. Lett.,* **2006**, 89, 241913.

[15] T. A. Klar, S. Jakobs, M. Dyba, A. Egner, S. W. Hell, *P. Natl. Acad. Sci. USA,* **2000**, 97, 8206.

[16] A. V. Petukhov, D. G. A. L. Aarts, I. P. Dolbnya, E. H. A. de Hoog, K. Kassapidou, G. J. Vroege, W. Bras, H. N. W. Lekkerkerker, *Phys. Rev. Lett.,* **2002**, 88, 208301.

[17] J. H. J. Thijssen, A. V. Petukhov, D. C. 't Hart, A. Imhof, C. H. M. Van der Werf, R. E. I. Schropp, A. Van Blaaderen, *Adv. Mater.,* **2006**, 18, 1662.

[18] J. Hilhorst, V. V. Abramova, A. Sinitskii, N. A. Sapoletova, K. S. Napolskii, A. A. Eliseev, D. V. Byelov, N. A. Grigorieva, A. V. Vasilieva, W. G. Bouwman, K. Kvashnina, A. Snigirev, S. V. Grigoriev, A. V. Petukhov, *Langmuir,* **2009**, 25, 10408–10412.

[19] A. Bosak, I. Snigireva, K. S. Napolskii, A. Snigirev, *Adv. Mater.,* **2010**, 22, 3256–3259.

[20] E. B. Mock, H. De Bruyn, B. S. Hawkett, R. G. Gilbert, C. F. Zukoski, Langmuir, **2006**, 22, 4037.

[21] A. P. Philipse, A. Vrij, *J. Colloid Interf. Sci.,* **1989**, 128, 121.

[22] A. L. D. Kilcoyne, T. Tyliszczak, W. F. Steele, S. Fakra, P. Hitchcock, K. Franck, E. Anderson, B. Harteneck, E. G. Rightor, G. E. Mitchell, A. P. Hitchcock, L. Yang, T. Warwick, H. Ade, *J. Synchrotron Radiat.,* **2003**, 10, 125.

[23] K. V. Kaznatcheev, C. Karunakaran, U. D. Lanke, S. G. Urquhart, M. Obst, A. P. Hitchcock, *Nucl. Instrum. Methods,* **2007**, 582, 96.

[24] D. T. Attwood, Soft X-Rays and Extreme Ultraviolet Radiation, 1st Ed., Cambridge University Press, Cambridge, UK**, 2007**.

[25] Y. Vladimirsky, D. P. Kern, T. H. P. Chang, D. T. Attwood, N. Iskander, S. Rothman, K. Mcquaide, J. Kirz, H. Ade, I. Mcnulty, H. Rarback, D. Shu, *Nucl. Instrum. Meth A,* **1988**, 266, 324.

[26] H. Bluhm, K. Andersson, T. Araki, K. Benzerara, G. E. Brown, J. J. Dynes, S. Ghosal, M. K. Gilles, H. C. Hansen, J. C. Hemminger, A. P. Hitchcock, G. Ketteler, A. L. D. Kilcoyne, E. Kneedler, J. R. Lawrence, G. G. Leppard, J. Majzlan, B. S. Mun, S. C. B. Myneni, A. Nilsson, H. Ogasawara, D. F. Ogletree, K. Pecher, M. Salmeron, D. K. Shuh, B. Tonner, T. Tyliszczak, T. Warwick, T. H. Yoon, *J. Electron Spectrosc.,* **2006**, 150, 86.

[27] F. de Groot, *Chem. Rev.,* **2001**, 101, 1779.

[28] F. de Groot, *Coord. Chem. Rev.,* **2005**, 249, 31.

[29] aXis2000 is free for noncommercial use. It is written in Interactive Data Language (IDL) and available online: *http://unicorn.mcmaster.ca/aXis2000.html*

[30] B. L. Henke, E. M. Gullikson, J. C. Davis, *Atom. Data Nucl. Data,* **1993**, 54, 181.

[31] J. Kikuma, B. P. Tonner, *J. Electron Spectrosc.,* **1996**, 82, 53.

[32] M. Taillefumier, D. Cabaret, A. M. Flank, F. Mauri, *Phys. Rev. B,* **2002**, 66, 195107.

[33] M. E. Leunissen, C. G. Christova, A. P. Hynninen, C. P. Royall, A. I. Campbell, A. Imhof, M. Dijkstra, R. van Roij, A. van Blaaderen, *Nature,* **2005**, 437, 235.

[34] R. H. Webb, *Rep. Prog. Phys.,* **1996**, 59, 427.

[35] W. L. Chao, B. D. Harteneck, J. A. Liddle, E. H. Anderson, D. T. Attwood, *Nature,* **2005**, 435, 1210.

[36] R. F. Egerton, Physical Principles of electron Microscopy, 3rd Ed., Springer, New York**, 2008**.

[37] M. P. Seah, W. A. Dench, *Surf. Interface Anal.,* **1979**, 1, 2.

[38] A. P. Hitchcock, J. Li, S. R. Reijerkerk, P. Foley, H. D. H. Stover, I. Shirley, *J. Electron Spectrosc.,* **2007**, 156, 467.

[39] G. A. Johansson, T. Tyliszczak, G. E. Mitchell, M. Keefe, A. P. Hitchcock, *J. Synchrotron Radiat.,* **2007**, 14, 395.

[40] H. Friedrich, C. J. Gommes, K. Overgaag, J. D. Meeldijk, W. H. Evers, B. de Nijs, M. P. Boneschanscher, P. E. de Jongh, A. J. Verkleij, K. P. de Jong, A. van Blaaderen, D. Vanmaekelbergh, *Nano Lett.,* **2009**, 9, 2719.

[41] S. Jeong, L. B. Hu, H. R. Lee, E. Garnett, J. W. Choi, Y. Cui, *Nano Lett.,* **2010**, 10, 2989.

[42] M. M. van Schooneveld, V. W. A. de Villeneuve, R. P. A. Dullens, D. G. A. L. Aarts, M. E. Leunissen, W. K. Kegel, *J. Phys. Chem. B,* **2009**, 113, 4560.

[43] M. C. D. Mourad, E. J. Devid, M. M. Van Schooneveld, C. Vonk, H. N. W. Lekkerkerker, *J. Phys. Chem. B,* **2008**, 112, 10142.

[44] J. F. Creemer, S. Helveg, G. H. Hoveling, S. Ullmann, A. M. Molenbroek, P. M. Sarro, H. W. Zandbergen, *Ultramicroscopy,* **2008**, 108, 993.

[45] E. de Smit, I. Swart, J. F. Creemer, G. H. Hoveling, M. K. Gilles, T. Tyliszczak, P. J. Kooyman, H. W. Zandbergen, C. Morin, B. M. Weckhuysen, F. M. F. de Groot, *Nature,* **2008**, 456, 222.

[46] E. de Smit, I. Swart, J. F. Creemer, C. Karunakaran, D. Bertwistle, H. W. Zandbergen, F. M. F. de Groot, B. M. Weckhuysen, *Angew. Chemie. Int. Edit.,* **2009**, 48, 3632.

[47] B. M. Weckhuysen, *Angew. Chemie. Int. Edit.,* **2009**, 48, 4910.

[48] F. M. F. de Groot, E. de Smit, M. M. van Schooneveld, L. R. Aramburo, B. M. Weckhuysen, *Chemphyschem,* **2010**, 11, 951.

Three Dimensional Structure and Defects in Colloidal Photonic Crystals Studied with Tomographic Scanning Transmission X-ray Microscopy

Self-assembled colloidal crystals have attracted major attention due to their potential as low-cost 3D photonic crystals. Although a high degree of perfection is crucial for the properties of these materials, little is known about their exact structure and internal defects. In this study, tomographic scanning transmission X-ray microscopy (STXM) is used to access the internal structure of self-assembled colloidal photonic crystals with high spatial resolution for the first time. The positions of individual particles of 236 nm in diameter are identified in three dimensions and the local crystal structure is revealed. Through image analysis, structural defects such as vacancies and stacking faults are identified. Tomographic STXM is shown to be an attractive and complementary imaging tool for photonic materials and other strongly absorbing or scattering materials that cannot be characterized by electron microscopy or optical nanoscopy.

Chapter 5: Tomographic STXM

5.1 INTRODUCTION

Photonic crystals are currently under research for their capability to manipulate the propagation of light which opens the way to the perfecting of existing technology like optical fibers[1, 2] or lasers,[3] but also to exotic new devices such as optical chips.[4]

Self-assembly of the right building blocks into large photonic crystals is one of the most promising pathways in terms of speed and production cost.[5, 6] Drawbacks of this technique lie in the intrinsic disorder present in such systems[7-10] and the difficulty of including functional defects at desired positions.[11] The most promising growth process in this category is convective assembly.[6, 12] This method produces good quality crystals with a mainly face centered cubic (fcc) structure,[9, 12] which is required for producing materials with a full photonic band gap in the visible.

Despite the large interest in these structures, much is still unknown about the processes governing self-assembly, driving the crystal into its fcc structure. Most of what is known about the crystal structure is obtained either through surface methods such as scanning electron microscopy (SEM)[7, 12] or through bulk averaging methods, such as microradian X-ray diffraction[9, 13, 14] or field-stop filtered microscopy.[15] These techniques only provide information about the crystal surface structure or about stacking sequences over large areas of crystal, but neglect the local defect structure, which is so important for the optical properties[16] and for the growth process.[10, 17]

Recent developments in X-ray imaging have yielded a spectrum of techniques with the potential to access the internal structure of colloidal photonic crystals. Among these are coherent diffraction imaging (CXDI)[18], ptychography,[19] and high resolution transmission hard X-ray microscopy (HRTXM).[20] The relatively high penetration power of X-rays enables studies of almost any material and thickness. In CXDI and ptychography use is made of phase retrieval algorithms to reconstruct a real-space representation from diffraction patterns. The merits of ptychography were demonstrated in a tomographic reconstruction of a bone sample[21] with a voxel size as small as 65 nm in all three dimensions. Full-field HRTXM imaging of colloidal crystals was recently demonstrated at 12 keV photon energy,[20] resulting in a large penetration depth of the probing beam and with a spatial resolution of ~100 nm. At such high energies, however, phase contrast is much larger than absorption contrast if the photon energy is not tuned to a specimen absorption edge. For this reason, interpretation of resulting data remains challenging.

In the previous chapter it was shown that much information about the local crystal structure can be obtained with a resolution as good as 30 nm by STXM imaging.[22] The major benefit of this technique is the possibility to obtain element specific absorption contrast, significantly simplifying data analysis. A detailed
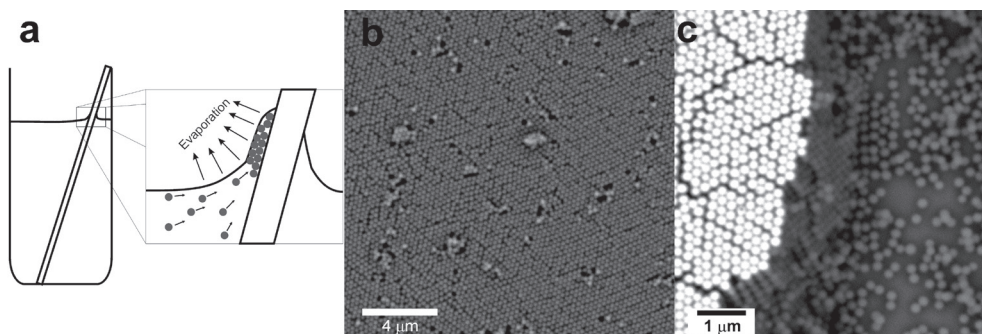
Figure 5.1. (a) A schematic representation of crystal growth by convective assembly is shown. Evaporation of solvent at the curved meniscus and the crystal surface creates a flow of particles towards the growing crystal. (b-c) Representative SEM images of the crystals obtained on glass substrates.

comparison between optical microscopy methods,[17, 22-25] SEM, and STXM was also given in the previous chapter.[22]

Here, the use of STXM is extended to include tomographic reconstruction, enabling studies of the internal three dimensional crystal structure of thick (>5 layers) crystals, including defects, for the first time. The crystals, grown from silica particles of 236 nm in diameter, were measured at and before their silicon K-edge, at 1845 and 1830 eV respectively, to obtain pure material absorption contrast and therefore information on sample thickness.[22]

5.2   EXPERIMENTAL

Silica particles were synthesized according to the method described by Stöber *et al.*[26] A coating of 3-(trimethoxysilyl)propyl methacrylate (TPM) was added following the method of Philipse and Vrij.[27] Particle diameter was determined using transmission electron microscopy (TEM) and was found to be 236 nm with a relative standard deviation of 5%. This size was verified for particles in solution using dynamic light scattering.

Crystals were grown onto various types of substrates by immersing the substrate into an aqueous dispersion with particle concentrations ranging from 0.1 to 1.0 % v/v and evaporating the solvent[12] (Millipore water, 18 MΩ·cm). A schematic of the growth process is shown in figure 5.1a. Si_3N_4 windows of 100 nm thickness (Silson Ltd.) as well as cut TEM grids coated with a 2-3 nm thick layer of platinum or palladium (Ted Pella, Substratek) were used as substrates. These were attached to a glass slide and added to a crystal growth dispersion. The reason for growing crystals on such thin substrates is the limited penetration depth of soft X-rays. At the energies used here, 1830-1845 eV, this can be up to several micrometers. As the substrate should not attenuate the beam too much, it should at most be 1 μm thick. Typical SEM images of crystals grown on thicker glass slides are displayed

in figures 5.1b and 5.1c.

STXM measurements were performed at the 10ID-1 soft X-ray spectromicroscopy beamline at the Canadian Light Source (CLS) in Saskatoon, Canada.[28] A schematic of the setup is displayed in figure 5.3a and the technical details of the technique are discussed in detail in chapter 4. In short, monochromatic X-rays with an energy between 130 and 2500 eV are focused onto a spot on the sample by a Fresnel zone plate. For the silica particles described in this chapter, measurements were performed at photon energies of 1845 and 1830 eV, *i.e.* above the silicon K-edge and in the pre-edge. Measured transmission is converted to optical density through the Lambert-Beer law. Background images recorded at 1830 eV are subtracted from the 1845 eV edge images, obtaining pure silicon absorption contrast. The lower size limit of the beam spot is determined by the quality of the zone plate, the outermost zone-width and the X-ray energy. In the experiment described here, the instrument spatial resolution was 30 nm. Higher order focal points of the zone plate and zero order light are filtered out by the order sorting aperture (OSA) and a central stop on the zone plate. Due to the relatively long focal length of the zone plate at the energies used in this experiment, the depth of focus of the beam (~3700 nm) was of the same order of magnitude as the whole thickness of the sample, ensuring optimum resolution in the whole of the crystal.[22] Finally, a detector consisting of a scintillator and a photomultiplier tube detects the transmitted X-ray intensity. A piezoelectric sample stage is used to scan the sample along the plane normal and parallel to the beam, gathering a focused transmission image of the desired region in the sample.

Prior to tomographic reconstruction, all images were processed using the aXis2000 software package[29]. For all images measured above the silicon K-edge a pre-edge image measured at an energy just below the onset of the edge was subtracted to obtain pure silicon absorption contrast. Tomographic reconstruction was performed with the IMOD tomography package.[30]

5.3   THEORY

Tomography is the science of imaging objects in slices (tomos means "slice" or "part" in ancient Greek). This may refer to physical sectioning, by cutting an object in thin slices and imaging them, but nowadays non-destructive methods are more widespread, largely due to medical tomographic methods such as magnetic resonance imaging (MRI) or X-ray computed tomography (CT). The method presented in this chapter strongly resembles the CT-technique and may be referred to as nano-CT.

This technique is based on imaging of samples with a focal length that exceeds the sample thickness. This way, the whole sample is in focus during image acquisition
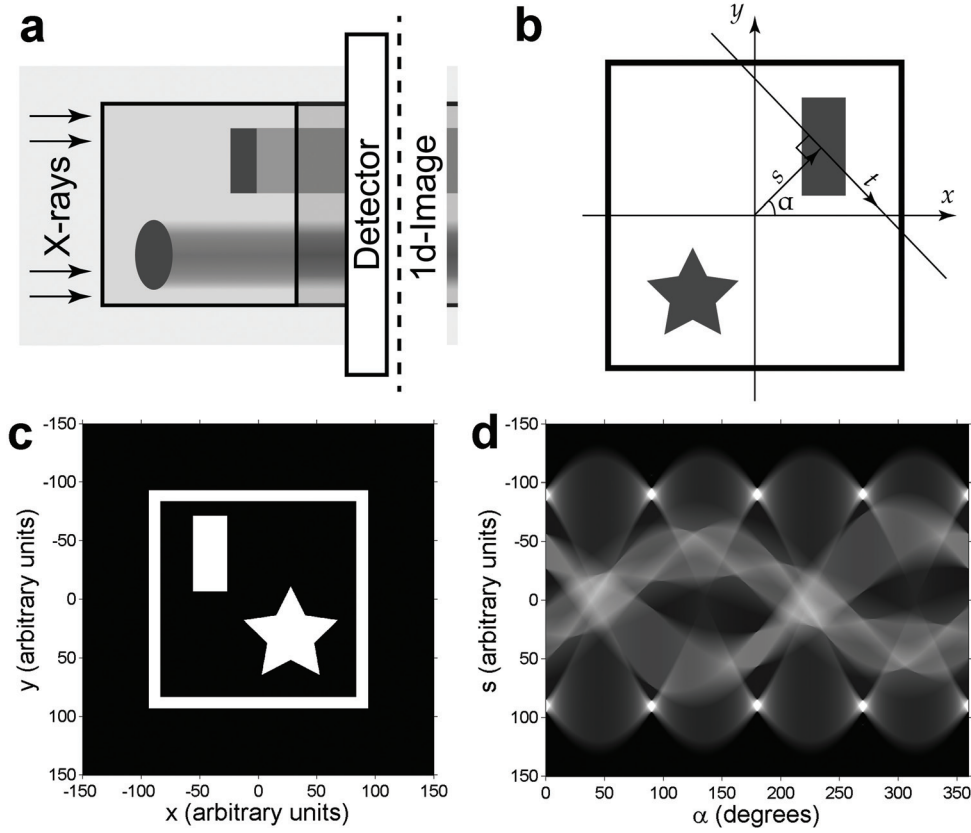
Figure 5.2. (a) In a 1D projection of a 2D sample, all structural information along the beam direction is lost. (b) The Radon transform transforms an intensity *I(x, y)* to an intensity *I(α, s)* by integrating along *t*. (c) An image of a star and a bar in a box and (d) its Radon transform.

and all parts of the sample along the optical axis contribute equally to the signal. A single image therefore provides information on the distribution of material in the image plane, but all information along the optical axis is averaged and any structural information in this direction is lost (figure 5.2a). By rotating the sample and taking another image, information can be obtained about the distribution of material in the direction that was previously the optical axis.

A perfect reconstruction of the internal structure of any sample would be possible if the measured dataset would contain a full Radon transform (*Rf*) of the sample, *i.e.* a dataset consisting of an infinite number of images collected from an equal amount of angles. In two dimensional space, this looks as follows:

$$Rf\left(\alpha,s\right) = \int_{-\infty}^{\infty} f\left(x(t),y(t)\right)dt$$

$$= \int_{-\infty}^{\infty} f\left(\left(t\sin\alpha + s\cos\alpha\right),\left(-t\cos\alpha + s\sin\alpha\right)\right)dt$$

(5.1)

where $f(x, y)$ is the material distribution in the x, y plane. The integral gives the total amount of material (or total signal extinction) along a line $L(\alpha, s)$, with α the angle between the line normal and the x-axis and s the distance between the line and the origin, as shown schematically in figure 5.2b. At a single value of α, a plot of Rf versus s would result in the 2D analogue of a transmission image. The full Radon transform is sometimes called a sinogram, as each point $f(x, y)$ in the sample produces a sine profile in the Radon transform. Figures 5.2c and 5.2d show a simple image of a star and a rectangle in a 2D box and its Radon transform.

In reality, a recorded tomogram (a "measured" Radon transform of a sample) consists of a finite number of angular projections, which drastically reduces the quality of the inverse transform. Moreover, physical constraints to sample rotation often limit the range of measured angles. This should ideally be 180 degrees, but transmission limitations or sample geometry usually limit this to 140 degrees or less, strongly reducing reconstruction resolution in the direction perpendicular to the missing measurement directions.

The reconstruction method employed here uses the fact that the Fourier transform of each 2D projection of the sample corresponds to a slice through the 3D Fourier image of the complete sample, as discussed for example by Friedrich et al.[31] By taking the Fourier transform of each recorded image and putting the resulting data together, the full 3D reciprocal space can be reconstructed. The inverse Fourier transform of the 3D dataset subsequently provides the 3D real-space image of the sample.

5.4   RESULTS & DISCUSSION

An example of a STXM image of a crystal consisting of 492 nm particles on a silicon nitride window is given in figure 5.3b. From left to right, sharp, stepwise changes in intensity indicate transitions towards a thicker crystal. A histogram of the measured intensity distribution is shown in the inset. Every peak corresponds to a certain thickness of crystal, with the highest measured intensity (right) corresponding to the thinnest piece of crystal. This way, up to 10 layers of material can be identified, as expressed by the numbers in the histogram. The corresponding numbers have been added to the OD image as well.

Overviews like figure 5.3b are suitable for selecting regions of interest (ROI) in a sample, or for investigating the transmission as function of material thickness. To be able to reconstruct crystal structures on a single particle level, however, more detailed images have to be obtained. Figures 5.3c-g show such images, with a field of view of 5x5 μm^2 and a pixel size of 25x25 nm^2. Particles in the images are 236 nm in diameter. By measuring such an ROI at different angles with respect to the beam, a rotation series is obtained through which the three dimensional crystal structure
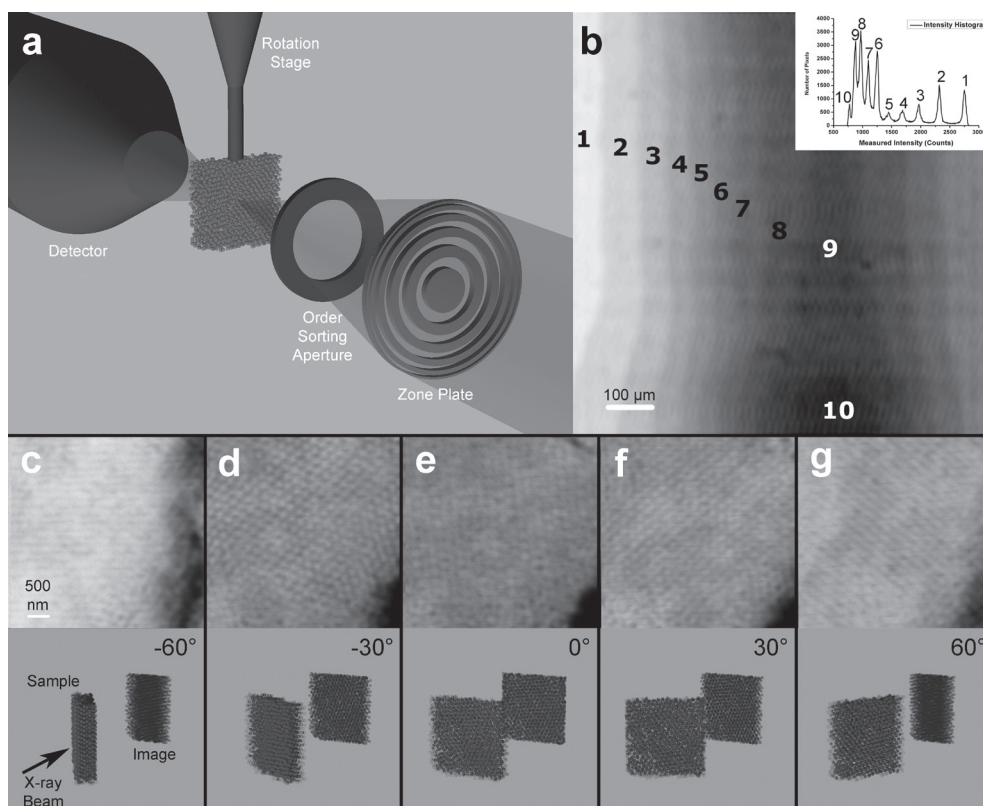
Figure 5.3. (a) A schematic representation of the microscopy setup as described in the main text. (b) A 1.0x1.0 mm^2 STXM overview of a crystal that is up to 10 layers thick. Different intensities represent different thicknesses and thickness increases from left to right. Individual particles cannot be distinguished at this magnification. The inset shows an intensity histogram, identifying up to 10 particle layers. Panels (c-g) contain optical density images obtained from STXM measurements on a real crystal. The angles at which the scans were made are given below each image, along with a schematic indicating the effect of measurement angle on transmission and width of the region of interest.

can be reconstructed. To allow for sample rotation at short working distances between the focusing optics and the detector, samples were prepared in a way similar to the method described by Obst *et al.*[32] In short, Pd and Pt coated TEM grids were cut on two sides to leave a small ribbon of material approximately 1 mm wide onto which the crystal was grown. This ribbon was glued to the rotation stage described by Johansson *et al.*[33] Suitable regions for tomogram recording were selected on the basis of three criteria. Firstly, sample thickness had to be large enough to obtain relevant information about the internal crystal structure, but small enough to avoid signal saturation at high scanning angles. Secondly, regions close to the edge of a grid square had to be avoided as the grid edges would interfere
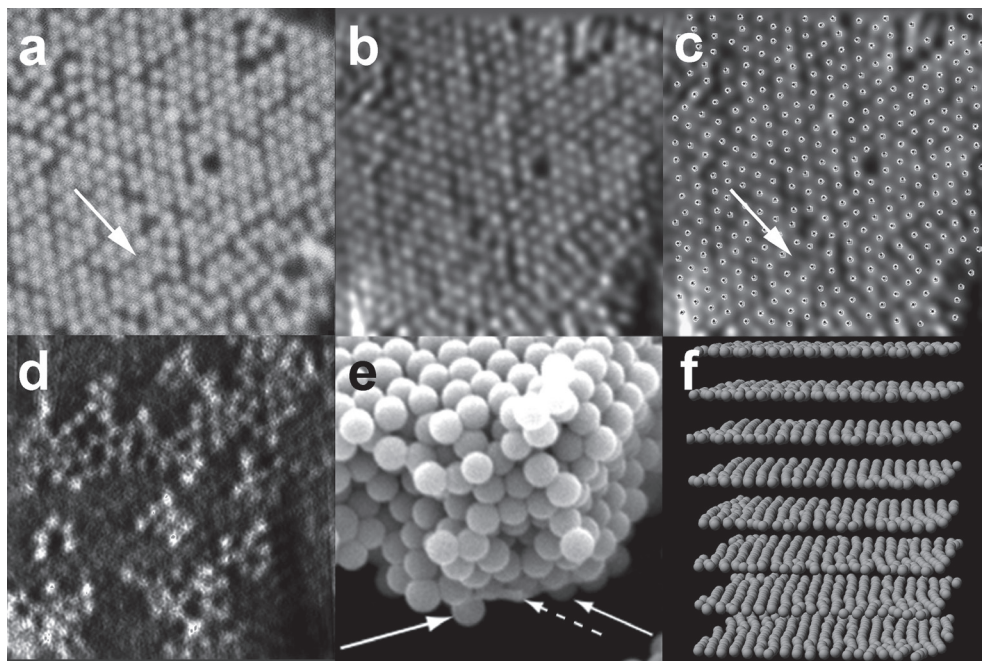
Figure 5.4. (a-c) The top layer of the crystal in SEM view, a tomographic STXM reconstruction and the detected particle positions, are shown respectively. Arrows indicate the only particle that was not identified by the detection algorithm. (d) Disordered layer at the bottom of the crystal. (e) SEM image showing that the disordered layer lies on the bottom side of the substrate. The substrate is indicated by the dashed arrow. (f) A model view showing all detected particles in the 8 layers of the reconstruction. The z-axis has been stretched for clarity.

with imaging upon rotation. Finally, to ensure proper sample positioning after every rotation step a region had to contain a prominent feature, such as a crystal crack. Pictures were taken over a range of -60° to 60° with steps of 4°. Every third step, an extra angle was recorded after a 2° interval.

Figure 5.3c-g show the region used for tomographic reconstruction recorded from 5 different angles. Below each image, a schematic representation of the sample and its image is provided for clarity. In the bottom right corner of each image, the crack that has been used as a reference for sample positioning can be seen. The projections have been converted from transmission to optical density (OD) images. From a calibration image, a single layer was found to have a maximum OD of approximately 0.25. Considering a packing fraction of 74% for close packed spheres, the average OD of 1.5 measured at normal incidence corresponds to approximately 8 layers of particles.[22] Intensity modulations corresponding to periodicities in the crystal lattice could be observed in almost all projections and are attributed to alignment of particles along specific crystallographic directions. In total, 41 projections were used for tomographic reconstruction.

5.4.1   Tomographic Reconstruction

Results of the tomographic reconstruction are displayed in figure 5.4. Figure 5.4a contains an SEM image of the region of interest; figure 5.4b depicts the same layer obtained by reconstruction of the STXM tomography dataset. From these images the perfect agreement between direct imaging and tomographic reconstruction is apparent. Only a slight discrepancy can be observed at the top edge and the bottom left corner of the reconstruction. These artifacts are attributed to misalignments during acquisition, resulting in the absence of these specific regions in some of the images. In total, the reconstruction produced a crystal of 8 layers thick, in good agreement with the value calculated from the average optical density. In addition, a disordered, open layer was also found at the bottom of the crystal (figure 5.4d). This layer consists of particles deposited on the back side of the TEM grid during crystal growth, as confirmed by the SEM image in figure 5.4e.

From the final reconstruction, particles and their positions were detected and digitized using an algorithm similar to the one described by Crocker and Grier,[34] written for IDL (Interactive Data Language). As can be seen in figure 5.4c, the algorithm accurately detects the center of virtually every particle. Only one particle that is present in the SEM image has been missed, as indicated by the arrows in figure 5.4a and 5.4c. Also in the region close to the crack some discrepancies can be noted. Here particles may have been slightly above or below the tomographic slice or excluded from some projection angles due to misalignments. Nonetheless, as over 300 particles were identified in the first layer, the detection was approximately 99% accurate. A 3D rendering of the particles from all 8 layers of the reconstruction is shown in figure 5.4d. The disordered layer on the back of the grid has been left out for clarity.

5.4.2   Defect Characterization

Using the detected particle coordinates, the crystalline environment of every individual particle could be determined. To be able to detect the stacking of individual particles, an algorithm was used that correlates the positions of the nearest neighbors in the layer above and below each particle to each other.[8] In hcp stacking these have the same orientation (ABA stacking of hexagonal layers), while in fcc the triangles they form in both layers are rotated by 60° with respect to each other (ABC stacking). Figure 5.5a shows that the measured structure is dominated by fcc stacking, as expected for a convectively assembled colloidal crystal.[12] However, the hcp stacking found in the fifth layer causes twinning from ABC to CBA structure in the middle of the crystal, which is unfavorable for the photonic band structure.[16]

Apart from stacking disorder, we observe other local defects, such as vacancies. These can be observed in images of the first and fifth crystal layers displayed
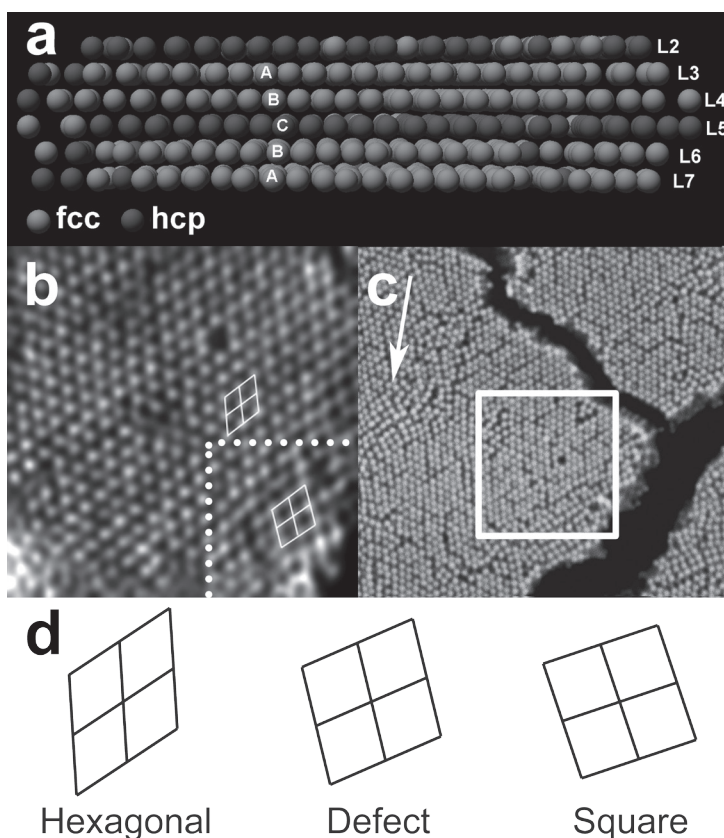
Figure 5.5. (a) A side view of the stacking sequence of layers 2 (top) to 7 (bottom) of the tomographic reconstruction is shown. Layers 1 and 8 are excluded as these have neither fcc nor hcp configuration. Both layers 2 and 5 are in hcp configuration. Panel (b) shows a reconstruction of the fifth layer of the crystal, including the deformed region in the bottom right, which is contained in the dotted square. From the white overlaid lines, it is clear that this region is between square and hexagonal orientation, as illustrated in (d). Panel (c) displays a deformed region of crystal outside of the tomographic region of interest (highlighted by the white square) is indicated by the arrow.

in figure 5.4b and 5.5b respectively. The top right corner in figure 5.4b shows a triangle of line defects as discussed by Meijer et al.[8] This structure can be formed when a group of three vacancies aligns and three neighboring particles move from an A to a B position on the hexagonal plane below. It has been shown recently[10] that defects like this may have a significant influence on the final crystal structure. However, we did not find similar defects in the inner structure of the studied crystal. The occurrence in the top layer may therefore be a surface effect and further study is required to conclusively establish whether or not these defects occur more frequently.

The bottom right corner in figure 5.4a and 5.4b shows a region of particles in square and rectangular configurations. These look similar to the transition regions that have been discussed by Meng et al.[17] as possible candidates for causing the strong preference for fcc growth, albeit for thin crystals. The occurrence of these regions here could point to a similar mechanism for thicker crystals, but conflicts with our observation of a stacking fault in the middle of the crystal. In an SEM overview image (figure 5.5c), the region can be seen to extend over a longer

range and a similar structure runs parallel to it indicating an additional possible thickness transition. As mentioned earlier, however, SEM cannot provide us with any information on the deeper, internal crystal structure. In the tomographic reconstruction, the transition region could be imaged in all crystal layers. In figure 5.5b the fifth layer of the crystal is displayed. The bottom right region in this picture, contained in the dotted box, lies at the same position as the deformed region in figure 5.4a and 5.4b. It does not have square coordination such as the first layer, but is not perfectly hexagonal either, as indicated by the drawn white lines connecting the particles and illustrated in figure 5.5d. Although the structures found in the layers in between do not resemble those found by Meng *et al.*,[17] they are different from the rest of the crystal. For layers beyond the fifth layer, the corner returns to a perfect hexagonal orientation in line with the rest of the crystal. From this, it can be concluded that the deformed regions observed in the top layer with SEM extend several layers into the crystal, but with a finite depth. It is therefore suspected that if these regions do influence the structure as in ref.[17] they only influence the top layers. In this light, it is remarkable that we find a twinning plane at exactly the depth where the influence of the deformed region ends. The limited size of the deformed region in this reconstruction, however, does not allow us to draw further solid conclusions about the growth mechanism. Nonetheless, the detail with which tomographic STXM yields information on the internal structure of convectively assembled crystals is highly promising for further investigations focusing on specific sites or defects in these materials.

5.4.3 Future Experiments

For further experiments, the start-up of new transmission X-ray microscopes with photon energies up to 14 keV promises microscopy with absorption contrast on virtually any element. With this, the imaging of thick inverted crystal structures (crystals of air spheres in high refractive index materials) consisting of heavier elements such as titanium,[35] iron, nickel[36] or even cadmium[37] becomes feasible. Also, the availability of both soft and hard X-ray microscopes might be used for the real-space study of colloidal liquid crystals[38]. In cases where no chemical or elemental contrast is required, the possibility of working with a wide energy range at full-field transmission X-ray microscopes (TXM) also drastically reduces acquisition times, thereby strongly increasing the sample throughput. Furthermore, combinations of STXM with coherent diffraction imaging[39] show promise of pushing the resolution into the sub-10 nm regime.

5.5   CONCLUSIONS

In summary, we have shown the applicability of absorption contrast soft X-ray tomography for the 3D imaging of crystals of inorganic colloids on a single particle level. In a volume of 5x5x2 μm^3 the positions and crystal structure of individual 236 nm particles were determined. Several types of crystal defects were identified, warranting further study into their role in the crystal growth process. Newly commissioning microscopes show promise of faster recording of high quality data on virtually any material with element specific absorption contrast. With these improvements in mind, we see X-ray tomography as a valuable addition to the characterization toolbox for photonic crystals in specific or condensed matter physics in general.

5.6   REFERENCES

[1] P. Russell, *Science,* **2003**, 299, 358.

[2] J. C. Knight, *Nature,* **2003**, 424, 847.

[3] O. Painter, R. K. Lee, A. Scherer, A. Yariv, J. D. O'Brien, P. D. Dapkus, I. Kim, *Science,* **1999**, 284, 1819.

[4] M. Soljacic, C. Luo, J. D. Joannopoulos, S. Fan, *Opt. Lett.,* **2003**, 28, 637.

[5] A. Blanco, E. Chomski, S. Grabtchak, M. Ibisate, S. John, S. W. Leonard, C. Lopez, F. Meseguer, H. Miguez, J. P. Mondia, G. A. Ozin, O. Toader, H. M. Van Driel, *Nature,* **2000**, 405, 437.

[6] Y. A. Vlasov, X. Z. Bo, J. C. Sturm, D. J. Norris, *Nature,* **2001**, 414, 289.

[7] Y. A. Vlasov, V. N. Astratov, A. V. Baryshev, A. A. Kaplyanskii, O. Z. Karimov, M. F. Limonov, *Phys. Rev. E,* **2000**, 61, 5784.

[8] J. M. Meijer, V. W. A. De Villeneuve, A. V. Petukhov, *Langmuir,* **2007**, 23, 3554.

[9] J. Hilhorst, V. V. Abramova, A. Sinitskii, N. A. Sapoletova, K. S. Napolskii, A. A. Eliseev, D. V. Byelov, N. A. Grigorieva, A. V. Vasilieva, W. G. Bouwman, K. Kvashnina, A. Snigirev, S. V. Grigoriev, A. V. Petukhov, *Langmuir,* **2009**, 25, 10408–10412.

[10] J. Hilhorst, J. R. Wolters, A. V. Petukhov, *CrystEngComm,* **2010**, 12, 3820–3826.

[11] T. A. Taton, D. J. Norris, *Nature,* **2002**, 416, 685.

[12] P. Jiang, J. F. Bertone, K. S. Hwang, V. L. Colvin, *Chem. Mater.,* **1999**, 11, 2132.

[13] W. L. Vos, M. Megens, C. M. Van Kats, P. Bosecke, *Langmuir,* **1997**, 13, 6004.

[14] J. H. J. Thijssen, A. V. Petukhov, D. C. 't Hart, A. Imhof, C. H. M. Van der Werf, R. E. I. Schropp, A. Van Blaaderen, *Adv. Mater.,* **2006**, 18, 1662.

[15] H. J. Schöpe, A. Barreira Fontecha, H. Konig, J. Marques Hueso, R. Biehl, *Langmuir,* **2006**, 22, 1828.

[16] Z. L. Wang, C. T. Chan, W. Y. Zhang, Z. Chen, N. B. Ming, P. Sheng, *Phys. Rev. E,* **2003**, 67, 016612.

[17] L. Meng, H. Wei, A. Nagel, B. J. Wiley, L. E. Scriven, N. D. J., *Nano Lett.,* **2006**, 6, 2249.

[18] J. Gulden, O. M. Yefanov, A. P. Mancuso, V. V. Abramova, J. Hilhorst, D. V. Byelov, I. Snigireva, A. Snigirev, A. V. Petukhov, I. A. Vartanyants, *Phys. Rev. B,* **2010**, 81, 224105.

[19] J. M. Rodenburg, A. C. Hurst, A. G. Cullis, B. R. Dobson, F. Pfeiffer, O. Bunk, C. David, K. Jefimovs, I. Johnson, *Phys. Rev. Lett.,* **2007**, 98, 034801.

[20] A. Bosak, I. Snigireva, K. S. Napolskii, A. Snigirev, *Adv. Mater.,* **2010**, 22, 3256–3259.

[21] M. Dierolf, A. Menzel, P. Thibault, P. Schneider, C. M. Kewish, R. Wepf, O. Bunk, F. Pfeiffer, *Nature,* **2010**, 467, 436.

[22] M. M. Van Schooneveld, J. Hilhorst, A. V. Petukhov, T. Tyliszczak, J. Wang, B. M. Weckhuysen, F. M. F. De Groot, E. De Smit, *Small,* **2011**, 7, 804.

[23] H. Wei, L. Meng, Y. Jun, D. J. Norris, *Appl. Phys. Lett.,* **2006**, 89, 241913.

[24] S. W. Hell, Nature, **2007**, 316, 1153.

[25] B. Harke, C. K. Ullal, J. Keller, S. W. Hell, *Nano Lett.,* **2008**, 8, 1309.

[26] W. Stober, A. Fink, E. Bohn, *J. Colloid Interf. Sci.,* **1968**, 26, 62.

[27] A. P. Philipse, A. Vrij, *J. Colloid Interf. Sci.,* **1989**, 128, 121.

[28] K. V. Kaznatcheev, C. Karunakaran, U. D. Lanke, S. G. Urquhart, M. Obst, A. P. Hitchcock, *Nucl. Instrum. Methods,* **2007**, 582, 96.

[29] aXis2000 is free for noncommercial use. It is written in Interactive Data Language (IDL) and available online: *http://unicorn.mcmaster.ca/aXis2000.html*

[30] J. R. Kremer, D. N. Mastronarde, J. R. McIntosh, J. Struct. Biol., **1996**, 116, 71.

[31] H. Friedrich, P. E. de Jongh, A. J. Verkleij, K. P. de Jong, *Chem. Rev.,* **2009**, 109, 1613.

[32] M. Obst, J. Wang, A. P. Hitchcock, *Geobiology,* **2009**, 7, 577.

[33] G. A. Johansson, T. Tyliszczak, G. E. Mitchell, M. Keefe, A. P. Hitchcock, *J. Synchrotron Radiat.,* **2007**, 14, 395.

[34] J. C. Crocker, D. G. Grier, *J. Colloid Interface Sci.,* **1996**, 179, 298.

[35] J. E. G. J. Wijnhoven, W. L. Vos, *Science,* **1998**, 281, 802.

[36] S. V. Grigoriev, K. S. Napolskii, N. A. Grigoryeva, A. V. Vasilieva, A. A. Mistonov, D. Y. Chernyshov, A. V. Petukhov, D. V. Belov, A. A. Eliseev, A. V. Lukashin, Y. D. Tretyakov, A. S. Sinitskii, H. Eckerlebe, *Phys. Rev. B,* **2009**, 79, 045123.
[37] P. V. Braun, P. Wiltzius, *Adv. Mater.,* **2001**, 13, 482.
[38] M. C. D. Mourad, E. J. Devid, M. M. Van Schooneveld, C. Vonk, H. N. W. Lekkerkerker, *J. Phys. Chem. B,* **2008**, 112, 10142.
[39] P. Thibault, M. Dierolf, A. Menzel, O. Bunk, C. David, F. Pfeiffer, *Science,* **2008**, 321, 379.

Variable Dislocation Widths in Colloidal Crystals of Soft Thermosensitive Spheres

6

Detailed measurements of the core structure of Shockley partial dislocations in colloidal crystals are presented. In crystalline arrays of micrometer sized thermosensitive particles, the interactions between the colloidal building blocks were tuned by changing the temperature. Individual dislocation cores were observed in a confocal microscope and their behaviour as function of temperature was studied. The obtained results qualitatively agree with the Peierls theory and are promising for further studies in which both Peierls stress and dislocation core width are measured simultaneously.

6.1   INTRODUCTION

For over a century, since the early experiments on colloids by Perrin,[1] colloidal particles have been employed as a model system for atoms. The merits of using colloids as model atoms are reflected in a process like crystal nucleation. Nucleation of an atomic crystal occurs very quickly and on a length scale of Angstroms or nanometers, precluding a real space study of crystal nucleation. The same process in a colloidal system takes minutes and can be observed directly with a microscope,[2] while the physics behind the process remains essentially the same. This way, homogeneous nucleation,[2] as well as nucleation at impurity dopants[3] has been studied in great detail. In many ways, this example illustrates one of the key aspects of colloid science; to generate slow and seeable model systems.

Another area of research that could benefit from the colloidal approach is dislocation theory. The historic Peierls theory was put forward shortly before the outbreak of world war 2.[4] Over a decade later, the core structure of dislocations was observed experimentally for the first time, as a result of the advent of high resolution electron microscopy.[5-7] Despite these advances a direct comparison between core structure and macroscopic material properties has not been made, due to the large spread in involved length and time scales. Here, we will discuss a system of colloidal thermosensitive spheres that readily crystallize into a random hexagonal close packed lattice. Through analysis of confocal microscopic images, Shockley partial dislocations can be identified and characterized. The width of the dislocations is shown to be strongly dependent on temperature, which is discussed within the light of the generalized Peierls theory[8] and the properties of the thermosensitive colloids. The results hold promise for experiments in which dislocation width and crystal shear strength are measured simultaneously.

Colloidal crystals form an ideal system to study dislocations. Due to the weak interactions between the particles, the formation of dislocations costs relatively little energy. In addition, because of the extremely low stacking fault energy, Shockley partial dislocations can exist in unpaired form, *i.e.* without the presence of a second Shockley partial with Burgers vectors adding up to a full dislocation.[9] Other peculiar dislocations have been observed, such as discrete Shockley partials and partial dislocation loops.[10] The size of the colloids allows for an accurate microscopic characterization of a crystallite, where particle coordinates can be determined in 3D through the use of image analysis software.[11]

6.2   EXPERIMENTAL

The colloidal system used in this consists of spheres made of a copolymer of N-Isopropylacrylamide (NIPAm) and acrylic acid (AAc) monomers,

cross-linked with N,N'-Methylenebisacrylamide (BIS) and dyed with 4-methylaminoethylmethacrylate-7-nitrobenzo-2-oxa-1,3-diazol (NBD-MAEM) for confocal microscopy. PolyNIPAm spheres are known for their strong temperature dependent behavior,[12] with their diameter decreasing up to a factor of three upon heating them above the lower critical solution temperature (LCST) at 32°C.[12] Below this temperature, the polymer has a hydrophilic character and is swollen with water. Above it, hydrophobic interactions dominate; most of the water is expelled and the particle shrinks.[13] This property has enabled studies of annealing and controlled melting [14, 15] of colloidal crystals through control over the particle volume fraction. The added acrylic acid monomer adds pH-dependent size behavior to the spheres, as well as additional charge stabilization at high temperature and pH.[16] Particles containing 11 mol% of acrylic acid at pH8 were used here. In addition to high stability at temperatures above the LCST, these particles have reduced thermosensitive behavior, enabling more accurate control of the particle volume fraction. The particles were crystallized in flat capillaries consisting of two microscope slides glued on top of each other with two small glass slides as spacer in between. Particle concentration was 2.2 wt%, a concentration that was empirically found to produce large crystals throughout the sample. Measurements were performed in a Linkam THMS600 stage mounted on top of a Nikon TE2000 inverted microscope with a C1 confocal scan head. Crystals were imaged layer by layer at temperatures ranging from 20 to 40°C. Above 40°C, dye fluorescence was quenched too much to obtain reliable particle coordinates.

6.3   THEORY

Stress-strain relations in solids can be described by elastic relations based on the well-known Hooke's law, which describes the extension of a spring in the direction of an applied stress. This relation also holds for most solids, as long as the load does not exceed the elastic limit. In fact, Hooke's law is just a special case of the general expression $\varepsilon_{ij} = S_{ijkl}\sigma_{kl}$, which describes the strain ε_{ij} tensor of a solid under a stress σ_{kl}. Instead of the spring constant, strain and stress are now related by the fourth rank compliance tensor S_{ijkl}. The subscripts i,j,k,l can assume values from 1 to 3, corresponding to the three real space dimensions. The compliance tensor therefore consists of 81 individual components. In practice, however, the ij and jj components, as well as the kl and lk components are equivalent, reducing the amount of independent components to 36 for a highly anisotropic material. In the fcc solid, the symmetry of the crystal further reduces the amount of independent components to 3, when the elastic constants are defined within the [100], [010], [001] or $\{x, y, z\}$ basis. In such a reduced set of components, the relevant stress, strain and compliances are given in a shorthand notation:

$$\begin{bmatrix} \varepsilon_{xx} \\ \varepsilon_{yy} \\ \varepsilon_{zz} \\ 2\varepsilon_{yz} \\ 2\varepsilon_{xz} \\ 2\varepsilon_{xy} \end{bmatrix} = \begin{bmatrix} \varepsilon_1 \\ \varepsilon_2 \\ \varepsilon_3 \\ \varepsilon_4 \\ \varepsilon_5 \\ \varepsilon_6 \end{bmatrix}; \begin{bmatrix} \sigma_{xx} \\ \sigma_{yy} \\ \sigma_{zz} \\ \sigma_{yz} \\ \sigma_{xz} \\ \sigma_{xy} \end{bmatrix} = \begin{bmatrix} \sigma_1 \\ \sigma_2 \\ \sigma_3 \\ \sigma_4 \\ \sigma_5 \\ \sigma_6 \end{bmatrix}; \begin{matrix} S_{xxxx} = S_{yyyy} = S_{zzzz} = S_{11} \\ S_{xxyy} = S_{yyzz} = S_{xxzz} = S_{12} \\ S_{yzyz} = S_{xzxz} = S_{xyxy} = S_{44} \end{matrix}$$ (6.1)

Using this notation, the compliance tensor looks as follows:

$$\begin{bmatrix} \varepsilon_1 \\ \varepsilon_2 \\ \varepsilon_3 \\ \varepsilon_4 \\ \varepsilon_5 \\ \varepsilon_6 \end{bmatrix} = \begin{bmatrix} S_{11} & S_{12} & S_{12} & 0 & 0 & 0 \\ S_{12} & S_{11} & S_{12} & 0 & 0 & 0 \\ S_{12} & S_{12} & S_{11} & 0 & 0 & 0 \\ 0 & 0 & 0 & S_{44} & 0 & 0 \\ 0 & 0 & 0 & 0 & S_{44} & 0 \\ 0 & 0 & 0 & 0 & 0 & S_{44} \end{bmatrix} \begin{bmatrix} \sigma_1 \\ \sigma_2 \\ \sigma_3 \\ \sigma_4 \\ \sigma_5 \\ \sigma_6 \end{bmatrix}$$ (6.2)

The inverse relation $\sigma_{ij} = C_{ijkl}\varepsilon_{kl}$, where C_{ijkl} is called the stiffness tensor, is as follows:

$$\begin{bmatrix} \sigma_1 \\ \sigma_2 \\ \sigma_3 \\ \sigma_4 \\ \sigma_5 \\ \sigma_6 \end{bmatrix} = \begin{bmatrix} C_{11} & C_{12} & C_{12} & 0 & 0 & 0 \\ C_{12} & C_{11} & C_{12} & 0 & 0 & 0 \\ C_{12} & C_{12} & C_{11} & 0 & 0 & 0 \\ 0 & 0 & 0 & C_{44} & 0 & 0 \\ 0 & 0 & 0 & 0 & C_{44} & 0 \\ 0 & 0 & 0 & 0 & 0 & C_{44} \end{bmatrix} \begin{bmatrix} \varepsilon_1 \\ \varepsilon_2 \\ \varepsilon_3 \\ \varepsilon_4 \\ \varepsilon_5 \\ \varepsilon_6 \end{bmatrix}$$ (6.3)

The components of the compliance and stiffness tensors are related according to [17]:

$$S_{11} = \frac{C_{11} + C_{12}}{C_{11}^2 + C_{11}C_{12} - 2C_{12}^2}$$

$$S_{12} = \frac{-C_{12}}{C_{11}^2 + C_{11}C_{12} - 2C_{12}^2}$$ (6.4)

$$S_{44} = \frac{1}{C_{44}}$$

For the calculations in this chapter the Poisson ratio for compression along a <112> direction was required. As the elastic constants for the fcc solid are usually

defined within the [100], [010], [001] or {x, y, z} basis, basis vectors of a new set had to be introduced:

$$\vec{\alpha} = \frac{1}{\sqrt{6}}(\vec{x} + \vec{y} - 2\vec{z})$$

$$\vec{\beta} = \frac{1}{\sqrt{3}}(\vec{x} + \vec{y} + \vec{z}) \qquad (6.5)$$

$$\vec{\gamma} = \frac{1}{\sqrt{2}}(\vec{x} - \vec{y})$$

Because the fcc solid is not fully isotropic, the elastic constants change upon rotation of the basis to the {α, β, γ} set. In order to facilitate the rotation of the compliance tensor, an anisotropy factor was introduced:

$$A = S_{11} - S_{12} - 2S_{44} \qquad (6.6)$$

The compliance tensor can be split into the sum of an isotropic part, where A was subtracted from all S_{11} components, and an anisotropy tensor:

$$S = \begin{bmatrix} S_{12} + 2S_{44} & S_{12} & S_{12} & 0 & 0 & 0 \\ S_{12} & S_{12} + 2S_{44} & S_{12} & 0 & 0 & 0 \\ S_{12} & S_{12} & S_{12} + 2S_{44} & 0 & 0 & 0 \\ 0 & 0 & 0 & S_{44} & 0 & 0 \\ 0 & 0 & 0 & 0 & S_{44} & 0 \\ 0 & 0 & 0 & 0 & 0 & S_{44} \end{bmatrix} + \begin{bmatrix} A & 0 & 0 & 0 & 0 & 0 \\ 0 & A & 0 & 0 & 0 & 0 \\ 0 & 0 & A & 0 & 0 & 0 \\ 0 & 0 & 0 & 0 & 0 & 0 \\ 0 & 0 & 0 & 0 & 0 & 0 \\ 0 & 0 & 0 & 0 & 0 & 0 \end{bmatrix}$$

Upon rotation, the isotropic part remains unchanged and only the diagonal anisotropy matrix has to be transformed. The fact that this matrix possesses only three non-zero elements simplifies calculations significantly with respect to the original compliance tensor. For the calculation of the rotation, the transition matrix Ω is introduced:

$$\Omega = \begin{pmatrix} \vec{\alpha} \cdot \vec{x} & \vec{\alpha} \cdot \vec{y} & \vec{\alpha} \cdot \vec{z} \\ \vec{\beta} \cdot \vec{x} & \vec{\beta} \cdot \vec{y} & \vec{\beta} \cdot \vec{z} \\ \vec{\gamma} \cdot \vec{x} & \vec{\gamma} \cdot \vec{y} & \vec{\gamma} \cdot \vec{z} \end{pmatrix} \qquad (6.8)$$

The new compliance tensor can subsequently be calculated according to:

$$S_{ijkl}^{\alpha\beta\gamma} = S_{ijkl,isotropic}^{xyz} + A(\Omega_{ix}\Omega_{jx}\Omega_{kx}\Omega_{lx} + \Omega_{iy}\Omega_{jy}\Omega_{ky}\Omega_{ly} + \Omega_{iz}\Omega_{jz}\Omega_{kz}\Omega_{lz}) \quad (6.9)$$

From the new compliance tensor, the Poisson ratios in the new basis can be determined. The Poisson ratio is defined as the dilation or compression of the lattice in a direction perpendicular to an applied compressive or dilative stress,
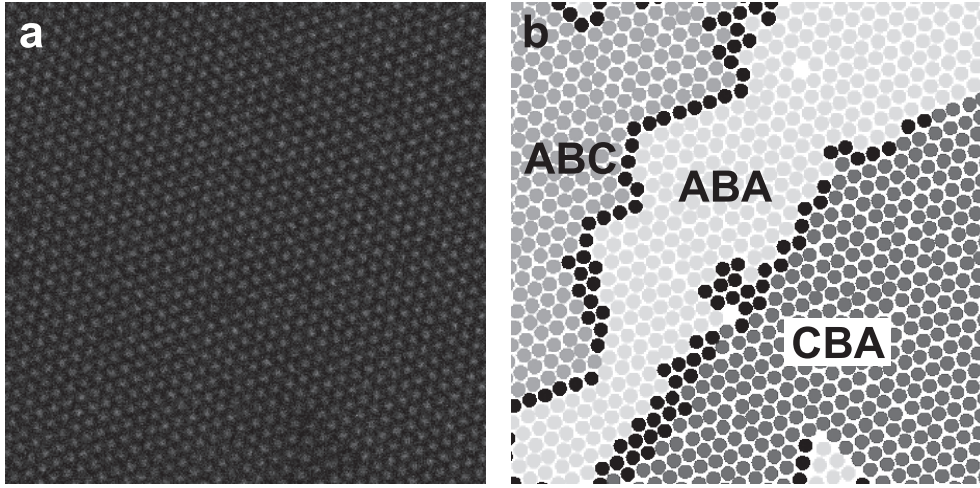
Figure 6.1. Panel (a) shows a typical confocal micrograph of a crystal of polyNIPAm spheres. (b) Schematic representation of the crystal structure of the same crystal layer as in (a). Different shades of grey represent different crystal structures. Black particles have no identifiable crystal structure, as they are located in dislocation cores. Note that for the distinction between crystal structures the particle positions in the layers above and below the characterized layer are used as well.

i.e. the off-diagonal components of the matrix. The response has to be calculated relative to the compression or dilation in the direction of the stress:

$$\nu_{\alpha\beta} = -\frac{S_{\alpha\alpha\beta\beta}}{S_{\alpha\alpha\alpha\alpha}} \tag{6.10}$$

Using the elastic constants given by Tretiakov and Wojciechowski [18], the Poisson ratio can now be calculated for compressive and dilative stresses within the new basis.

6.4   RESULTS & DISCUSSION

Figure 6.1a shows a typical micrograph of a single layer. After finding particle coordinates using an algorithm in IDL (interactive data language),[11] the crystalline environment of all particles was determined as described before,[10] resulting in images like figure 6.1b. The different shades of grey distinguish two crystal phases: hexagonal close packed (hcp) or face centered cubic (fcc), with different stacking directions (ABA vs. BAB or ABC vs. CBA), all in all four different crystal configurations. When a transition between two phases is found, a partial dislocation must be present. This can be confirmed by plotting the coordinates of the two layers containing the dislocation on top of each other (figure 6.2a-c). Here, the lattice deformation around the dislocation core is clearly visible. It was found that dislocation lines most often run along the <112> or <110> directions and that
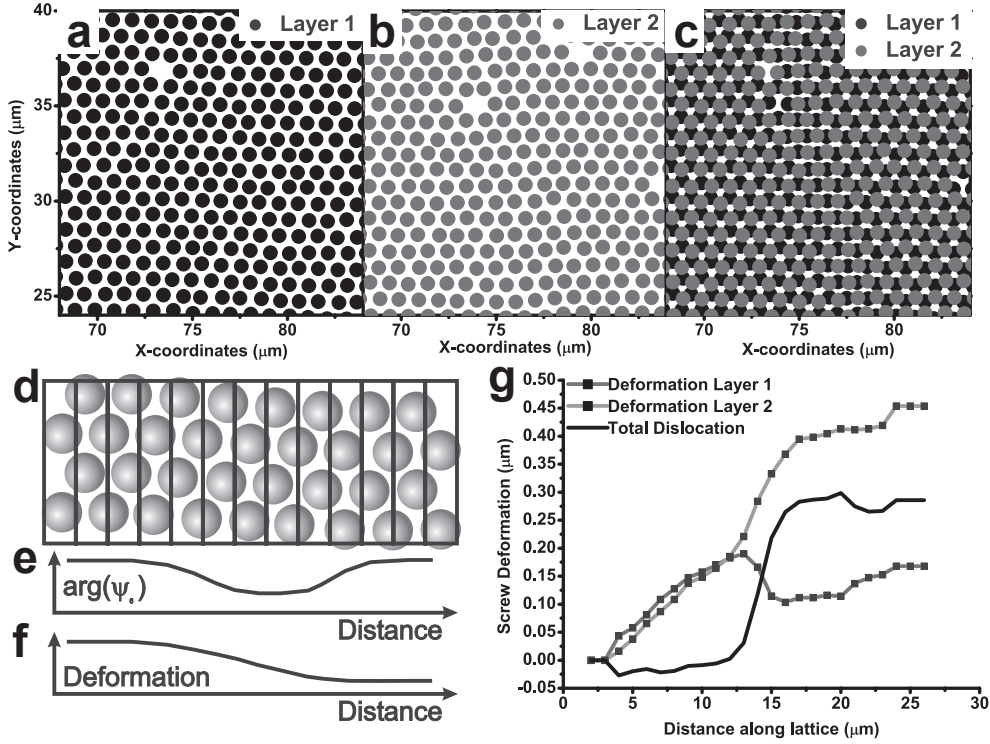
Figure 6.2. Panels (a)-(c) show two subsequent hexagonal layers containing a dislocation. The individual layers in (a) and (b) look normal, but their overlay in (c) shows a dislocation running from top to bottom at x ≈ 76 μm. In (d) the lines are shown that divide a layer into bins. For each bin, the lattice orientation is determined, resulting in a plot like (e). The corresponding lattice deformation is given in (f). Panel (g) shows the lattice deformations for two individual layers and their difference; a dislocation.

in both cases dislocations with dominating screw component were by far the most abundant, as expected from their lower line energy.[19]

Using the hexagonal order parameter ψ_6, the extent of the deformation in the dislocation core region can be accurately determined.[9] The ψ_6 order parameter, defined as

$$\psi_{6,j} = \frac{1}{N} \sum_{k=1}^{N} e^{-6i\theta_{jk}} \qquad (6.11)$$

for each particle j, is a measure for the hexagonal order of a particle. It is a complex sum over all N in-plane nearest neighbors of a particle, where θ_{jk} is the angle between a fixed reference axis and the vector between particle j and neighbor particle k. The absolute value of this parameter is an indication of the (hexagonal) crystallinity of the particle within a layer and its complex argument indicates the local orientation of the lattice with respect to the reference axis. Around a dislocation, the lattice is

Figure 6.3. Panel (a) shows a representation of the 30° Shockley partial that was studied. The dislocation line lies vertic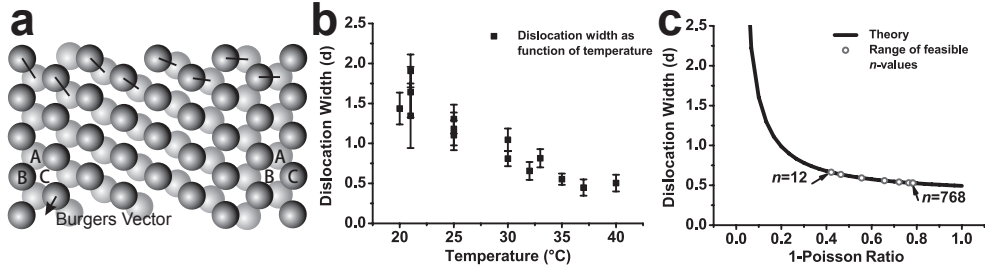al in this image, along the <110> direction. The Burgers vector is shown in the bottom left and has a 30° angle with respect to the dislocation line. The lines connecting the particles in the top of the figure illustrate the gradual deformation of the lattice as particles move from a B to a C position. Panel (b) is a plot of the measured dislocation widths as a function of temperature. Panel (c) shows calculated dislocation widths as function of the Poisson ratio. The empty circles represent dislocation widths that can be obtained for soft spheres using the elastic constants calculated by Tretiakov et al. [19].

slightly deformed, resulting in a different orientation of the lattice. To quantify the extent of the deformation, the argument of ψ_6 is averaged over several particles in a small bin parallel to the dislocation line (figure 6.2d-e). The tangent of this angle multiplied with the width of the bin gives the deformation in the direction along the dislocation line, *i.e.* the screw component of the dislocation.[9] The sum of the deformations in all bins provides a detailed curve of the total screw component of the dislocation in a single layer (figure 6.2f). Since the dislocation is contained between two layers, both layers have to be characterized and the difference taken to result in the final dislocation curve (figure 6.2g). The resulting curve can be fitted to an arctangent function of the form

$$u(x) = \frac{b}{\pi} \arctan \frac{x}{w} - \frac{b}{2}$$ (6.12)

which corresponds to the original solution that was obtained by Peierls for a dislocation profile[4] and is still used in more complex solids.[8] Such a fit yields the Burgers vector b and the dislocation width w. Two times w is the range in which half of the lattice deformation is contained. This is a measure for the plastic shear strength of a crystal according to:

$$\sigma_p = \frac{2\mu}{1-\nu} e^{-4\pi w/b}$$ (6.13)

where μ is the bulk shear modulus of the material, and ν is the Poisson ratio, as discussed in chapter 1, equation 1.2.

Using the ψ_6 method, the behavior of unpaired 30° Shockley partials with dislocation lines along <110> was studied as a function of temperature. The configuration of such a dislocation is shown in figure 6.3a. It is a dislocation of

mixed type with a dominating screw character. The widths of the dislocations, as obtained from arctangent fits of the deformation profiles are plotted as function of temperature in figure 6.3b. It is evident that the dislocation width is strongly temperature dependent, decreasing by a factor of 4 between 20 and 40°C. According to equation 6.3, this implies that the Peierls stress strongly increases and the crystal "hardens". This may seem counterintuitive at first, as crystals of polyNIPAm particles have been shown to melt upon heating in earlier studies. [14] However, the added acrylic acid co-monomers reduce the thermal response of the particles in such a way, that their reaction to temperature change is not strong enough to melt the crystal. In fact, in these measurements, due to slow heating and sample equilibration, the particle number density increased under the influence of gravity upon heating, keeping particle volume fraction approximately constant over the whole temperature range. The observed decrease of dislocation width and consequent crystal hardening is therefore not caused by a gradual transition towards the melting point, but has to be due to a change in the interaction potential between the particles. As the temperature is increased and particles shrink, their repulsive potential becomes steeper.[20] This is commonly described by a potential of the form $U = \varepsilon(\frac{\sigma}{r})^n$, where σ represents the particle diameter, r is the interparticle distance and ε is a measure for the strength of the repulsion. The factor n in the exponent determines the "hardness" of the potential. If n goes to infinity, the particles behave like hard spheres, while for n equals 1 the potential is Coulomb-like. For polyNIPAm particles, the value of n has been shown to range from 12 at low temperature to hard-sphere-like at high temperatures.[20] Even though the particles used in this study do not shrink dramatically, the value of n is still increasing with temperature.

A recent study by Tretiakov *et al.*[18] shows that the value of n strongly influences the crystal Poisson ratio; a parameter that has been known to affect dislocation widths since Peierls' early calculations. As this influence strongly depends on the crystal structure and dislocation orientation, the dependence of dislocation width on Poisson ratio was calculated for this particular case, following the procedure in ref.[8]. In this reference, influences of the width of partial dislocations on the dislocation energy are discussed for a dissociated screw dislocation along the <110> direction in an fcc {111} plane, within a Peierls framework. The basis of this framework is that the energy of a dislocation consists of an elastic contribution and a misfit energy. The elastic part results from the compression or dilation of the lattice around a dislocation. Elastic energy is minimized by spreading the deformations as far as possible, increasing dislocation width. The misfit energy, caused by non-ideal alignment of particles across the glide plane, is minimized by localizing the deformations. Therefore, w is large for dominating elastic interactions and small for dominating misfit energy.

81

Chapter 6: Temperature Dependent Dislocation Width

Assuming arctangent deformations for the edge and screw parts of the <110> screw dislocation, elastic theory can be applied to obtain an expression for the elastic energy as function of the lattice deformations. For a dissociated screw dislocation along <110> in an fcc lattice, the solution is given by [8]

$$E_{el} = \frac{\mu b^2}{4\pi} \left\{ \ln\left[\frac{R}{2w}\right] - \frac{1}{4}\ln\left[\left(\frac{d}{2w}\right)^2 + 1\right] + \frac{1}{12(1-\nu)}\ln\left[\left(\frac{d}{2w}\right)^2 + 1\right] \right\} \quad (6.14)$$

Here, μ is the {111} plane shear modulus, R the dislocation cut-off radius, ν the Poisson ratio and d the separation distance between partial dislocations.

Looking more closely at the various terms in equation 6.14, it can be noted that the first term corresponds to the elastic energy of a full screw dislocation, while the second and third terms arise from the splitting of the dislocation in two Shockley partials. As the partial dislocations studied here were present in unpaired form due to the low stacking fault energy, d is much larger than w. In this particular case, if the energy of the stacking fault between the two partials is assumed to be negligible, the misfit energy, E_A, depends linearly on dislocation width:

$$E_A = \frac{\sqrt{3}\mu b^2}{2\pi^2 c} w \quad (6.15)$$

where c is the {111} interlayer spacing. This expression results from an integration of the misfit potential over the whole dislocation.[8] The stable dislocation width is located at the minimum of the sum of elastic and misfit contributions. This can be found by setting the derivative with respect to w of the total energy, $E_{tot} = E_A + E_{el}$, to zero:

$$\frac{\partial E}{\partial w} = \frac{\mu b^2}{4\pi} \left\{ \frac{-1}{w} + \frac{1}{2}\frac{d^2}{4w^3 + d^2 w} - \frac{1}{6(1-\nu)}\frac{d^2}{4w^3 + d^2 w} + \frac{2\sqrt{3}}{\pi c} \right\} = 0 \quad (6.16)$$

where c is the fcc interlayer spacing for {111} planes. For $d \gg w$, this leads to

$$w = \frac{\pi c}{2\sqrt{3}} \left(\frac{1}{2} + \frac{1}{6(1-\nu)} \right) \quad (6.17)$$

with ν and c as the only variables. As the measurements of w were scaled to the particle diameter d, c can be removed from equation 6.7 to yield

$$\frac{w}{d} = \frac{\pi}{3\sqrt{2}} \left(\frac{1}{2} + \frac{1}{6(1-\nu)} \right) \quad (6.18)$$

A plot of dislocation widths as function of Poisson ratio is shown in figure 6.3c (note that the x-axis displays 1 minus the Poisson ratio). Comparing this image with figure 6.3b, it can be seen that the full range of measured dislocation widths can be covered by changing the Poisson ratio between 0 and 1. Although values

82

of the Poisson ratio above 0.5 are impossible for isotropic materials, in anisotropic materials the Poisson ratio can assume arbitrary values for specific directions[18]. Using the values of the elastic constants presented by Tretiakov *et al.*[18] for fcc crystals of soft spheres, the Poisson ratio for compression along <112> could be calculated as a function of particle softness (details of the calculations are given in the theory section). This allowed for a direct comparison between dislocation width and particle softness. Figure 6.3c displays the range of calculated dislocation widths obtained for particles with values of the softness parameter n ranging from 12 to 768, *i.e.* from fully swollen polyNIPAm particles to almost hard spheres.

Dislocation widths ranging from 0.78 particle diameters for soft spheres ($n = 12$) to 0.42 particle diameters for hard spheres ($n = 768$) were obtained from the calculations. The trend follows the measured results qualitatively; as temperature increases, particle repulsive potentials become steeper (larger n), reducing the Poisson ratio as shown in figure 6.3c, thereby reducing dislocation width. This shows that standard dislocation theory is suitable for qualitatively describing dislocation behavior as a function of temperature in soft sphere crystals.

Quantitatively, there is a discrepancy between measurements and calculations, mainly at low temperature. Considering the assumptions that have been made in the model, the discrepancy is small, but some improvements may yield even better agreement. On the one hand, the trial functions for the dislocation profile may be too simple and on the other hand more complex models should be used for calculations of the elastic and misfit energies. Both possibilities have been discussed by Schoeck.[8] An absolute comparison between theory and experiment, therefore, requires extension of the currently available theoretic framework. Efforts in this direction may benefit from further measurements on colloidal systems, for example on the effects of dislocation orientation on its width. Additionally, state-of-the-art microscopy setups, combined with shear cells[21] or optical tweezers,[22] may be employed to directly measure the Peierls stress, while simultaneously measuring dislocation widths, allowing another direct comparison between Peierls theory and experiment.

6.5 CONCLUSIONS

In conclusion, we have presented direct measurements of dislocation widths as function of temperature in soft-sphere colloidal crystals. The observed trend can be explained qualitatively within a Peierls framework applied to hexagonal crystals. The trend is found to be due to a change in particle interaction potential, leading to a decrease in Poisson ratio with temperature. Quantitatively, the range of measured widths exceeds the predicted values by a factor of ~2 to 3, indicating the necessity for further theoretical efforts to close this gap. Despite this absolute

discrepancy, results are promising for further experiments where Peierls stress and dislocation width are measured simultaneously.

6.6   REFERENCES

[1] J. Perrin, *Ann. Chim. Phys.,* **1909**, 18, 5.

[2] U. Gasser, E. R. Weeks, A. Schofield, P. N. Pusey, D. A. Weitz, *Science,* **2001**, 292, 258.

[3] V. W. A. de Villeneuve, R. P. A. Dullens, D. G. A. L. Aarts, E. Groeneveld, J. H. Scherff, W. K. Kegel, H. N. W. Lekkerkerker, *Science,* **2005**, 309, 1231.

[4] R. Peierls, *Proc. Phys. Soc.,* **1940**, 52, 34.

[5] W. Bollmann, *Phys. Rev.,* **1956**, 103, 1588.

[6] J. W. Menter, *Proc. R. Soc. London, Ser. A,* **1956**, 236, 119.

[7] P. B. Hirsch, R. W. Horne, M. J. Whelan, *Philos. Mag.,* **1956**, 1, 677.

[8] G. Schoeck, *Philos. Mag. A,* **1994**, 69, 1085.

[9] V. W. A. De Villeneuve, Ph.D. Thesis, Utrecht University, **2008.**

[10] J. M. Meijer, V. W. A. De Villeneuve, A. V. Petukhov, *Langmuir,* **2007**, 23, 3554.

[11] J. C. Crocker, D. G. Grier, *J. Colloid Interf. Sci.,* **1996**, 179, 298.

[12] R. Pelton, *Adv. Colloid Interf. Sci.,* **2000**, 85, 1.

[13] R. Pelton, *J. Colloid Interf. Sci.,* **2010**, 348, 673.

[14] A. M. Alsayed, M. F. Islam, J. Zhang, P. J. Collings, A. G. Yodh, *Science,* **2005**, 309, 1207.

[15] Y. Peng, Z. Wang, A. M. Alsayed, A. G. Yodh, Y. Han, *Phys. Rev. Lett.,* **2010**, 104, 205703.

[16] M. Karg, I. Pastoriza-Santos, B. Rodriguez-Gonzalez, R. von Klitzing, S. Wellert, T. Hellweg, *Langmuir,* **2008**, 24, 6300.

[17] A. F. Bower, Applied Mechanics of Solids, CRC Press, Boca Raton**, 2010**.

[18] K. V. Tretiakov, K. W. Wojciechowski, *J. Phys. Chem. B,* **2008**, 112, 1699.

[19] D. Hull, D. J. Bacon, Introduction to Dislocations, fourth edn., Elsevier Ltd., Oxford**, 2001**.

[20] D. M. Heyes, A. C. Branka, *Soft Matter,* **2009**, 5, 2681.

[21] D. Derks, H. Wisman, A. van Blaaderen, A. Imhof, *J. Phys.-Condens. Mat.,* **2004**, 16, S3917.

[22] M. Yada, J. Yamamoto, H. Yokoyama, *Phys. Rev. Lett.,* **2004**, 92, 185501.

7

Intrinsic Stacking Faults and Persistent Face Centered Cubic Crystal Growth in Sedimentary Colloidal Hard Sphere Crystals

Hard sphere crystal growth is a delicate interplay between kinetics and thermodynamics, where the former is commonly thought to favor a random hexagonal close packed structure and the latter leads to a face centered cubic crystal. In this chapter, the presence of slanted stacking faults in sedimentary colloidal crystals is discussed. Correlations between these persisting faults and large regions of fcc structure are investigated and the mechanism of nucleation of the faults is elucidated. The results are promising for use in epitaxial growth of colloidal crystals, where proper templating could lead to almost perfect fcc crystals with selectively incorporated defects.

7.1   INTRODUCTION

Since the simulations by Alder and Wainwright and Wood and Jacobsen in the 1950's,[1, 2], and the acquisition of the experimental hard sphere phase diagram by Pusey and van Megen in 1986,[3] colloidal hard spheres have been the "Fruit Flies" of crystallization studies. This can be attributed to the fact that they form the simplest system that can undergo a fluid-to-solid phase transition and are therefore very well suited to study processes like crystal nucleation.[4] Additionally, colloids of sizes close to a micrometer have slow dynamics and can be imaged using microscopy, allowing real-time, real-space data acquisition on a single particle level.[4, 5] Much theoretical and experimental effort has been spent on determining the equilibrium crystalline state of the colloidal hard sphere solid.[3, 6-12] By now, consensus has been reached that the face centered cubic (fcc) crystal structure is thermodynamically the most stable one. Nonetheless, a random hexagonal close packed (rhcp) structure is often observed experimentally. Because of the extremely small free energy difference of less than 10^{-3} k_BT per sphere between the fcc and hexagonal close packed (hcp) structures, the kinetics of crystallization usually traps the crystal in the metastable rhcp structure. These rhcp crystals have been found to relax to the thermodynamically stable fcc structure over a period of at least several months.[10-12] Rearrangement occurs via regions of twinned fcc crystal that slowly grow at the expense of rhcp regions.[11]

In order to study the equilibrium structure of hard sphere crystals in a controlled way, as well as studying bulk nucleation and growth, the majority of research on this topic has been focused on "ideal" hard sphere systems.[6, 11-13] The most important aspects for "ideal" behavior are particle interactions, polydispersity and sample disturbances. First of all, by matching the refractive index of the particles to that of the solvent, van der Waals forces are kept to a minimum to ensure purely repulsive, hard-sphere-like interactions.[3] Secondly, particle polydispersity significantly affects nucleation and growth speeds[14, 15] as well as the final crystal structure[16] and the concentration of defects.[17] When polydispersity in a sample is too high, crystallization can only occur through size fractionation.[18-21] These strong effects necessitate the use of monodisperse particles when studying the crystallization behavior of colloidal hard spheres. Thirdly, due to the small interaction energy between hard sphere colloids even very small perturbations, like movement of a sample from storage to a measurement setup, can have a significant effect on the crystal structure.[12] Some of these disturbances, which are the most difficult to control, are caused by gravity. By using small particles, matching the density of the colloids to the solvent[11, 12] or even sending colloids into space,[6, 22] this factor was minimized in various accounts in order to study the true crystallization behavior of the system. Crystals grown under such milli- or microgravity conditions grow

out into a random mixture of fcc and hcp layers with equal probabilities to find either. In systems where gravity is not minimized, a tendency towards fcc growth is usually observed. The effects of gravity on crystal structure can be twofold. First, at a colloid volume fraction higher than the freezing transition (49.4 vol%), fast crystal nucleation in the bulk is followed by sedimentation of the growing crystallites. Second, in the case that a low volume fraction of colloids is used, the particles sediment to the sample bottom, where the concentration will eventually exceed the freezing transition. This results in crystals that grow upwards from the sample bottom.[13] Too fast sedimentation may result in a glassy sediment, from which crystals may start growing from the top downwards over a period of weeks to months.[23] In the first case, at a high volume fraction, the sedimenting crystallites are subject to frictional shear. Since shear is well known to promote fcc growth through reorganization of the hexagonal crystal layers, the increased fraction of fcc in these crystals is no surprise.[12] In the latter case, resulting in so-called sedimentary crystals, an fcc fraction of 80% was observed by Pusey et al. contrary to the value of 50% observed for density matched crystals.[13] This was explained by a slower growth for sedimentary crystals with respect to crystals grown at high initial volume fraction. When growth is slower, the crystal has more time to explore the free energy landscape and find the energy minimum before further crystal growth traps it in a fixed position. Hoogenboom *et al.* quantitatively investigated the structure of sedimentary crystals as a function of crystal growth speed and showed that crystallization speed indeed affected crystal structure.[24] Lower initial particle volume fractions (slower crystallization) led to larger fcc fractions. Similar findings from simulations were recently published by Marechal *et al.*, confirming the role of thermodynamics in the final structure of slowly grown sedimentary crystals.[25]

In this chapter, the local crystal structure of sedimentary colloidal crystals grown from dispersions with a high initial volume fraction and particles with a small gravitational length (fast sedimentation) is discussed. Although the sedimentation flux J, as defined by Marechal *et al.*, does not differ much from the values in refs.[24] and [25], different final crystal structures are obtained. These findings are discussed and a growth mechanism related to the presence of crystalline defects is proposed.

7.2   EXPERIMENTAL

Particle Synthesis

Cross-linked, dyed poly(methyl methacrylate) particles with a diameter of 892 nm (polydispersity 2.9%, sample A) and 828 nm (polydispersity 4.0%, sample B) synthesized by Bosma et al.[26] were used in this study. The given sizes and polydispersities were determined by scanning electron microscopy (SEM) and

confirmed with static light scattering (SLS). Polydispersities obtained from SLS tend to be overestimated, but serve to verify the values obtained from SEM. Samples were prepared by centrifuging a stock dispersion, removing the supernatant and redispersing the particles in cis-decalin at a desired volume fraction, ranging from 0.1 to 0.5. Samples were loaded into small Chromacol 2-SV vials with sawed-off bottom replaced by Menzel Gläser 22 mm #1 microscope cover slips. The cover slips were glued to the bottom using Araldit AW2101 epoxy glue with HW2951 hardener. This glue is resistant to cis-decalin, preventing influences of depletion attraction due to dissolved polymer.

Samples were left to sediment over a period of typically 40 hours before imaging. In a few cases, measurements were started directly after tumbling the sample to follow the process of crystallization in time.

Confocal microscopy

A Nikon Eclipse TE2000U inverted microscope fitted with a Nikon C1 confocal scan head was used for obtaining high resolution images of the colloidal crystals. For illumination, a Spectra Physics 163C air cooled ion laser was used at a wavelength of 488 nm. For 3D reconstruction of particle positions, volumes of 40x40x20 μm^3 were imaged with 512x512x400 voxels, a significant oversampling in the out-of-plane direction considering the confocal resolution of 153 nm in the x–y plane and 566 nm in the out-of-plane direction. Oversampling was found to improve the accuracy of particle detection in the out-of-plane direction.

Image and data analysis

Particle coordinates in 2D and 3D were obtained using algorithms described before.[27, 28] From these coordinates, the crystalline environment of all particles was determined using an algorithm in Interactive Data Language (IDL), based on the method described by Ackland and Jones for their program "Ballviewer".[29] In short, the distribution of angles between the bond vectors of all nearest neighbors of a particle strongly depends on its crystalline environment. By analyzing this distribution, an fcc or hcp environment can be assigned to a particle. In addition, a similar algorithm was written based on the analysis of the angular distribution of second nearest neighbors, which are located at an average distance of $d\sqrt{2}$. In an fcc structure, second nearest neighbors are arranged in an octahedron around the reference particle, while the hcp structure results in a trigonal prism configuration. Both algorithms gave similar results. Also, detection artifacts where single particles within an fcc region were assigned with hcp structure by the Ballviewer program were reproduced. Therefore, an additional filter was introduced, requiring a particle with hcp surroundings to have at least three nearest neighbors with the same packing, otherwise it was marked as undetermined. For determining the

correlation parameters P_{ff} and P_{hf}, the total number of fcc next nearest neighbors was counted for all fcc and hcp particles in a crystal, respectively. This was divided by the total number of next nearest neighbors of the two types of particles. The reason that correlations between next nearest neighbors were studied is that this avoids biased correlations. Six out of twelve first nearest neighbors will always have the same crystalline environment as the reference particle as they are in the same {111} plane. This does not hold for the next nearest neighbors. Therefore, correlation artifacts are avoided.

7.3   RESULTS & DISCUSSION

7.3.1   3D crystal structure

Figure 7.1a and 7.1b show typical confocal micrographs of a sedimentary colloidal crystal used in this study. The plane of imaging is perpendicular to gravity and parallel to the bottom of the cell. This is the cause of the hexagonal orientation of the particles in the plane of imaging. Several types of disorder are indicated by arrows. Arrow 1 indicates a vacancy, the most common and most studied defect in colloidal crystals.[17, 30-33] The second arrow points to a linear defect that was discussed in a recent publication by Meijer et al.[34] This defect is characterized by a rectangular arrangement of the particles, and is a special manifestation of a Shockley partial dislocation. Across the defect, interparticle positional correlations are changed and the crystalline environment (fcc or hcp) of the particles may change.[34, 35] The third type of defect (arrow 3) very much resembles the configuration of the linear defect, with the particles surrounding it forming a rectangular configuration. The difference lies in the fact that, upon changing the position of the focal plane of the microscope, particles on one side of the defect become blurred, while they remain in focus on the other side (arrows in figure 7.1b). This implies a height step across the defect, similar to what was recently observed for convectively assembled colloidal crystals (see chapter 3 or ref [36]). By measuring through crystals layer by layer, it was found that the third type of defect could persist through many consecutive layers, suggesting a planar nature rather than a linear one. To investigate this further, several confocal datasets of single crystals in volumes of 40x40x20 μm^3 were collected. From these datasets, particle positions could be reconstructed in 3 dimensions. Subsequently, the coordinates were loaded into the program Ballviewer by Ackland and Jones. [29] This program is designed to determine the crystalline environment of particles from the positions of their nearest neighbors. Two plots from this program are shown in figure 7.1c and 7.1d. For clarity, smaller subsets of the original 40x40x20 μm^3 were used. Red particles have hcp surroundings, while green ones are in an fcc environment. Blue particles correspond to a body centered cubic phase, but
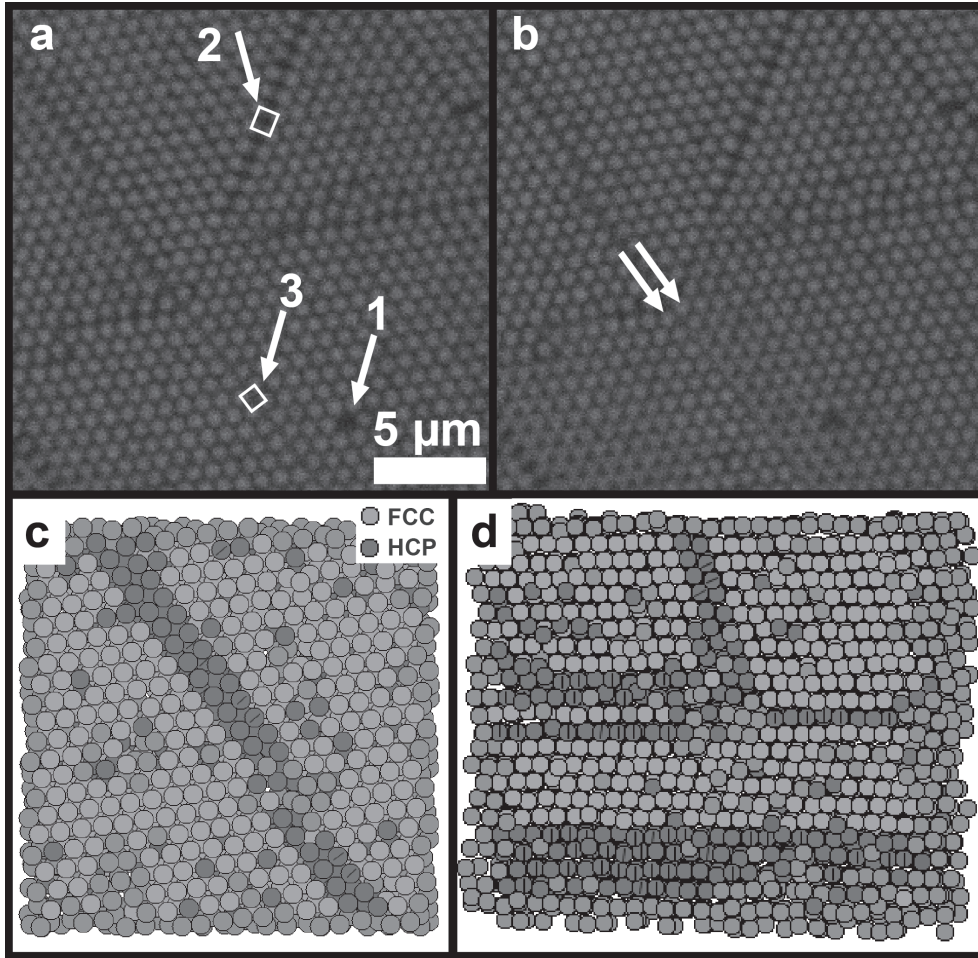
Figure 7.1. Panels (a) and (b) display the same crystalline layer imaged with slightly different positions of the confocal plane. In (a), arrows 1, 2 and 3 point to a vacancy, a Shockley partial dislocation and a slanted stacking fault, respectively. Panels (c) and (d) show Ballviewer images in which the stacking of particles was determined. Panel (c) contains a view of a (111) plane parallel to the substrate, while (d) contains a view along the fault with gravity running from top to bottom. All crystals shown are grown from sample B particles.

since this stacking is only assigned to individual particles, this has no physical meaning and the stacking of these particles can be viewed as coincidental. They can be considered to have no determined crystal structure, like the grey particles. The same holds for the single red particles in regions of fcc crystal. Due to Brownian motion, the particle centers have shifted from their ideal lattice positions and are wrongly identified by the algorithm. Since they are in perfect fcc regions, hcp coordination is impossible and the particle stacking should be considered to be

undetermined or fcc. Figure 7.1c displays a hexagonally oriented plane parallel to the substrate. Two lines of particles in hcp environment can be seen, with the particles lined up in rectangles. The defect persists for several layers. Figure 7.1d displays a view along the length of the line defect, with gravity running from top to bottom of the image. Several hcp layers can be seen running horizontally in this figure. These belong to stacking disorder in the growth direction. The two hcp planes running almost vertically correspond to the red lines in figure 7.1c. The height step across the defect is clearly visible and it can be concluded that the defects indeed have a planar nature, in the form of a slanted stacking fault on a different {111} plane from the one parallel to the substrate. This conclusion matches with X-ray diffraction experiments on slanted stacking faults in convectively assembled colloidal crystals.[36] Similar defects, resulting from misfit dislocations, have been studied in great detail before in epitaxially grown colloidal crystals with {100} planes parallel to the substrate.[37] Here, the origin of the stacking faults does not lie in the presence of misfit dislocations, as will be discussed later. The real surprise, lies in the areas surrounding the slanted stacking faults. While unfaulted regions of the crystals usually adopt an rhcp structure pure fcc crystals are typically observed surrounding the slanted faults, as can be seen in figure 7.1c and 7.1d. This raises the question whether the stacking faults are the cause or the result of the fcc growth. On the one hand, they can affect the growth by lifting the degeneracy of the (111) plane during growth, as suggested for Lennard-Jones (LJ) systems by van de Waal.[38] On the other hand, slow crystal growth may result in randomly stacked crystals with a preference towards fcc. In such crystals relatively large fcc regions may grow by chance. Subsequently, slanted stacking faults can be formed in such regions by small disturbances to the sample after crystal growth or through compression of the crystal.[25, 37]

7.3.2 Analysis of randomness

In order to investigate the origin of these defects and their surroundings, a closer investigation into the final crystal structure was performed. In most studies on the hard sphere crystal structure, the parameter α is used to characterize the fraction of layers with fcc environment. Randomly stacked crystals have an α-value of 0.5, while a value of 1 indicates a perfect fcc structure. The value of α can be easily determined from diffraction experiments,[39] as well as from microscopy. However, as Solomon and Solomon[35] pointed out, the value of α alone does not fully describe the internal structure of the crystal. A crystal consisting of equally large perfect fcc and hcp regions (block structure) will give the same α value as a crystal with alternating fcc and hcp layers (alternating structure) or a completely random structure with equal amounts of fcc and hcp. Therefore they introduced an additional parameter from polymer science, that discriminates between the various
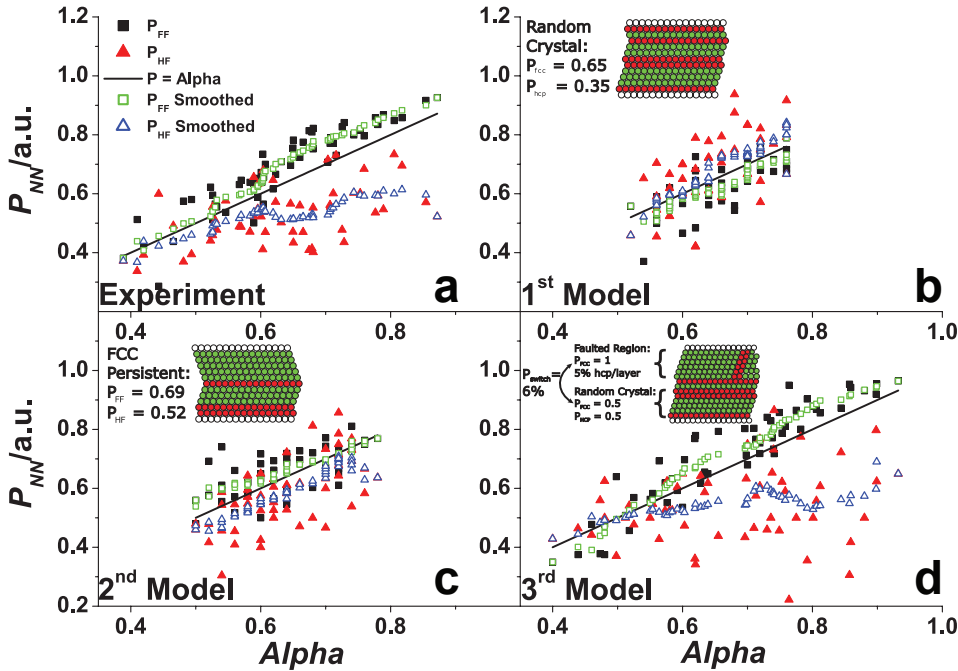
Figure 7.2. Measured (a) and simulated (b)–(d) values for P_{ff} and P_{hf}. Closed squares and triangles correspond to P_{ff} and P_{hf} respectively. The black line is where P equals $α$. Open squares and triangles result from 5 point adjacent averaging of the P_{ff} and P_{hf} datasets to display a clearer trend. Measured data were obtained from both samples A and B.

structures.[35] This parameter, $χ$, is defined as follows:

$$χ = \frac{\left[fcc / hcp \right]}{\left[fcc \right]\left[hcp \right]} \tag{7.1}$$

where [fcc/hcp] is the probability to find an fcc layer followed by an hcp layer and [fcc] and [hcp] are the probabilities for finding an fcc or an hcp layer respectively (thus [fcc] equals $α$ and [hcp] equals 1-$α$). In a random crystal, [fcc/hcp] is simply [fcc] times [hcp], hence $χ$ equals 1. In a block structure, fcc/hcp pairs will hardly be present, while in the alternating structure, 50% of the crystal will consist of fcc/hcp sequences (the other being hcp/fcc sequences). This leads to $χ$-values of 0 and 2, respectively. For discriminating between randomly grown crystals and crystals with a non-random layer sequence, values of $α$ and $χ$ have to be obtained from many crystals. The limited statistics due to the finite size of single crystals result in a wide distribution of $α$ and $χ$-values. Plotting a probability distribution of $χ$-values for many crystals can give a good indication of the preferred structure,[35] but in this case, it was more instructive to plot individual values of $χ$ against the values of $α$ obtained from the same crystals.

92

In this study the persistence and stacking parameters were determined per particle instead of per layer, to be able to account for stacking disorder in four different <111> directions. Slightly different, but related parameters were used, which were found to differentiate more clearly between randomly grown crystals and crystals with a preferred layer sequence. These parameters, labeled P_{ff} and P_{hf}, are defined as the probability to find an fcc particle as a next nearest neighbor (*i.e.* at a distance $d\sqrt{2}$ from the reference particle) to a random fcc or hcp particle, respectively. P_{ff} relates to χ via:

$$\chi = \frac{\alpha\left(1-P_{ff}\right)}{\alpha\left(1-\alpha\right)} = \frac{\left(1-P_{ff}\right)}{\left(1-\alpha\right)} \tag{7.2}$$

Here $\alpha\,(1-P_{ff})$ equals [fcc/hcp], the probability to find an fcc layer (α) followed by an hcp layer ($P_{fh} = 1-P_{ff}$). Figure 7.2a shows results obtained by plotting P_{ff} and P_{hf} against α for 55 crystallites. Although there is a considerable spread in the data, with α ranging from less than 0.4 to 0.9, and P_{ff} values showing an even larger spread, two trends are evident. First, the values of P_{ff} increase with α and are slightly larger than α over the whole data range. This means that on average, the probability to find fcc particles as neighbors of other fcc particles is larger than the average probability of finding an fcc particle at a random position in the crystal. Hence, fcc particles tend to cluster (analogous to $\chi < 1$). This effect is most pronounced at values of α around 0.7, as can be seen from the smoothed data in figure 7.2a. At lower values, P_{ff} is approximately equal to α, indicating random crystals. At higher values, both P_{ff} and α approach their maximum value of 1 and therefore trend towards each other, although P_{ff} remains larger than α over the whole data range, keeping χ-values below 1. The second trend that can be observed from figure 7.2a is that the values of P_{hf} show a large spread, but are grouped around an almost constant value of approximately 0.5. The smoothed curve shows only a slight trend towards higher values with increasing α. It appears that the probability to find fcc particles next to hcp particles is always close to 50%. Independent of α, stacking around hcp particles seems to be random.

7.3.3 Crystal growth models

Although the results point towards a non-random growth of the crystal, where fcc regions are formed due to preferred clustering rather than by chance, simple, one-dimensional coin-flipping "crystal growth" models were used to verify this. These models generate 50-layer rhcp crystals from varying input parameters. The simplest version generated a sequence of fcc and hcp layers, with a probability of 65% to generate an fcc layer and 35% to generate hcp, as dictated by the average value of α measured in the experiments. The resulting data for 55 crystals "grown" in this way are presented in figure 7.2b. The values of α, P_{ff} and P_{hf} are all scattered

around the input value of 65% probability for fcc formation. Both P_{ff} and P_{hf} increase with α, with a small spread around its values. These results are to be expected for truly random crystals: whether an fcc or an hcp layer is taken as a reference, the probability to find fcc in a neighboring layer is similar to the average probability of finding it anywhere in the crystal (χ=1). The results confirm the hypothesis that the experimental crystal structures are not random.

A second model was designed to use the measured values of P_{ff} and P_{hf} as growth parameters: upon an existing fcc layer, there was be a 69% chance to grow another fcc layer, while upon an hcp layer, the probability was 52%. The validity of this model would point to the existence of a non-negligible surface tension between regions of fcc and hcp crystal. Again, these input values were chosen to represent the average experimental output values. Resulting data are shown in figure 7.2c. It is clear that using the average measurement data as input parameters does not yield a trend similar to the experimental results. P_{ff} values are on average slightly larger than for the random crystals, while P_{hf} values are somewhat smaller. The spread of the data points also does not reflect the measurements. Since this strongly depends on the amount of layers in a crystal (more layers decrease the spread of the data), the amount of layers in simulated crystals was decreased, but the results did not resemble the experimental findings. Several other input values were changed as well and it was found that the output for P_{hf} was always grouped around its input value, with a trend following α. P_{ff} also grouped around its input values, but did not trend with α. For crystal structures with values of α close to 0.5, this resulted in values of P_{ff} that were often much larger than 0.5, contrary to the experimental observation that P_{ff} is approximately equal to α in this region.

Finally, it was found that the experimental data could be accurately described by a third model. This model was designed to grow perfectly random crystals (50% fcc), with a small probability for a transition into a faulted region with almost perfect fcc growth. An equal probability to return to a random crystal was also introduced. In the faulted region, each fcc layer contained 5% of hcp particles with P_{hf} values of 0.5 assigned to them. Although similar results were obtained without these hcp particles, they were included to resemble the double stacking faults present in the real crystals. Figure 7.2d shows results obtained within this model with a probability of 6% per layer to nucleate a faulted region. This value was found to produce the best results, which are remarkably similar to the measurements. For smaller nucleation probabilities, a large fraction of the α-values was grouped around 0.5, indicating a decreased number of fcc crystals with faulted regions and growth of perfectly random crystals. For larger nucleation probabilities, the distribution of α-values narrowed, as faulted regions often nucleated and closed again within a single crystal and most crystals obtained similar fractions of faulted region. However, a relatively wide range of nucleation values ranging roughly
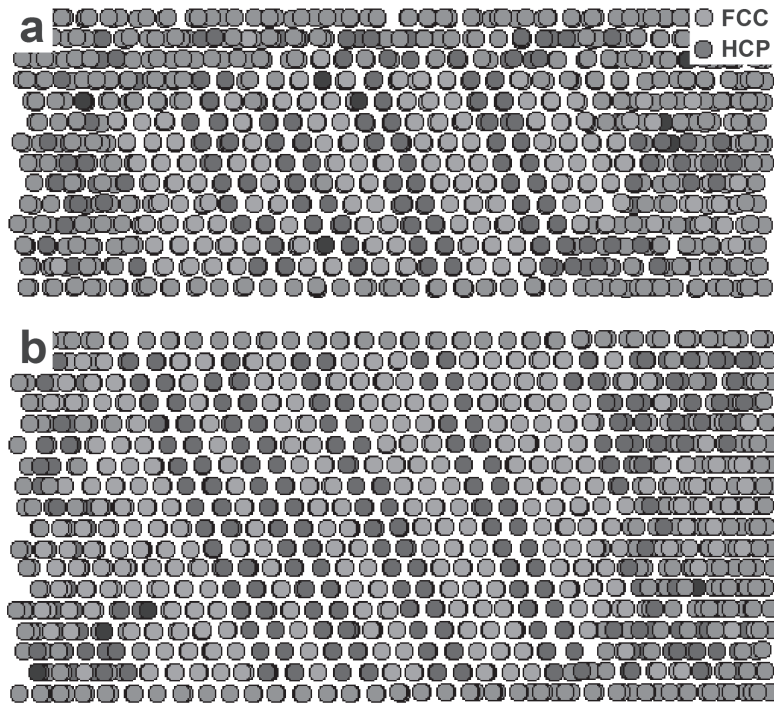
Figure 7.3. A crystal imaged during (a) and after (b) growth. During growth the slanted stacking faults are already present and are found to persist after growth.

from 1 to 10% gave satisfactory results resembling the experimental data.

These results seem to indicate that crystal growth occurs through a mechanism favoring fcc growth in certain regions, while in others a random structure is favored. This coexistence of rhcp and fcc regions in single crystallites has in fact been observed before in single crystal X-ray diffraction measurements[40] and can now be explained from an "atomistic" origin. However, another plausible explanation was presented recently.[25] Here, the spread in the data is explained through the thermodynamic stability of the fcc phase. In larger crystals, the energy difference between fcc and hcp becomes larger and the likelihood that fcc stacking dominates in a crystal is increased. Assuming a log-normal distribution of crystal sizes, results similar to those in figure 7.2a were obtained.[25]

7.3.4   Role of stacking faults

Although it remains unclear whether the data in figure 7.2a are caused by a distribution in domain sizes or by the presence of slanted stacking faults, the role of the latter was further investigated. Their ubiquitous presence in the regions of fcc stacking suggests that a mechanism similar to the one proposed for LJ systems by van de Waal[38] may govern crystal growth. Measurements show that the defects

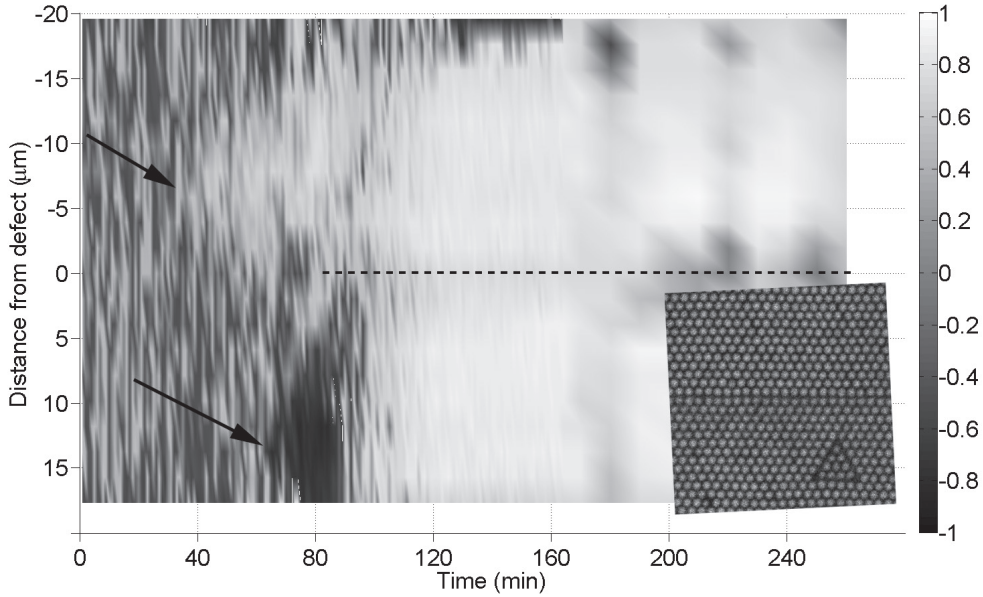**Figure 7.4. Image of the crystal structure and crystallinity of a single layer as function of time. The greyscale represents the value of (2α-1)ψ₆. This is 1 for a fully crystalline fcc layer and -1 for hcp. For disordered regions it is close to 0. The orientation of the crystal is as shown in the inset. For each time, the values of (2α-1)ψ₆ are averaged along the x-axis of the inset. The y-axis of the figure corresponds to the y-axis of the inset. The slanted fault is positioned at y = 0. Before crystallization starts (0 < t < 40 min) the data strongly fluctuate. At t = 40 min, an fcc region begins to crystallize, as indicated by the top arrow. At t = 60 min, an hcp layer forms in the bottom. As soon as this region grows out and reaches the defect, it rearranges to an fcc position.**

are present from the start of crystal growth and are copied through many layers (figure 7.3). However, the mechanism of layer nucleation at the surface defect line, as proposed by van de Waal,[38] does not occur. New layers may nucleate anywhere on the surrounding (111) planes in either hcp or fcc positions, as shown in figure 7.4.

This figure gives a schematic view of crystallization around a slanted stacking fault as a function of time. The inset on the bottom right shows the orientation of the crystal. The direction of gravity is into the plane. At every point in time (*x*-axis), the average crystallinity as well as the crystal structure were determined as a function of distance to the defect line (*y*-axis). The crystallinity is determined using the bond order parameter

$$\psi_{6,j} = \frac{1}{N} \sum_{k}^{N} e^{6i\theta(\overrightarrow{r_{jk}})} \tag{7.3}$$

which describes the angular distribution of nearest neighbors *k* around a central particle *j*. In a crystalline environment, the absolute value of ψ_6 is close to 1, while

96

in a fluid, it fluctuates strongly, with an average value of 0.4. The crystal structure was determined for every particle according to the method described by Meijer *et al.*[34] In bins parallel to the defect (*i.e.* along the horizontal axis of the inset in figure 7.4), the average values of ψ_6 and α were combined into a single parameter β ($\beta =(2\alpha-1)\psi_6$). Fcc particles with high crystallinity give a β-value of 1, while hcp particles yield a value of -1. Disordered regions or mixed hcp/fcc regions result in values around 0.
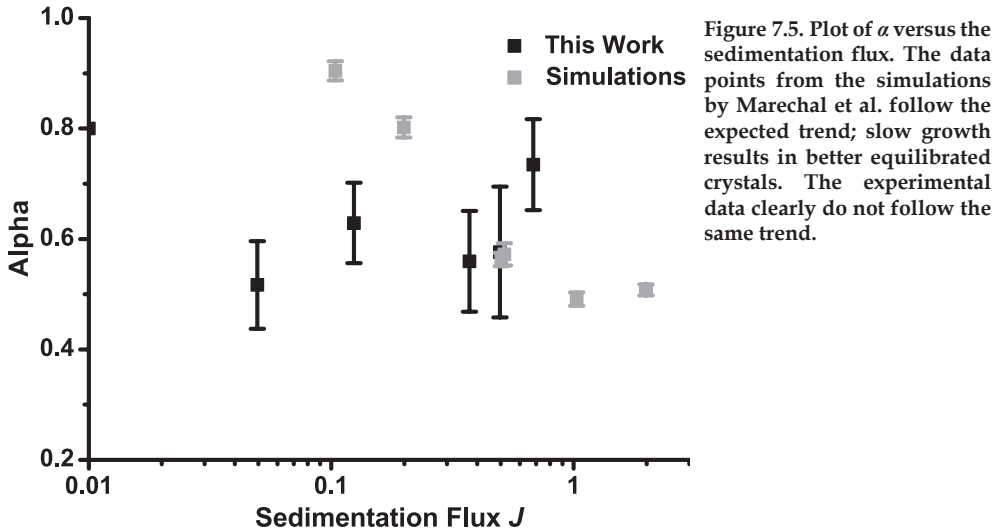
In figure 7.4, white and black bins correspond to particles with positive and negative β-values, respectively. The dashed line in the middle corresponds to the position of the defect line. Until t = 40 min., the small values of β indicate that no crystal is present. Nucleation is found to occur at two separate positions away from the defect line: after 40 minutes at X ≈ 13 μm in fcc structure (top arrow) and after 60 minutes at X ≈ 34 μm in hcp structure (bottom arrow). The crystalline regions are found to grow over time, until they fill the whole picture at t ≈ 100 min. Around that moment, the whole hcp layer reorients to an fcc position. In other measurements, we observed similar behavior, although it could take a few hours before reorganization would occur.

The nucleation away from the defect line can be explained by the difference in particle interactions between LJ and hard sphere systems. In the LJ system, particles will preferably bind at the defect, as they will have a fourfold coordination instead of a threefold coordination on a flat (111) plane. This results in more attraction and a lower energy barrier for layer nucleation. In hard sphere crystals, attraction does not play a role, and the sole effect of entropy on the positioning of individual particles near the defect could well be negligible. However, a full layer growing next to a defect in the wrong position leaves a considerable volume near the defect unoccupied, which is entropically unfavorable. Also, closing the defect and forming a perfect hexagonal layer on top of it, requires the formation of a stair-rod dislocation. The energy of such a dislocation is of the order of tens of k_BT according to

$$E_{SR} = \frac{\mu b^2}{4\pi(1-\nu)}\ln\left(\frac{e^2 R}{2w}\right) \tag{7.4}$$

where μ is the crystal shear modulus, b is the dislocation Burgers vector, e is the base of the natural logarithm and R is the size of the crystal. Termination of the stacking fault therefore is a costly process in terms of free energy and persistence is much more likely. The cost of creating hcp layers and of closing the defect could promote the rapid restructuring of hcp layers to fcc positions during or shortly after crystal growth, as shown in figure 7.4. Similar fast initial annealing has been observed in earlier studies using light scattering.[41] In addition, the final slow restructuring towards a twinned fcc structure observed for homogeneously nucleated crystals[11,

Figure 7.5. Plot of α versus the sedimentation flux. The data points from the simulations by Marechal et al. follow the expected trend; slow growth results in better equilibrated crystals. The experimental data clearly do not follow the same trend.

[12] may be facilitated by the slanted stacking faults through a lowering of the activation barrier for layer rearrangement, since only a fraction of a layer has to move instead of a whole layer at once. It is noted that this growth mechanism for sedimentary crystallization differs from the one presented by Hoogenboom *et al.*,[24] who reported on the slow sedimentation of silica particles from dispersions with low starting concentrations (<1 vol%). There, fcc growth was explained as a result of the long time available for crystal layers to rearrange to their thermodynamically stable position before further crystal growth increased the energy barrier for rearrangement. In our system, initial concentrations range from 10 to 50 vol%, but the density difference with the solvent is much smaller and crystal growth speed is not much different from low concentration silica dispersions.

Both types of growth were considered in a recent simulation study by Marechal *et al.*[25], who investigated sedimentary hard sphere crystallization as a function of sedimentation flux J:

$$J = Pe \frac{D_0}{D_s^L} \frac{\phi_i}{\pi} \qquad (7.5)$$

with $Pe = mg\sigma / k_B T$ the sedimentation Péclet number, *i.e.* the ratio between the potential energy a particle loses upon sedimenting a distance corresponding to its own diameter and the thermal energy. D_0 is the Stokes-Einstein diffusion coefficient, φ_i is the initial volume fraction in the sample and D_s^L is the long time self-diffusion coefficient. The sedimentation flux provides a measure for the crystal growth speed that is applicable to a wide range of colloidal suspensions as it takes effects of gravity as well as concentration into account. Both high Péclet numbers and high volume fractions result in a large sedimentation flux and therefore fast

crystal growth. If growth is too fast, crystalline layers do not have time to rearrange towards their thermodynamically stable state before they are kinetically trapped by further crystal growth. For small values of J, crystals should grow slow enough to result in equilibrium structures, *i.e.* fcc crystals. A plot of α versus J confirmed this for their simulation data as well as for the data of Hoogenboom *et al.*[24] No evidence was found for an effect of slanted stacking faults on crystal growth.

The simulation data are reproduced in figure 7.5, along with the data obtained from the systems used in this study. The experimental data point at lowest J corresponds to an additional dataset of crystals grown in a density matched solvent at a φ_i of 0.40. It is clear that the data from this study differ from the data obtained by Marechal *et al.*[25] and therefore also from the data by Hoogenboom *et al.*[24] Although the sedimentation flux is comparable between all three studies discussed here, in this study particles with a smaller Péclet number and higher initial volume fraction were used. A crucial difference in crystallization results from this.[42] The lower the Péclet number of a dispersion, the more layers crystallize simultaneously in a first order phase transition at the onset of crystallization. After the first layers have nucleated, crystallization continues in a layer-by-layer fashion.[42] In a low-Péclet number dispersion, this region in which continued growth takes place (the region in which a fluid-solid interface is present) is much wider than at high Péclet number. These differences may account for the different dependence of α on J and may cause a defect mediated growth mechanism to become more important, but further experiments and simulations have to be performed to investigate this.

7.3.5   Defect nucleation

The appearance of slanted stacking faults in a sedimentary crystal is not trivial; the crystals grow on a flat substrate, yet a height difference is readily introduced. By investigating the region where the defect starts to grow in more detail, it was found that nucleation occurs at a line defect similar to the one indicated by arrow 2 in figure 7.1a. In a pure fcc crystal, such a line defect generates two hcp half-planes parallel to the substrate. As described by Meijer et al.,[34] a perfect hexagonal layer can close the defect again. For particles with a small gravitational length, a significant loss in gravitational energy can occur upon settling into one of the square coordinated sites in the line defect, as the height difference between a "normal" position in a new layer and a position in the defect is $0.17d$, where d is the particle diameter (figure 7.6a). In our system, this corresponds to a loss of $0.12\ k_BT$ per particle. This does not suffice to trap particles in the defect but it does significantly increase the occupancy of these positions. Once particles settle into the defect, a following layer cannot close the defect, hence it persists, including a height discontinuity at the defect line. A typical sequence of layers is shown in figure 7.6b–f. First, a perfect hexagonal layer is observed. On top of that, two half-
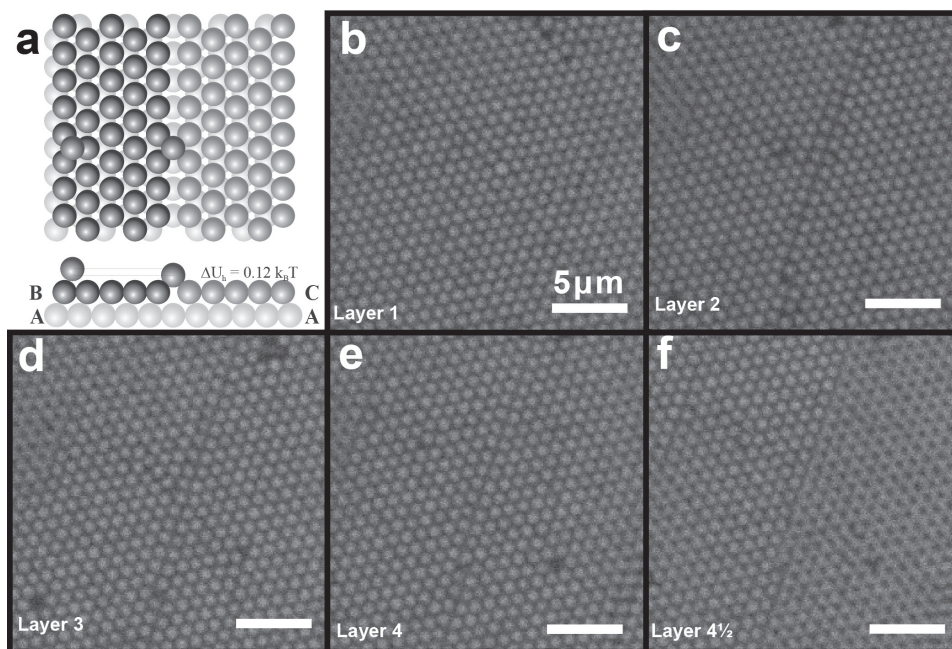
99

Figure 7.6. (a) is a schematic representation of a type two line defect, where a perfect hexagonal layer is covered by two half-layers that each occupy a different one of two possible positions. A particle sedimenting into the line defect lies 0.17d lower than its counterpart that is in a "normal" position. Panels (b)–(f) show the nucleation mechanism of a slanted stacking fault in a crystal grown from sample B particles.

layers are separated by a type two defect. In the next layer, the defect persists, but with the particles surrounding it packed closer together. One layer further, it contains a height difference, as is shown by the partly out-of-focus image 7.6f. As discussed, this mechanism requires particles with a small gravitational length. If the gravitational energy gain is too small, the defect will not be filled and a flat crystal will continue to grow. This was confirmed by Marechal *et al.*, who grew crystals at comparable sedimentation flux, but with different gravitational lengths.[42] They showed that for larger gravitational lengths, less slanted defects are grown. In our study, this was verified for density matched colloids, that did not produce the slanted defects and grew mostly rhcp crystals. The fact that the defects are easily nucleated on top of a line defect is promising for the possibility of selectively incorporating defects into otherwise pure fcc crystals. By epitaxial growth onto templates with built-in line defects, stacking faults may be grown at predefined positions in a crystal and may be used to locally affect the optical properties of photonic crystals. Results on selective incorporation of crystal defects are presented in chapter 8.

7.4   CONCLUSIONS

The findings presented here shed new light on the crystallization of colloidal hard spheres under gravity. They point towards a new mechanism that forces certain regions in the crystals to adopt fcc stacking, while other parts retain rhcp structure. The presence of slanted stacking faults in the regions of fcc stacking during and after crystallization and the rearrangement of crystal layers next to the defects strongly suggest their involvement in the forcing of the crystal stacking, although no unambiguous evidence for this was found. Since the final crystal structure strongly resembles the faulted, twinned structures observed in light and X-ray diffraction experiments on homogeneously nucleated colloidal crystals, we suspect that slanted stacking faults may play a role in the structural rearrangements towards the thermodynamically stable fcc structure.

7.5   REFERENCES

[1] B. J. Alder, T. E. Wainwright, *J. Chem. Phys.,* **1957**, 27, 1208.

[2] W. W. Wood, J. D. Jacobson, *J. Chem. Phys.,* **1957**, 27, 1207.

[3] P. N. Pusey, W. Vanmegen, *Nature,* **1986**, 320, 340.

[4] U. Gasser, E. R. Weeks, A. Schofield, P. N. Pusey, D. A. Weitz, *Science,* **2001**, 292, 258.

[5] A. Van Blaaderen, P. Wiltzius, *Science,* **1995**, 270, 1177.

[6] J. Zhu, M. Li, R. Rogers, W. Meyer, R. H. Ottewill, STS-73 Space Shuttle Crew, W. B. Russel, P. M. Chaikin, *Nature,* **1997**, 387, 883.

[7] L. V. Woodcock, *Nature,* **1997**, 385, 141.

[8] P. G. Bolhuis, D. Frenkel, S. C. Mau, D. A. Huse, *Nature,* **1997**, 388, 235.

[9] S. C. Mau, D. A. Huse, *Phys. Rev. E,* **1999**, 59, 4396.

[10] S. Pronk, D. Frenkel, *J. Chem. Phys.,* **1999**, 110, 4589.

[11] W. K. Kegel, J. K. G. Dhont, *J. Chem. Phys.,* **2000**, 112, 3431.

[12] V. C. Martelozzo, A. B. Schofield, W. C. K. Poon, P. N. Pusey, *Phys. Rev. E,* **2002**, 66.

[13] P. N. Pusey, W. Van Megen, P. Bartlett, B. J. Ackerson, J. G. Rarity, S. M. Underwood, *Phys. Rev. Lett.,* **1989**, 63, 2653.

[14] H. J. Schoepe, G. Bryant, W. van Megen, *Phys. Rev. E,* **2006**, 74, 060401.

[15] H. J. Schoepe, G. Bryant, W. van Megen, *J. Chem. Phys.,* **2007**, 127, 084505.

[16] S. Martin, G. Bryant, W. van Megen, *Phys. Rev. Lett.,* **2003**, 90, 255702.

[17] S. Pronk, D. Frenkel, *J. Chem. Phys.,* **2004**, 120, 6764.

[18] P. G. Bolhuis, D. A. Kofke, *Phys. Rev. E,* **1996**, 54, 634.

[19] D. A. Kofke, P. G. Bolhuis, *Phys. Rev. E,* **1999**, 59, 618.

[20] S. Martin, G. Bryant, W. van Megen, *Phys. Rev. E,* **2003**, 67, 061405.

[21] P. Bartlett, *J. Chem. Phys.,* **1998**, 109, 10970.

[22] Z. D. Cheng, P. M. Chaikin, J. X. Zhu, W. B. Russel, W. V. Meyer, *Phys. Rev. Lett.,* **2002**, 88, 015501.

[23] A. V. Petukhov, D. G. A. L. Aarts, I. P. Dolbnya, E. H. A. de Hoog, K. Kassapidou, G. J. Vroege, W. Bras, H. N. W. Lekkerkerker, *Phys. Rev. Lett.,* **2002**, 88, 208301.

[24] J. P. Hoogenboom, D. Derks, P. Vergeer, A. van Blaaderen, *J. Chem. Phys.,* **2002**, 117, 11320.

[25] M. Marechal, M. Hermes, M. Dijkstra, *J. Chem. Phys.,* **2011**, 135, 034510.

[26] G. Bosma, C. Pathmamanoharan, E. H. A. de Hoog, W. K. Kegel, A. van Blaaderen, H. N. W. Lekkerkerker, *J. Colloid Interf. Sci.,* **2002**, 245, 292.

[27] J. C. Crocker, D. G. Grier, *J. Colloid Interf. Sci.,* **1996**, 179, 298.

[28] J. P. Hoogenboom, P. Vergeer, A. van Blaaderen, *J. Chem. Phys.,* **2003**, 119, 3371.

[29] G. J. Ackland, A. P. Jones, *Phys. Rev. B,* **2006**, 73, 054104.

[30] C. H. Bennett, B. J. Alder, *J. Chem. Phys.,* **1971**, 54, 4796.

[31] A. Pertsinidis, X. S. Ling, *Nature,* **2001**, 413, 147.

[32] A. Pertsinidis, X. S. Ling, *Phys. Rev. Lett.,* **2001**, 87, 098303.

[33] A. Libal, C. Reichhardt, C. J. O. Reichhardt, *Phys. Rev. E,* **2007**, 75, 011403.

[34] J. M. Meijer, V. W. A. De Villeneuve, A. V. Petukhov, *Langmuir,* **2007**, 23, 3554.

[35] T. Solomon, M. J. Solomon, *J. Chem. Phys.,* **2006**, 124, 134905.

[36] J. Hilhorst, V. V. Abramova, A. Sinitskii, N. A. Sapoletova, K. S. Napolskii, A. A. Eliseev, D. V. Byelov, N. A. Grigorieva, A. V. Vasilieva, W. G. Bouwman, K. Kvashnina, A. Snigirev, S. V. Grigoriev, A. V. Petukhov, *Langmuir,* **2009**, 25, 10408–10412.

[37] P. Schall, I. Cohen, D. A. Weitz, F. Spaepen, *Science,* **2004**, 305, 1944.

[38] B. W. v. d. Waal, *Phys. Rev. Lett.,* **1991**, 67, 3263.

[39] A. J. C. Wilson, *Proc. Roy. Soc. London, Ser. A,* **1942**, 180, 277.

[40] I. P. Dolbnya, A. V. Petukhov, D. G. A. L. Aarts, G. J. Vroege, H. N. W. Lekkerkerker, *Europhys. Lett.,* **2005**, 72, 962.

[41] C. Dux, H. Versmold, *Phys. Rev. Lett.,* **1997**, 78, 1811.

[42] M. Marechal, M. Dijkstra, *Phys. Rev. E,* **2007**, 75, 061404.

8

Defect Engineering in Epitaxially Grown Sedimentary Colloidal Crystals

Electron beam and focused ion beam lithography are used to produce crystal growth templates that induce the growth of intrinsic stacking faults into sedimentary colloidal crystals at predetermined positions. On templates with hexagonal and square particle coordination, intrinsic stacking faults can be grown by including two dimensional projections of the cross-sections of intrinsic stacking faults with the {111} and {100} planes in the templates, respectively. With focused ion beam lithography, templates with a three dimensional structure mimicking a faulted {100} plane can be produced to control the direction of the incorporated stacking faults. This way, intergrowth structures can be created at a predetermined position in a crystal, resulting in small hollow channels running through it. Simulations indicate that channel corners and T-junctions can be grown by suitably designing the templates.

103

8.1   INTRODUCTION

Colloids are promising materials for the cheap and fast production of photonic crystals through self-assembly. Before applications can be realized, several hurdles remain to be taken. First, a robust method for synthesizing structures with a full photonic band gap has to be found. Second, the disorder that is intrinsic to self-assembled systems has to be reduced to a minimum, to prevent the closure of the band gap. Third, although this is not a requirement for some applications, control over the incorporation of defects at desired positions will add functionality for the realization of more complex applications.

For the first hurdle, the synthesis of structures with a full band gap, several methods have been proposed. Both the face centered cubic (fcc) and hexagonal close packed (hcp) structures, that can be formed from spherical colloids with isotropic interactions, do possess a full band gap if the crystal structure is inverted. [1, 2] This means that the voids in the colloidal crystal are filled up with a high refractive index materials and the colloids are etched out.[3, 4] However, the band gap of the resulting structures is very sensitive to disorder and is unsuitable for practical purposes.[5, 6] A structure that is more promising for generating a robust full photonic band gap is the diamond structure.[7] This structure does not form from single component dispersions of colloids with isotropic interactions, yet several pathways to synthesize it have been proposed.[8-10] Still, none of the proposed pathways has been realized experimentally and if the diamond structure is grown, the second hurdle has to be taken: growing the crystal with a sufficiently small concentration of defects.

Self-assembled colloidal structures are very susceptible to disorder.[11] The weak interparticle interactions cause colloidal crystals to have more defects than their metallic counterparts. For example, the equilibrium concentration of vacancies lies around 10^{-4} per unit cell for colloids,[12] while for copper at room temperature it is around 10^{-22}.[13] Experimentally, vacancy concentrations up to 1% have been reported for colloidal crystals, due to crystal growth kinetics.[14] The same comparison can be made for stacking faults. For atomic crystals, the model system for studying stacking faults has always been cobalt, which has ~10% stacking disorder in a preferred hcp structure.[15, 16] For colloidal crystals, 50% of stacking disorder is no exception,[17, 18] although thermodynamically, the crystals should be fully fcc.[19] As both vacancy and stacking fault concentrations in experiments are typically higher than expected on the basis of free energy calculations, kinetics play an important role in the formation of colloidal crystals. It was demonstrated by Hoogenboom *et al.* that reducing crystal growth speed indeed reduces the amount of stacking disorder.[20] One way to increase the degree of perfection in colloidal crystals is therefore to grow crystals slowly. Still, some degree of stacking disorder remains

in such crystals. Another method to reduce such disorder is the use of growth templates.[21] By promoting the growth of specific crystal planes that are unique to a single crystal structure (for example the fcc {100} plane or the hcp {1100} plane), crystals free of stacking faults can be grown.[21, 22] This procedure may be extended to force the growth of so-called Laves phases onto a binary colloid mixture[8] or to guide the growth of a faultless diamond structure in dispersions of patchy particles.[10] This way, the first two conditions for the formation of high quality self-assembled photonic crystals may be fulfilled at the same time.

Finally, if such crystals can be grown by templating, their functionality may be improved by growing faults at selected positions, creating optical propagation channels. For this purpose templates can be the method of choice as well, as was proposed in chapter 7. Figure 8.1a shows the mechanism that was proposed for the growth of slanted intrinsic stacking faults in sedimentary colloidal crystals. On hexagonal layers in such crystals, two layers may form in different positions and grow towards each other, leaving a line defect in between. If the gravitational length of the sedimenting particles is sufficiently small, they preferably settle into this defect line and prevent the growth of a perfect crystal on top. Further crystal growth should then result in the generation of slanted stacking faults in an fcc crystal structure. This growth mechanism will be employed in this chapter to selectively include defects in otherwise perfect fcc crystals. In addition, similar faults will be grown in crystals grown onto fcc {100} templates, which give more control over the crystal structure and intergrowth of faults. Finally, template designs for incorporating more advanced fault structures into fcc crystals by adding height steps are proposed. The analogy between the fcc and diamond structures makes the same methods applicable to a wider range of structures.

8.2   EXPERIMENTAL

Electron Beam Lithography

Substrates used for electron beam (E-beam) lithography consisted of glass microscope coverslips of 22 mm in diameter, coated with a layer of Indium Tin Oxide (ITO) with a resistivity of 100 $\Omega\cdot$square^{-1} (Diamond Coatings Ltd.). The substrates were cleaned by ultrasonication in a beaker containing isopropanol (Acros, "pure"), after which a layer of 950 kDa PMMA was spincoated onto the ITO-side from a 8 wt% solution in anisole (solution obtained from Microchem). A Delta 10 spincoater was used at 5000 rpm (ramp 1 s) for 60 seconds, after which the resist was baked at a 180°C hotplate for 60 seconds, producing a 400-500 nm thick resist layer.

Lithography was performed in a Raith E-Line setup with an acceleration voltage of 20kV and a electron dose varying from 1.8 to 4.0 pC/hole. A schematic

a

B $\Delta U_b = 0.12\ k_BT$ C
A   A

b

E-Beam Lithography

E-Beam
1.7-4.0 pC·hole^{-1}

PMMA Layer: ~500 nm, 950 kg·mol^{-1}

ITO coating: 100 Ω·square^{-1}

Glass microscope slide

c

Focused Ion Beam
Lithography

Focused
Gallium Ions

E-Beam

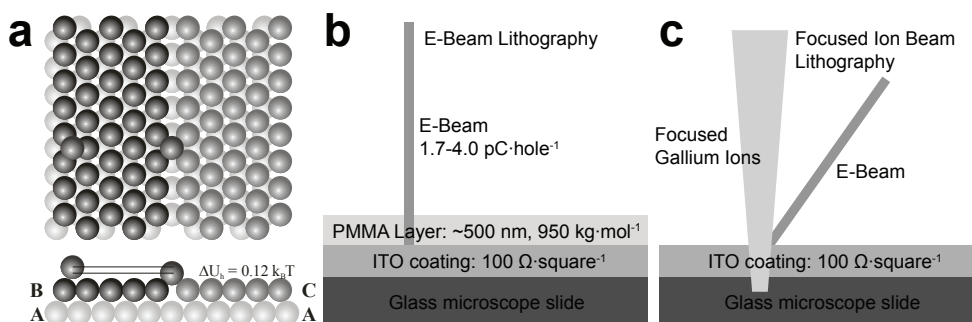ITO coating: 100 Ω·square^{-1}

Glass microscope slide

Figure 8.1. (a) Schematic representation of the nucleation mechanism of a slanted stacking fault on a {111} plane. Two half-planes in B and C positions grow towards each other, leaving a defect line in between. Sedimenting particles fall into the defect and start the growth of a slanted fault there. Panels (b) and (c) schematically show the setups used for creating the templates.

of the setup and of the substrate build-up is shown in figure 8.1b. Coordinate files were designed in advance and imported into the E-beam setup from ASCII files. Templates were produced in a sequential hole-by-hole fashion. Typically, 60-80 templates were generated per substrate, each with different electron dose or lattice spacing.

After writing the structures, templates were developed by removing the exposed materials in a 3 : 1 isopropanol : methyl isobutyl ketone solution (Scharlau, p.a.) for 60 seconds. Development was halted by rinsing the substrates in pure isopropanol for 60 seconds.

8.2.1 Focused Ion Beam Lithography

For focused ion beam (FIB) lithography the same glass-ITO substrates were used as for E-beam lithography, but no PMMA layer was spincoated on top. FIB uses Gallium ions to create structures in a substrate. The impact of these ions is large enough that almost any material can be etched without applying a resist. The FIB setup consisted of an FEI Nova Nanolab 600 Dualbeam apparatus and is schematically drawn in figure 8.1c.

First, the bar required to lower part of the substrate was milled, after which the holes were written into the substrate. Contrary to the hole-by-hole approach in E-beam lithography, the ion beam was continuously scanned over a whole template, slowly etching out all holes simultaneously. Simultaneously, the substrate was scanned with an electron beam to neutralize the charge build-up caused by implantation of gallium ions into the substrate. No post-writing development was necessary to obtain the functional structure.

Sample Cells and Crystal Growth

Sample cells for crystal growth were made by sawing the bottom off Chromacol

106

2-SV chromatography vials and gluing the substrates to the bottom using Araldit AW2101 epoxy glue with HW2951 hardener. The E-beam substrates were subsequently treated with a solution of polyhydroxystearic acid in dodecane (Acros, >99%) for 90 seconds up to several hours to prevent the sticking of particles to the substrate. The FIB substrates were treated for 5 minutes with a solution of 7.5 wt% potassium hydroxide (Merck, p.a.) in a mixture of ethanol (Merck, absolute p.a.) and 7.5 wt% water (Millipore, >18MΩ·cm) called PEW solution.

Suspensions of PMMA particles with a diameter of 900 nm and 1200 nm in cis-decahydronaphthalene (cis-decalin, Merck, "for synthesis") were added to the sample cells in aliquots of 0.2 to 1.0 mL. Particle concentration ranged from 0.34 to 40 v%. On a few occasions, a mixture (TTC) of tetrachloromethane (Merck, "for spectroscopy"), (1,2,3,4)-tetrahydronaphthalene (tetralin, Acros, 98+%) and cis-decalin in a volume ratio of 0.35:0.3:0.3 was used to density match the colloids.

Typically, suspensions were left to sediment for 40 hours before imaging the resulting structures.

Data Analysis

Confocal images were recorded using a Nikon Eclipse TE2000U inverted microscope with a Nikon C1 confocal scan head. A Spectra Physics 163C air cooled ion laser operating at a wavelength of 488 nm was used for illumination.

From the obtained images, particles were detected and analyzed using analysis software written for interactive data language (IDL).[23] For imaging the local crystal structure, the program Ballviewer was used.[24]

8.3   RESULTS & DISCUSSION

8.3.1   Template optimization

Figure 8.2a-c show schematics of templates of the various kinds used in this study. Figure 8.2d-f contain images of the experimental realizations of these templates. Panels d and e are confocal images obtained by removing excitation filters from the confocal to get signal from scattered laser light. Both templates were created with e-beam lithography. Figure 8.2f is an SEM image recorded in the FIB setup just after writing. Results on the incorporation of defects will be presented in section 8.3.2. First, the properties of the templates and the results of the writing process will be discussed.

The template shown in figure 8.2d is one of the templates used for testing of the nucleation hypothesis presented in chapter 7. These will be labeled hexagonal templates throughout the chapter. The defect in this image is wider than the mismatch created by growing a B and a C layer towards each other, as in figure 8.1a. Such templates were used as well, but in this case, a wider defect of 1.35*d*
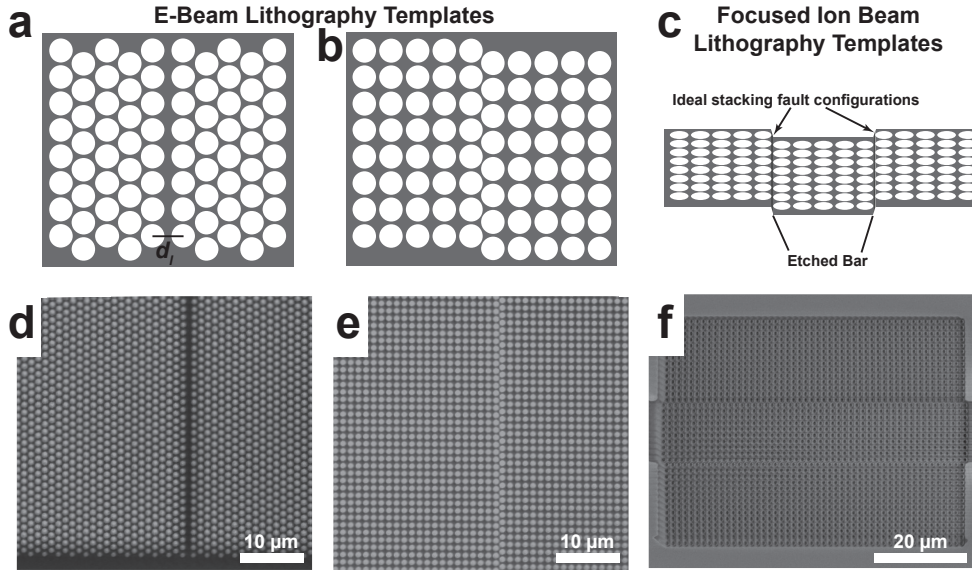
Figure 8.2. (a)-(c) Structures of the templates used in this chapter. (d)-(f) Experimental realizations of the structures shown in (a)-(c).

was created to accommodate a larger height difference for sedimenting particles, as illustrated in the bottom part of figure 8.1a. This larger height difference was chosen to exactly match the height step of $d\sqrt{6}/9$ that exists across the slanted stacking faults discussed in chapter 7. For the particles of 1200 nm diameter used here, this increases gravitational energy difference between a normal position and a position in the defect from 0.12 $k_B T$ to 0.19 $k_B T$ per particle.

The template in figure 8.2b and 8.2e is analogous to the hexagonal template in that it consists of a perfect crystallographic plane with a single defect line in it. The crystallographic plane is {100} in this case, as can be deduced from the characteristic square configuration of the holes. The difference with the hexagonal template is the uniqueness of the {100} plane to the fcc structure. The hexagonal template may contain stacking disorder in the growth direction, leading to a closure of the defect, as discussed in chapter 7. Contrary to this, crystal growth onto a {100} plane results in a unique growth of the fcc structure[21] and therefore a more likely persistence of the defect. In addition, the orientation of {111} planes in a crystal grown onto a {100} template is such that the inclusion of multiple intrinsic stacking faults may lead to their intergrowth, forming line defects parallel to the substrate, enabling detailed studies of such reactions on an "atomic" level and possibly leading to the creation of optical channels in self-assembled photonic crystals.

Like in the hexagonal templates, the line defect on the {100} plane is a projection

of an intrinsic stacking fault on a plane. This is symmetric and the direction of growth of the stacking fault is therefore not predetermined. Creating dislocation reactions on such templates is governed by chance, as faults can grow in two directions. For this reason, the third type of template was created, shown in figure 8.2c and 8.2f. This is again a {100} template, but here the defect lines contain a height step in the substrate, replicating the exact configuration of an intrinsic stacking fault as it exists in an fcc crystal. In the configuration illustrated in figure 8.2c, with a lower region between two faults, the two formed stacking faults will grow towards each other and react upon meeting. Such templates were created using an FIB setup, as this enables the milling of a substrate to introduce the required height step in a template.

Templates, both from e-beam and FIB lithography, could not be used as-produced. In the case of e-beam lithography, the spin-coated PMMA layer contained the template structure and thus served as the substrate onto which particles sedimented. When the templates were used as-produced, the sedimenting particles stuck to the substrate and did not have time to rearrange to their desired positions. An example of this is given in figure 8.3a, which contains a flat {100} template. Some particle have found their template directed position, but most of the substrate shows particles in a disordered arrangement. Measurements over time revealed that these particles were immobilized, even if the suspension above the substrate was dilute. The particles, like the substrate, consist of PMMA. These are stabilized by a layer of poly-hydroxystearic acid (PHSA) to prevent aggregation by steric stabilization.[25] The same polymer was used to cover the templates to prevent particle sticking,[26] as described in the experimental section. Figure 8.3b is an image of particles sedimented onto a substrate that was treated with PHSA for 90 seconds. The effect is clear, but the coverage is still incomplete. In figure 8.3c the substrate was treated for several hours and it is clear that this has the desired effect; particles follow the template-induced structure and form an almost perfect {100} plane. All e-beam generated substrates presented in this chapter were therefore treated with PHSA before applying particles.

The templates created with FIB lithography suffered from an entirely different problem. Figure 8.3d shows an as-produced template onto which particles were sedimented. Particles can be seen around the template and in the template edges, but not in the middle of the template. Figure 8.3e is a confocal image recorded 5 μm above the same template. This region is clear of particles as well. Only at 10 μm above the substrate (not shown) particles could be found directly over the template, although concentration was still lower than in the bulk. This effect is attributed to substrate charging due to ion implantation.

Already during template production, charging was found to be a problem. Although ITO covered slides were used to prevent charging, the ITO layer was
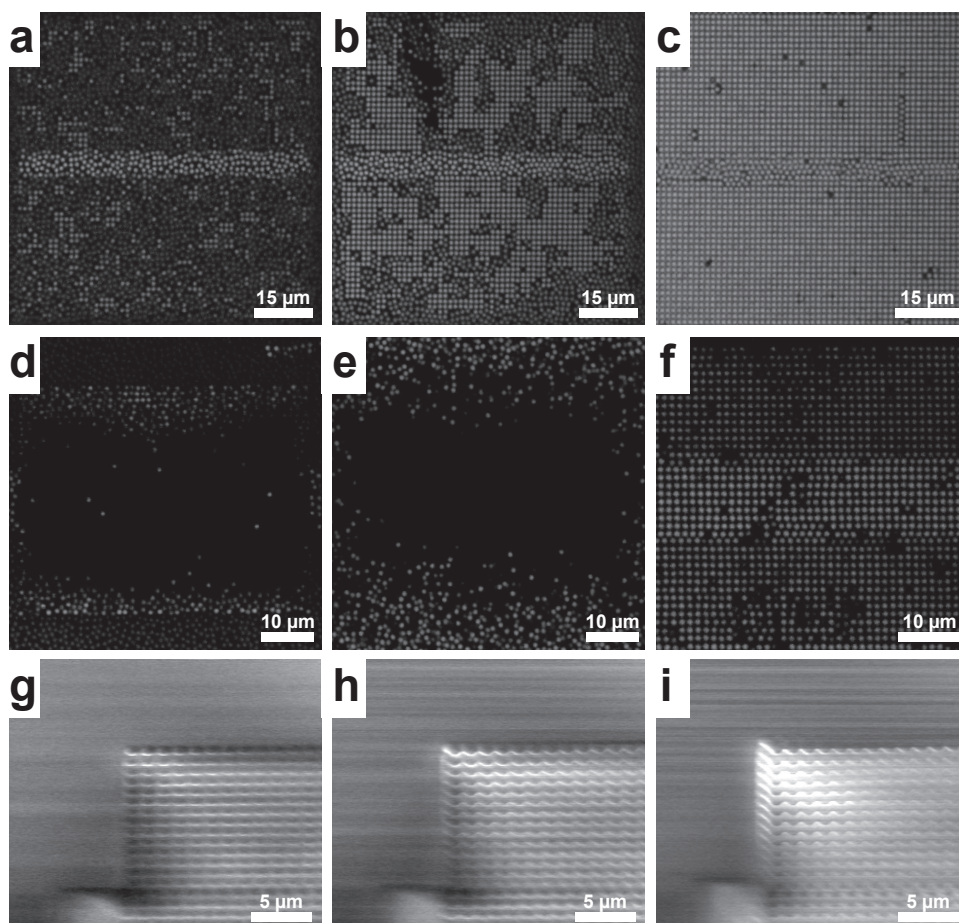
Figure 8.3. (a)-(c) Confocal images of particles sedimented on {100} templates with different degrees of PHSA coating. From left to right, particle sticking is drastically reduced. Panels (d) and (e) show confocal images of particles on and above an FIB substrate before treatment with PEW solution. Particles are repelled from the template area due to substrate charging. Panel (f) shows the template after treatment with PEW solution. Panels (g)-(i) show a template during various stages of ion beam milling. From left to right, the drift during milling is clear.

thin enough to be milled away early in the process. Continued milling caused a deposition of positively charged gallium ions in the substrate, deflecting the milling beam and resulting in a distortion of the template. This process is shown in figure 8.3g-i. From left to right, the template can be seen to distort more and more as milling proceeds. The pictures are SEM images taken during milling, which explains the high level of noise. A solution for the charging was found in using a high electron current and imaging continuously during milling. The incoming electrons neutralized the positive charge enough to produce suitable templates for
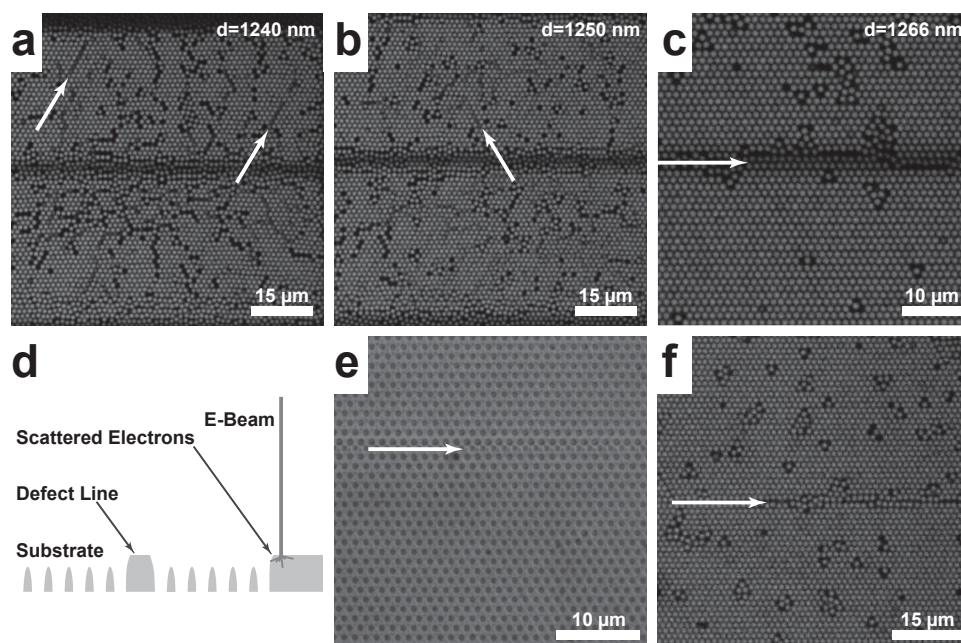
110

Figure 8.4. (a)-(c) Templates with different spacings. In (a) and (b), the template spacing is too small to fit the crystal and several defects are formed. In (c) the template perfectly fits the crystal spacing, but a dark line in the middle, indicated by the arrow, remains. This is a height step caused by a reduction of the amount of scattered electrons in this area, as illustrated in (d). Panel (e) shows an additional line of holes used to remove the height step. In (f) a crystal grown on the substrate shows that the height step is indeed removed.

crystal growth. Yet apparently, some charge was left in the templates, leading to a repulsion of the PMMA particles from the template. The long range of the repulsion can be explained by the low dielectric constant of cis-decalin, increasing the Debye length to many times the particle diameter.[27] By immersing the substrates into a solution of potassium hydroxide in a mixture of water and ethanol (PEW solution) for 5 minutes, the charge was found to be removed and particles nicely followed the imposed structure as shown in figure 8.3f.

To create optimum crystal growth conditions, a template has to fit the lattice spacing perfectly. If the periodicity of a template is slightly different from the ideal lattice spacing, strain builds up in the crystal.[22, 28] For crystals thicker than a few layers, this is released through the growth of misfit dislocations.[28] The optimum lattice spacing for the particles used in this study was found to be 1266 nm, which is approximately 6% larger than the particle size.[22] A range of smaller and larger spacings were also generated and did not produce satisfactory results, as shown for smaller spacings in figures 8.4a and 8.4b. Although most of the particles do form a hexagonal structure as dictated by the template, the crystal periodicity is

111

slightly larger than in the template. This is reflected by empty rows between small crystalline areas. Particles can be seen to be lying on top of the defect, unable to fit in due to the periodicity mismatch. Several of these defects are indicated by the arrows in figures 8.4a and 8.4b. The template in figure 8.4c has the ideal spacing of 1266 nm and does not show such defects.

One defect common to all templates shown in figure 8.4a-c is the horizontal dark line in the middle of the template, indicated by the arrow in figure 8.4c. This is a result of the scattering of electrons in the PMMA layer. The longer the e-beam remains focused on a single spot in the substrate, the larger the area of resist that is damaged and removed after development. This mechanism can be used to tune the size of the holes in the template. If the hole size is chosen to be large, the top layer of the resist is removed completely, leaving the template positioned slightly lower than the rest of the substrate. In the defect line, less holes are drilled, and therefore less material is removed from the substrate. A side view of a resulting template is shown schematically in figure 8.4d. Particles sedimenting on the defect region do not lie at the same level as the particles on the rest of the template and therefore do not form an ideal structure. To solve this problem, an additional line of holes was written in the defect line (arrow in figure 8.4e). The electron dose was much lower than used for the rest of the template, to prevent particles from preferably sedimenting into these positions. The extra hole line did remove the height step and resulted in crystal growth as shown in figure 8.4f. The arrow indicates the defect region, which is positioned at the same height as the rest of the template.

8.3.2   Resulting Crystal Structures
Hexagonal Templates

Crystal growth on hexagonal templates did not produce slanted faults on every attempt. Depending on the exact growth conditions and on chance, the defects were either closed in the first few layers above the template, or slanted faults were formed that persisted for many layers. For PMMA particles of 1200 nm diameter in cis-decalin, persisting defects were formed in approximately 50% of the crystals. Examples of this are given in figure 8.5. Figure 8.5a shows a confocal slice through the first layer of particles in a template. The defect line is indicated by the arrow. Although the slice was taken through the first layer of particles, a row of particles can be seen in the defect, indicating that these particles have sedimented below the level of the second layer, as assumed in the nucleation model of chapter 7. A cross-section of the same crystal along the plane perpendicular to the defect is shown in figure 8.5b. The direction of gravity in this picture is indicated by the arrow to the left. The arrow in the middle of the image points to the row of particles that have sedimented into the defect. These are clearly positioned below the other particles in the second layer.
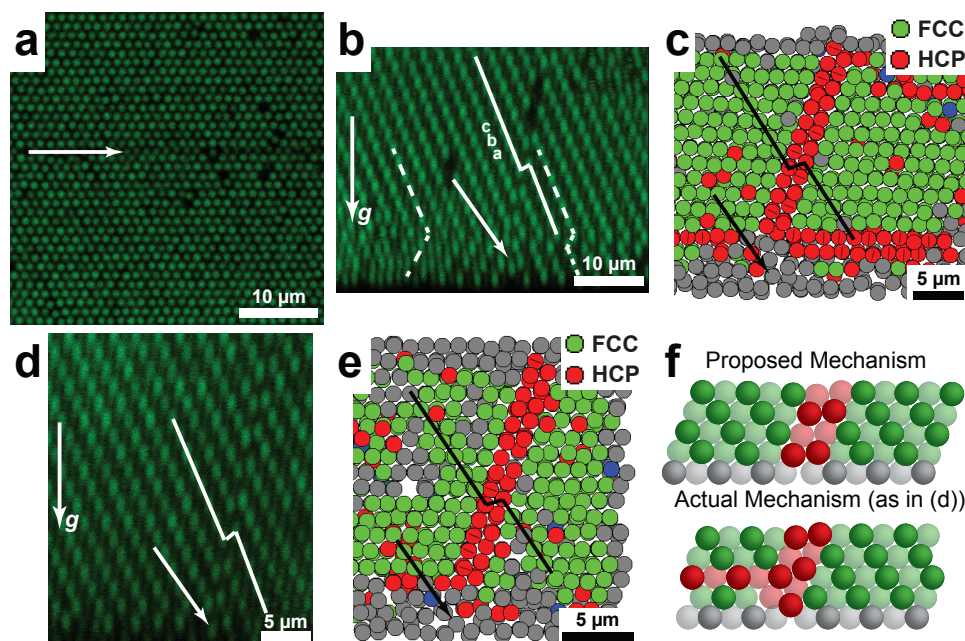
Figure 8.5. Panel (a) shows the defect line in hexagonal crystal layer. The particles that have sedimented into it are highlighted by the arrow. Panels (b) and (c) show a confocal image and a ballviewer reconstruction of a single crystal into which a stacking fault has been incorporated. Panels (d) and (e) show a different crystal, where a stacking fault is grown through a slightly different mechanism. In (f), a schematic of the stacking fault growth mechanism proposed in chapter 7 is shown, as well as the mechanism as it was grown in (d).

When the structure higher in the crystal is investigated, the fcc structure is apparent from the rows of particles in ABC stacking. This is highlighted by the drawn white line. The kink in this line is where the slanted stacking fault is grown into the structure. This is clarified in figure 8.5c, that contains a Ballviewer[24] image made of the detected particle coordinates from a 3D confocal dataset of the crystal. The view is the same as in figure 8.5b, but now, green particles have been detected as fcc and red particles as hcp. Here, the top part of the crystal can be seen to be fully fcc, with the slanted stacking fault running through it in red. These images are representative of the 50% of the structures containing such faults on these templates, grown at low particle volume fraction; highly perfect fcc crystals with slanted stacking faults originating from the substrate. The nucleation mechanism, however, does not correspond to the mechanism that was proposed in chapter 7. The bottom layers in figure 8.5b do not form an fcc structure from the start, as indicated by the dashed lines. This can also be seen in figure 8.5c, where the bottom layers have no determined crystal structure. In most crystals formed on hexagonal templates, this was a recurring problem. The first layer perfectly

113
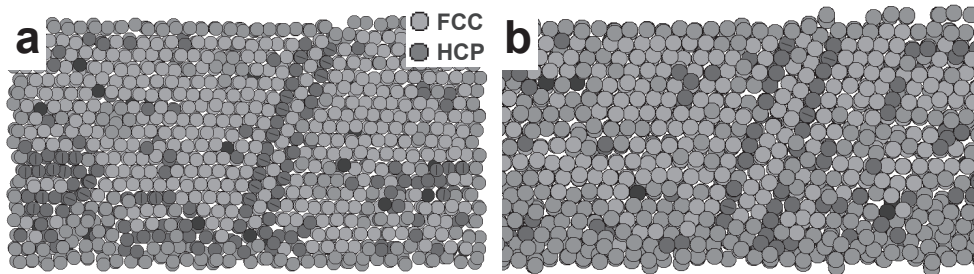
Figure 8.6. Panels (a) and (b) show different realizations of stacking faults on hexagonal templates, indicating that crystal growth is not governed by a single, unique mechanism.

followed the template structure, as in figure 8.5a, but the second and third layers were often much less crystalline. Still, the height step introduced at the template often produced the slanted stacking fault higher in the crystal.

Another example of a crystal grown on a hexagonal template is shown in figure 8.5d and 8.5e. Again, the arrow indicates a particle lying in the defect line and the white line indicates the fcc structure with slanted stacking fault. Here, the second layer was also less crystalline than the first layer on the template, but the crystal structure close to the substrate was more defined than in figure 8.5a-c. This dataset was therefore used to identify the mechanism of propagation of the fault and of the height step through the less-ordered region. Figure 8.5f displays the mechanism as identified in chapter 7 and the structure observed in figure 8.5d. The main difference between the two mechanisms is the number of particles in the slanted defect layers. From the first to the fifth layer, the first mechanism contains four particles from the substrate to the top, while the second mechanisms has five. Also, the right hcp layer is the one originating from the defect line here, while in the first mechanism, the left hcp layer originates there. The right side of the crystal is identical in both mechanisms, but the left part of the crystal is twinned in the measured case, while it is perfect fcc in the proposed model. Stacking disorder in the first few layers was observed in all measurements and differed from crystal to crystal. The mechanism is therefore not universal, but the transmission of the height step, as showed in figure 8.5f, is universal and creates stacking faults higher in the crystal. The disorder in the first layers, however, may result in the growth of different types of slanted stacking faults. In addition to intrinsic stacking faults, extrinsic ones have also been observed, as well as two layers of hcp separated by two fcc layers (shown in figure 8.6a and 8.6b, respectively).
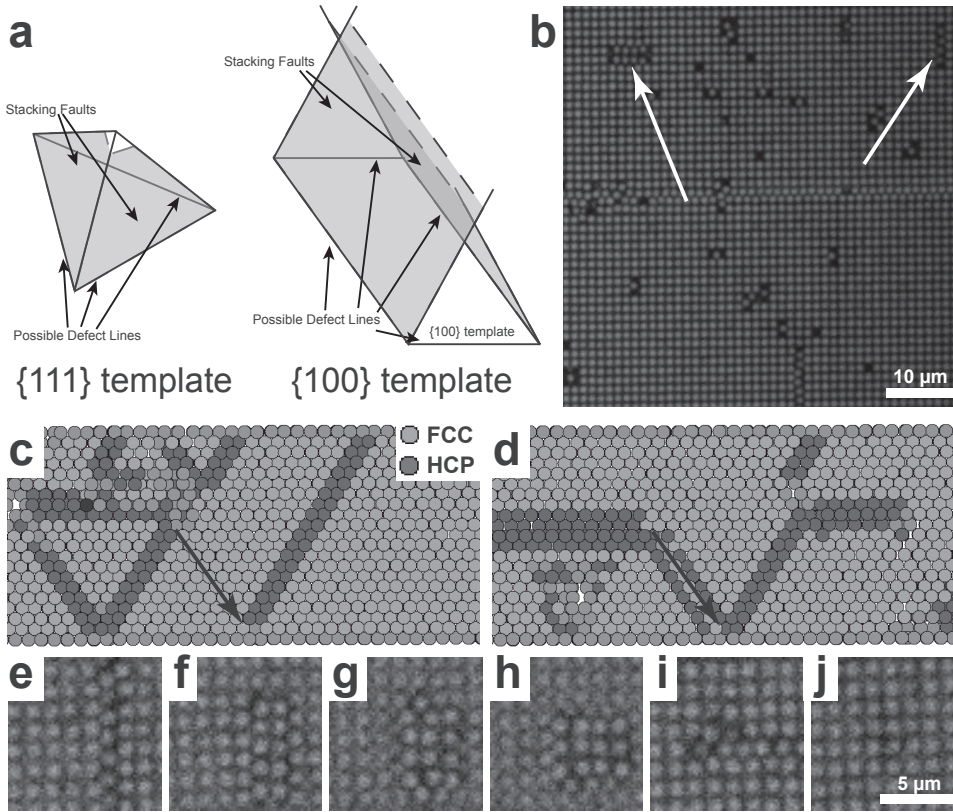
{100} Templates

Because of the different growth mechanisms for each crystal, the formation of different types of stacking faults and the 50% chance of incorporating a defect, the growth of slanted stacking faults on fcc {111} planes was found to be unsuitable

114

Figure 8.7. (a) schematically shows the orientation of slanted stacking faults on {111} and {100} planes, respectively. **(b)** shows the first layer of a crystal grown on a {100} template. The arrows indicate positions where the presence of vacancies has enabled the shifting of a row of particles by 1/4<110>. **(c)** and **(d)** show different realizations of crystal structures grown on top of {100} templates. The arrows indicate the position of the defect line. **(e)-(j)** show several confocal slices through a stacking fault tetrahedron. From left to right, the left and right edges of the fault can be seen to grow outward, while the top and bottom edges grow inward, until the fault closes in **(j)**.

for selective, reproducible incorporation of defects in colloidal crystals. A probable cause for the erratic behavior of the faults is the stacking disorder on the second and third crystal planes. As shown earlier, this stacking disorder does not prevent the inclusion of defects, but prevents the governing of defect growth by a single mechanism. To exclude the role of stacking disorder, {100} templates were produced. The fcc {100} plane is not degenerate like the {111} plane. Therefore, the only structure to grow on a {100} template is the fcc structure. Including a projection of a slanted intrinsic stacking fault in the template should also lead to defect growth in crystals grown on these templates. An additional advantage of growth on a {100} template is the orientation of the crystal {111} planes. When multiple defects are included in a template, the resulting stacking faults can grow

towards each other to react at a line parallel to the template, facilitating studies of the resulting structure. This is impossible on a hexagonal template, where the intersections of the slanted {111} planes with the template are oriented at 60° angles with respect to each other. For clarity, both structures are shown in Figure 8.7a.

The structure of the {100} templates that were used is shown in figures 8.2b and 8.2e. The first layer of a structure grown on such a template is shown in figure 8.7b. Most of the template is reproduced well, although a significant fraction of vacancies is present. Side-views of resulting structures are presented in figures 8.7c and 8.7d. In figure 8.7c, the defect region, indicated by the arrow, has produced an intrinsic stacking fault at the desired position. Contrary to the defects on hexagonal templates, the faults in these structures reproducibly grew on the right position due to the absence of stacking disorder.

A pair of faults similar to the one grown at the desired position can be seen to grow in the bottom left corner of figure 8.7c, from a region of the template that should produce a perfect crystal. Such structures have been observed before as the result of a non-ideal periodicity in the template.[14, 28, 29] This same effect could play a role here, although the faults seem to nucleate from regions where a vacancy has caused a row of particles to shift their position by half a lattice vector (arrows in figure 8.7b). From these rows of particles, two slanted stacking faults can grow outward, parallel to the row of shifted particles. From the ends of the defect line, slanted faults then grow inward, until they meet and close the defect, resulting in what is called a stacking fault tetrahedron (SFT).[13] Microscope images of several cross-sections of a single SFT are given in figure 8.7e-j. From left to right, the initial configuration of a vertical line of shifted particles can be seen to gradually change into a horizontal line of shifted particles, until the defect closes altogether in figure 8.7j. SFT's are commonly formed in fcc crystals with low stacking fault energy and it is therefore no surprise that they occur in colloidal crystals. For these structures to form, a high concentration of vacancies has to be present in a solid. Precipitation of these vacancies to form vacancy loops and the subsequent collapse of these loops results in the formation of Frank partial loops. These may finally collapse further to form SFT's.[13] In the crystals formed here, this mechanism is highly unlikely. The amount of vacancies required for SFT formation is roughly equal to the amount of particles in one of the planes of the tetrahedron. The frequency with which SFT's occur would require a vast amount of vacancies to be included in the crystals during growth. In addition, these vacancies would have to possess a high diffusivity to agglomerate into vacancy loops at the time scale of the experiments presented here. A more likely mechanism, especially for crystals grown from high Péclet number particles, grown in a layer-by-layer fashion,[30, 31] is the formation of a defect line such as in figure 8.7e. This can be created by a single vacancy, or by a trivacancy if two layers are involved. From such a defect, it may be favorable to
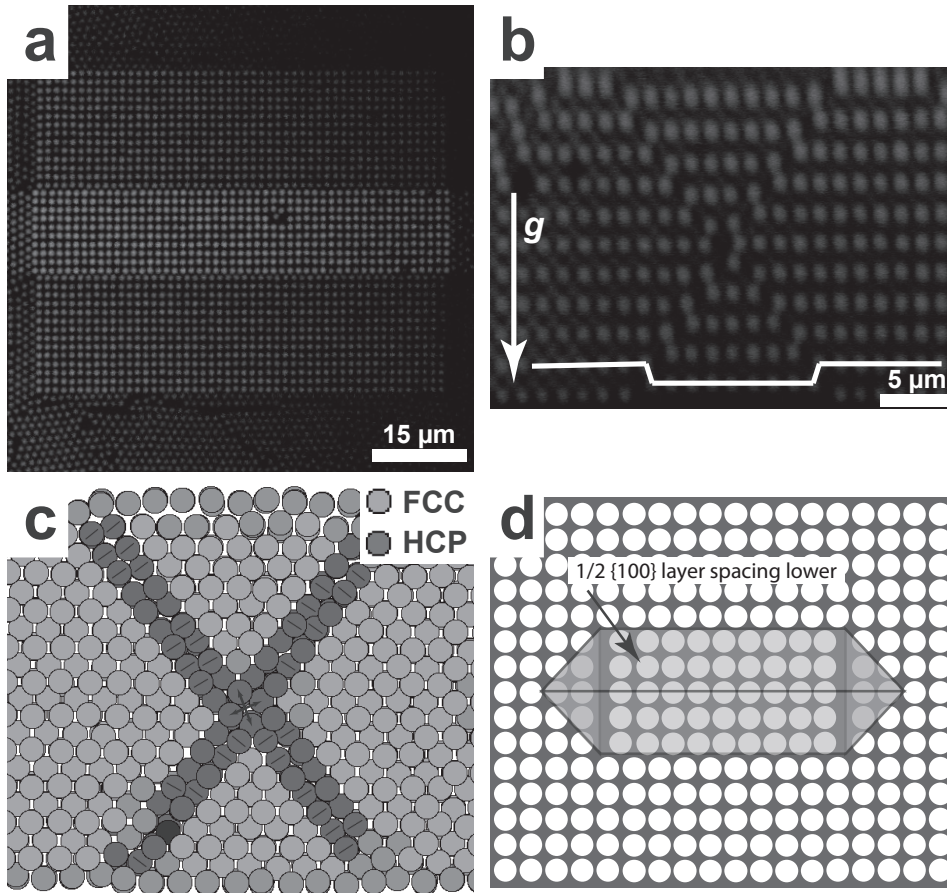
Figure 8.8. (a) Bottom layer of a crystal on an FIB template. The different intensities correspond to different particle heights. (b) Side view of the same crystal as in (a). Stacking faults grow from the bottom, through each other, to the top of the image. (c) Ballviewer image of the same crystal. The hcp layers can be seen to cross each other and continue through the crystal. Panel (d) shows the proposed template for the formation of stacking fault tetrahedra, resulting in a defect line of defined length at a predetermined height in the crystal.

grow a SFT layer-by-layer, as shown in figure 8.7e-j.

The defects that nucleated at the intended position at the defect line in the template also grew in two directions simultaneously (figure 8.7d). This is attributed to the symmetry of the template and the orientation of {111} planes in crystals grown on {100} templates. Line defects in a {100} template can produce stacking faults in two directions in a single fcc crystal. Contrary to this, line defects in hexagonal templates can produce stacking faults in two directions, but not within the same crystal, as different directions of stacking faults require different fcc twins.

Chapter 8: Defect Engineering in Colloidal Epitaxy

Focused Ion Beam {100} Templates

To solve this problem and to gain control over the growth direction of the defects, templates with height steps were fabricated. By milling away parts of a substrate and patterning the milled region as shown in figures 8.2c and 8.2f, a structure corresponding to a perfect intrinsic stacking fault can be created in the template. By including two such height steps in a mirrored configuration, a pair of stacking faults can be grown towards each other. Results of crystal growth on such a template are shown in figure 8.8. Figure 8.8a shows the first layer grown on a FIB-template. The template is located in the center part of the image, where the particles have assembled into a square configuration. This region is lighter than the remainder of the image, as the particles have sedimented into the template, resulting in a slightly different focal plane than the surrounding crystals. In the template area, an even brighter bar can be seen. This is the bar that has been etched away to allow part of the crystal to have a well-defined height difference with the rest of the structure, to produce perfect stacking faults.

A side view of the same crystal is shown in figure 8.8b. The arrow to the left indicates the direction of gravity and therefore points towards the template. From the template, two intrinsic stacking faults grow upwards, at the position of the kinks in the solid white line. Halfway through the image, these faults meet and interact to form a channel through the crystal. Above that, the stacking faults continue to grow upwards. The structure is illustrated more clearly in a Ballviewer[24] image of the crystal (figure 8.8c), where particles in the stacking faults are visualized in red. Here, the perfect fcc structure containing two crossing intrinsic stacking faults is instantly clear.

The formation of crossing faults is surprising, as the meeting of two stacking faults in fcc metals usually results in the formation of a stair-rod dislocation, ending the propagation of the stacking fault and instead leaving a distorted region of crystal. This discrepancy can be explained through the extremely small stacking fault energy in colloidal crystals. The energy of a stair-rod dislocation (a pure edge dislocation) roughly scales as

$$E_{SR} = \frac{\mu b^2}{4\pi(1-\nu)} \ln\left(\frac{e^2 R}{2w}\right) \tag{8.1}$$

where μ is the crystal shear modulus, b is the dislocation Burgers vector, e is the base of the natural logarithm, R is the size of the crystal and w is the dislocation core width. For a stair-rod dislocation, the stacking fault energy of the two bordering stacking faults also adds to this:

$$E_{SF,SR} = 2\gamma R \tag{8.2}$$

where γ is the stacking fault energy. Note that in both cases, the energy is given per unit length of dislocation. For a typical fcc metal, with a shear modulus of ~40

GPa[32] and an R of 250 particles (after which other dislocations distort the field of the first dislocation), E_{SR} is approximately 30 k_BT per lattice constant along the dislocation. Assuming a stacking fault energy of 0.1 J·m^{-2},[33] the contribution of the stacking faults to the energy is much larger than this, on the order of $2 \cdot 10^3$ k_BT per lattice constant. Similar calculations for a colloidal crystal, assuming a shear modulus of 1 Pa[34] and a stacking fault energy of 10^{-3} k_BT per particle[19], result in a total energy of ~10 k_BT for the full stair-rod configuration. Here, the stacking fault energy of ~0.5 k_BT makes up a minor part of the dislocation energy.

Contrary to the stair-rod configuration, the crossing faults configuration does not contain a dislocation, as a Burgers circuit drawn around the defect closes perfectly. The energy of this configuration consists of the stacking fault energy of the four stacking faults bordering the defect, and the energy needed to create the channel through the crystal. As the stacking fault contribution for a fault extending 250 particle diameters into the crystal was calculated to be ~10^3 k_BT per stacking fault in a metal, a configuration containing four stacking faults has a much higher energy than a stair-rod configuration, even without the penalty of breaking the bonds in the defect line. This additional term is mainly made up of the energy required to break the bonds between the particles indicated by the arrows in figure 8.8c. Per particle length of defect, two interparticle bonds are broken, which for typical fcc metals have bond strengths on the order of 10^2 k_BT per bond[35], adding only marginally to the total defect energy.
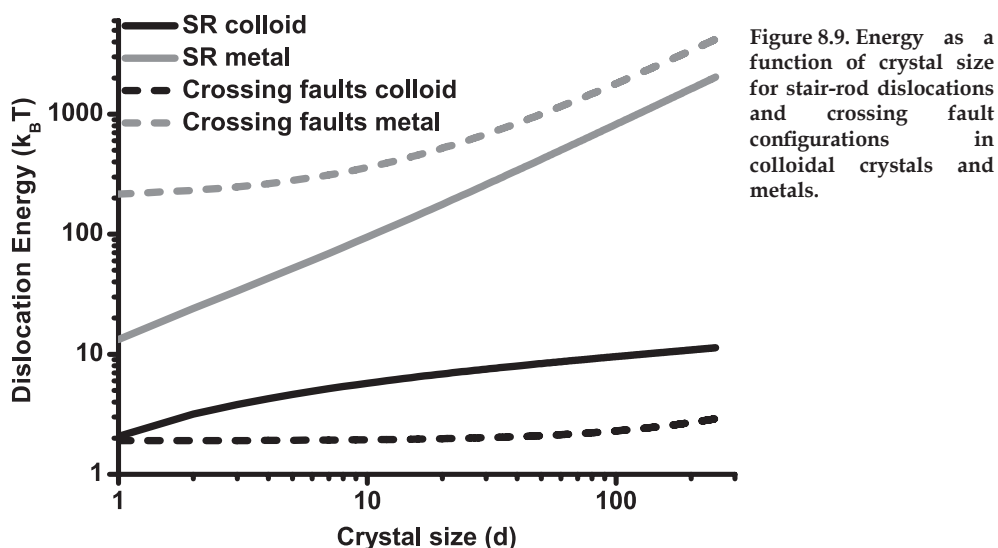
In the colloidal case, the four stacking faults extending 250 particle diameters contribute ~1 k_BT to the defect energy. The energy required for creating the additional 0.16 d^3 of volume in the defect, assuming a crystallization pressure of 11.7 k_BT·d^{-3},[34] is ~1.9 k_BT. Contrary to the metallic case, the energy of this configuration is smaller than for the stair-rod configuration, mainly attributable to the low stacking fault energy in colloidal crystals.

The dislocation energies for both metals and colloidal crystals are displayed in figure 8.9 as a function of crystal size. A sedimentary colloidal crystal is usually smaller than 250 particle diameters, but it can be seen here that the crossing faults configuration is more stable than the stair-rod configuration over the whole range of crystal sizes. The contrary can be seen to be true for metals. This shows that the crossing faults defect is possibly unique to colloidal crystals, although they may exist in fcc metals as metastable structures resulting from reactions between two stair-rod dislocations.

Contrary to the flat templates, the templates containing a height step produced the same stacking faults in each experiment. Stacking faults reproducibly grew into the same direction and crossed each other at the same height above the template. On most templates, some slanted faults still nucleated at other positions as a result of the presence of vacancies or due to a lattice mismatch, but on templates

Figure 8.9. Energy as a function of crystal size for stair-rod dislocations and crossing fault configurations in colloidal crystals and metals.

with a lattice constant of 1.09d, the resulting structures were almost defect-free. The resulting structures hold promise for the selective incorporation of defects in otherwise perfect colloidal photonic crystals. By infiltrating the fcc structure with a high refractive index material and etching out the colloids, crystals with a full photonic band gap can be obtained.[3, 4, 36] The intergrowth channels in the crossing faults structure can then function as propagation channels for light. One of the drawbacks of inverted fcc photonic crystals is their sensitivity to other types of disorder, that readily close their band gap. A solution for this problem in self-assembled colloidal systems is the use of templates that have been predicted to stabilize the Laves phases in binary mixtures of colloids.[8] The different components of these binary crystal structures are separately arranged on a diamond and a pyrochlore lattice, each of which possesses a larger and more robust band gap than the inverted fcc structure. Although the diamond and pyrochlore structures are more complex than the fcc structure, they also show a large degree of similarity. This includes their susceptibility to stacking disorder and formation of dislocations. As the growth of such structures has been predicted to occur only if induced by templates, these same templates can be modified to produce defects at desired positions, analogous to the templates used here.

Another promising direction where templates may be employed to incorporate faults is the use of patchy particles. Patchy particles constitute one of the most promising directions for creating self-assembled structures with, for example, the diamond structure. Through preferred oriented attachment patchy particles are able to generate non-close-packed structures that have more favorable optical properties than the close-packed structures that can be formed by purely repulsive

120

colloids. Again, templates may be employed to guide the particles into the desired structure.

Corners and T-junctions

To investigate further possibilities for influencing the defect structure and adding functionality, templates containing projections of corners and T-junctions were designed and tested using NVT Monte Carlo simulations. The simulations were not used to investigate the final equilibrium state of the crystals, but rather to provide rapid insights into the flaws and benefits of different template structures. For the design of the templates, use was made of the mechanism of formation of stacking fault tetrahedra that was observed earlier. Structures similar to the structure in figure 8.7f were designed with the aim of growing two faults towards each other along the defect line and two faults away from each other from the tips of the defect, as illustrated in figure 8.8d. To grow slanted faults towards each other along a defect line, as in the focused ion beam experiments described before, the ideal depth for the bar in the template is one third of the {100} interlayer spacing. To create the defects growing away from the tips of the line, the bar should ideally be placed one third of the interlayer spacing higher, or two thirds lower. As this is incompatible with the other defects, a compromise of one half was used. Also, for growing ideal stacking faults the lattice spacing across the defect should be slightly adapted, with the two parts of the crystal on the long sides of the defect slightly shifted towards each other. In the case of a SFT projection, however, a single fcc crystal surrounds the defect area and adjusting the spacing across the defect would affect the spacing in the fcc crystal. Therefore, the spacing across the defect in these templates was kept equal to the ideal lattice spacing in the rest of the crystal.

Figure 8.10 shows the structures resulting from sedimenting particles on a substrate with two SFT projections that were rotated by 90° with respect to each other. Figure 8.10a shows the template structure and a few of the particles that sedimented onto it (dark grey). Figure 8.10b shows a slice through the crystal a few layers above the template. An fcc structure has been formed and intrinsic stacking faults have been incorporated at the desired positions. In figures 8.10c and 8.10d the faults continue to grow towards each other until they intergrow in figure 8.10e, after which they continue to propagate through the structure (figure 8.10f). The red particles near the bottom and right edges of the image are due to the periodic boundary conditions used in the simulations and show the top and left sides of the SFT's, respectively. Similar results were obtained for T-junction templates, of which the structure is given in figure 8.10g. To demonstrate the reproducibility and versatility of the incorporation mechanism the template shown in figure 8.10h was designed. The displayed template was stitched together from three separate templates on which simulations were performed separately. Figure 8.10i shows
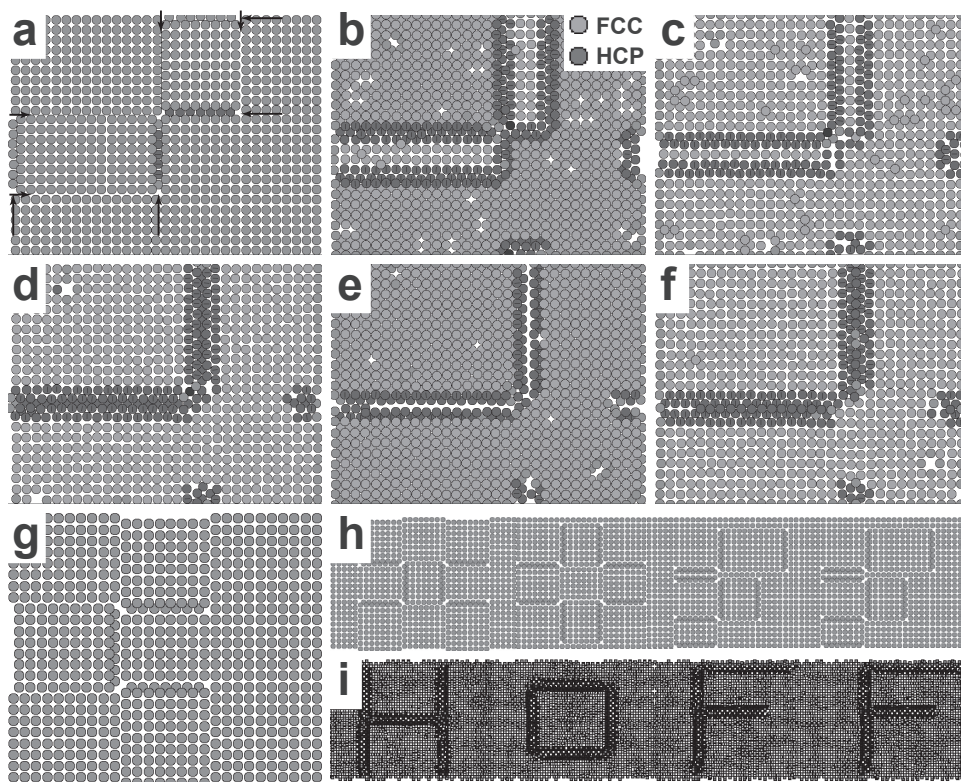
121

Figure 8.10. (a) Template used for simulations in which faults grow in a corner configuration. (b)-(f) Several slices through the resulting structure, showing the small channel through the crystal in (e). Panel (g) shows a template from which hollow T-junctions can be grown into a crystal. Panel (h) shows a template in which corners and t-junctions were combined. Panel (i) shows the structure grown onto this template in simulations, spelling HOFF.

the resulting structure, where HOFF (after Jacobus Henricus van 't Hoff) has been written at the height where the faults cross each other. The results from simulations are highly promising for further experiments in which the proposed templates are realized through FIB lithography.

8.4 SUMMARY AND CONCLUSIONS

Results were shown on the selective incorporation of slanted intrinsic stacking faults in sedimentary colloidal crystals. Crystal were grown on flat hexagonal and square templates containing 2D projections of slanted faults, as well as on square templates with height steps mimicking ideal stacking fault configurations. On all of these templates, stacking faults were grown at the desired positions, albeit with varying degrees of success. On the hexagonal templates, faults were formed

in approximately 50% of the crystals. The growth of defects was disturbed by disorder on the second and third crystal layers. Yet, the height difference induced by the template was often transferred to the growing crystal and induced the growth of defects there. This indicates that the crystals are very sensitive to small lattice distortions and that the stress caused by such distortions is readily relieved through the formation of stacking faults.

Square {100} templates were produced to improve the nucleation of faults at the desired position, as stacking faults parallel to the substrate are absent in such structures. Fault nucleation was markedly improved and always occurred on the desired position. Due to the symmetry of the template and the orientation of the lattice, two faults often nucleated from a single defect line. To prevent this, new templates including platforms of different height were produced using ion beam lithography. These mimicked the ideal structure of intrinsic stacking faults and reproducibly produced highly perfect fcc crystals with stacking faults with the right position and direction. Intergrowth of two such stacking faults resulted in small channels through the crystal at well-defined positions. Preliminary results from simulations showed the possibility of including corners and junctions in these channels by properly designing the templates.

The results presented in this chapter hold promise for the generation of functional photonic crystals. Although the fcc structure in itself does possess a full photonic band gap if the crystal is inverted, the results obtained here can also be viewed as a model for more complex structures. Among these are the sodium chloride structure[29], the binary Laves phases[8] and structures built from patchy particles.[10] All of these structures share their susceptibility to stacking disorder with the fcc structure and can therefore be modified using proper templating.

To fully explore the potential of the structures presented here, efforts to characterize the optical properties of such structures have to be made. The effects of the presence of a hollow channel may provide propagation channels through a photonic crystal, but the stacking faults bordering the defect may also cause losses. Therefore, both calculations as well as experiments have to be performed.

8.5   REFERENCES

[1] H. S. Sozuer, J. W. Haus, R. Inguva, *Phys. Rev. B,* **1992**, 45, 13962.

[2] K. Busch, S. John, *Phys. Rev. E,* **1998**, 58, 3896.

[3] J. E. G. J. Wijnhoven, W. L. Vos, *Science,* **1998**, 281, 802.

[4] A. Blanco, E. Chomski, S. Grabtchak, M. Ibisate, S. John, S. W. Leonard, C. Lopez, F. Meseguer, H. Miguez, J. P. Mondia, G. A. Ozin, O. Toader, H. M. Van Driel, *Nature,* **2000**, 405, 437.

[5] V. Yannopapas, N. Stefanou, A. Modinos, *Phys. Rev. Lett.,* **2001**, 86, 4811.

[6] Z. L. Wang, C. T. Chan, W. Y. Zhang, Z. Chen, N. B. Ming, P. Sheng, *Phys. Rev. E,* **2003**, 67, 016612.

[7] M. Maldovan, C. K. Ullal, W. C. Carter, E. L. Thomas, *Nature Mater.,* **2003**, 2, 664.

[8] A. Hynninen, J. H. J. Thijssen, E. C. M. Vermolen, M. Dijkstra, A. Van Blaaderen, *Nature Mater.,* **2007**, 6, 202.

[9] Z. L. Zhang, A. S. Keys, T. Chen, S. C. Glotzer, *Langmuir,* **2005**, 21, 11547.

[10] S. C. Glotzer, M. J. Solomon, *Nature Mater.,* **2007**, 6, 557.

[11] V. C. Martelozzo, A. B. Schofield, W. C. K. Poon, P. N. Pusey, *Phys. Rev. E,* **2002**, 66, 021408.

[12] S. Pronk, D. Frenkel, *J. Chem. Phys.,* **2004**, 120, 6764.

[13] D. Hull, D. J. Bacon, Introduction to Dislocations, fourth edn., Elsevier Ltd., Oxford**, 2001**.

[14] W. Lee, A. Chan, M. A. Bevan, J. A. Lewis, P. V. Braun, *Langmuir,* **2004**, 20, 5262.

[15] A. J. C. Wilson, *Proc. Roy. Soc. London, Ser. A,* **1942**, 180, 277.

[16] O. S. Edwards, H. Lipson, *Proc. Roy. Soc. London, Ser. A,* **1942**, 180, 0268.

[17] P. N. Pusey, W. Van Megen, P. Bartlett, B. J. Ackerson, J. G. Rarity, S. M. Underwood, *Phys. Rev. Lett.,* **1989**, 63, 2653.

[18] J. Zhu, M. Li, R. Rogers, W. Meyer, R. H. Ottewill, STS-73 Space Shuttle Crew, W. B. Russel, P. M. Chaikin, *Nature,* **1997**, 387, 883.

[19] S. C. Mau, D. A. Huse, *Phys. Rev. E,* **1999**, 59, 4396.

[20] J. P. Hoogenboom, D. Derks, P. Vergeer, A. van Blaaderen, *J. Chem. Phys.,* **2002**, 117, 11320.

[21] A. van Blaaderen, R. Ruel, P. Wiltzius, *Nature,* **1997**, 385, 321.

[22] J. P. Hoogenboom, A. K. van Langen-Suurling, J. Romijn, A. van Blaaderen, *Phys. Rev. E,* **2004**, 69, 051602.

[23] J. C. Crocker, D. G. Grier, *J. Colloid Interf. Sci.,* **1996**, 179, 298.

[24] G. J. Ackland, A. P. Jones, *Phys. Rev. B,* **2006**, 73, 054104.

[25] G. Bosma, C. Pathmamanoharan, E. H. A. de Hoog, W. K. Kegel, A. van Blaaderen, H. N. W. Lekkerkerker, *J. Colloid Interf. Sci.,* **2002**, 245, 292.

[26] E. C. M. Vermolen, Ph.D. Thesis, Utrecht University, **2008.**

[27] A. Yethiraj, A. van Blaaderen, *Nature,* **2003**, 421, 513.

[28] P. Schall, I. Cohen, D. A. Weitz, F. Spaepen, *Science,* **2004**, 305, 1944.

[29] E. C. M. Vermolen, A. Kuijk, L. C. Filion, M. Hermes, J. H. J. Thijssen, M. Dijkstra, A. van Blaaderen, *P. Natl. Acad. Sci. USA,* **2009**, 106, 16063.

[30] M. Marechal, M. Hermes, M. Dijkstra, *J. Chem. Phys.,* **2011**, 135, 034510.

[31] T. Biben, R. Ohnesorge, H. Lowen, *Europhys. Lett.,* **1994**, 28, 665.

[32] H. P. R. Frederikse, in CRC Handbook of Chemistry and Physics, 88th edn. (Ed: D. R. Lide), Taylor & Francis Group, Boca Raton **2008**, 12-33.

[33] H. Van Swygenhoven, P. M. Derlet, A. G. Froseth, *Nature Mater.,* **2004**, 3, 399.

[34] D. Frenkel, A. J. C. Ladd, *Phys. Rev. Lett.,* **1987**, 59, 1169.

[35] Y. R. Luo, in CRC Handbook of Chemistry and Physics, 88th edn. (Ed: D. R. Lide), Taylor & Francis Group, Boca Raton **2008**, 9-56.

[36] Y. A. Vlasov, X. Z. Bo, J. C. Sturm, D. J. Norris, *Nature,* **2001**, 414, 289.

Summary

Like all atomic crystals, crystals built from sub-micrometer sized building blocks through self-organization always possess a certain degree of disorder. Extensive research has been devoted to controlling defects in atomic crystals by influencing their growth conditions and through post-processing. In colloid science, studies on defects are in their infancy. On the one hand, knowledge about defects can contribute to the optimization of the colloidal crystal structure, perfecting their optical properties. On the other hand, colloids can also serve as a model system for atomic materials, filling gaps that are still present in our understanding of defect behavior in these materials. This thesis is devoted to the identification of crystalline defects in colloidal crystals, study their behavior, and influence their growth.

In **chapter 2** synchrotron X-ray diffraction experiments are performed on silica colloidal crystals in cyclohexane. In particular, the effect of multiple diffraction on the intensity of streaks of diffuse scattering called Bragg rods is discussed. The intensity of these rods mainly stems from stacking disorder in crystals, enabling the determination of crystal stacking sequences through measuring intensity profiles of these rods. To be able to fully quantify the rod profiles, it is important to know what other effects contribute to their intensity. By investigating the same Bragg rods at different photon energies it could be deduced that the presence of Bragg rods at forbidden positions in q-space is caused by multiple diffraction. However, compared to the intensity of allowed rods, which are normally used to determine stacking disorder, the intensity of multiple diffraction is found not to be significant.

Chapter 3 discusses the presence of significant amounts of stacking disorder in convectively assembled colloidal crystals. The high refractive index contrast between particles and their surroundings in these crystals makes light microscopy studies on their structure very hard. Their internal structure has been discussed manifold on the basis of scanning electron microscopy images, looking at cuts through crystals and discussing stacking disorder parallel to the substrate. In this chapter, X-ray diffraction is used to investigate the crystal structure in other directions through the interpretation of scattering profiles along Bragg rods. Approximately 10% of stacking disorder in the form of intrinsic stacking faults is found to occur in two out of the three <111> directions that are not perpendicular to the substrate.

Although confocal microscopy is a frequently used tool to investigate the internal structure of colloidal crystals in dispersion, dried crystals obtained by convective assembly cannot be characterized with this technique. The scattering of light from the building blocks prevents real-space investigations into their internal structure. In **chapters 4 and 5** the possibility of using scanning transmission X-ray microscopy

to study the internal structure of such structures is discussed. In **chapter 4** a two dimensional study is made of thin colloidal crystals. The transmission properties of several materials at different X-ray energies are discussed. It is shown that in crystals of polystyrene spheres of 200 nm diameter the crystal structure can be determined with single particle accuracy for structures of three layers thick. For silica crystals of particles of 500 nm in diameter, it is shown that crystal thicknesses can be accurately determined up to 10 layers through an optical density image, although local structures cannot be determined by 2D measurements. **Chapter 5** focuses on studies on the internal structure of silica colloidal crystals. Here, tomography is used to obtain information on the full 3D structure of such crystals on a single particle level. To this end 41 images of the same piece of crystal were taken under different angles. The tomographic reconstruction yielded information on vacancies and stacking faults, as well as lattice deformations.

Chapter 6** contains an in-depth study of single dislocations in colloidal crystals of thermosensitive particles. Thermosensitivity is a way to gain better control over particle crystallization and can be employed to remove dislocations from a crystal through annealing. To investigate the behavior of dislocations in detail during crystal heating, their behavior is investigated as function of temperature using confocal microscopy. The observed behavior is found to be counterintuitive, showing a reduction in dislocation size and therefore a strengthening of the crystal and a reduction in dislocation mobility upon heating. This is found to be caused by a shrinking and consequent hardening of the particles, while the particle volume fraction remained approximately constant due to a gravitational compression of the crystal. Dislocation behavior could be qualitatively explained by existing theory and showed promise for direct measurements of crystal shear strength as function of dislocation profile.

The last two chapters focus on the role of dislocations and stacking faults during crystal growth. **Chapter 7** discusses the growth of slanted stacking faults into sedimentary colloidal crystals. Their nucleation mechanism and their influence on the final crystal structure are discussed. Indications were found that the presence of these faults during crystal growth causes a favored fcc growth, but a thermodynamic driving force could not be excluded. In **chapter 8** the nucleation mechanism of these faults is used to grow them at predetermined positions into crystals by using growth templates. The use of different types of templates resulted in crystals with different orientations and different fault structures. The best results were obtained when height steps could be integrated into the templates to perfectly mimic the structure of a stacking fault. Using these templates, the direction of the faults could be controlled and intergrowth structures could be produced, resulting in small hollow channels running through a crystal.

Samenvatting in het Nederlands

Dit proefschrift beschrijft de studie van roosterfouten in colloïdale kristallen. Als ik na deze eerste zin verder zou gaan met een beschrijving van het effect van dislocaties op de fotonische eigenschappen van epitaxiaal gegroeide vlakgecentreerd kubische structuren, zou ik deze samenvatting in het Nederlands net zo goed niet kunnen schrijven. De beoogde lezers van dit hoofdstuk zouden na het lezen van "dislocaties" of "fotonische" zijn afgehaakt, waarna het niet meer zou uitmaken of ik dit hoofdstuk zou vullen met een samengevatte inhoud van mijn proefschrift of met een verhandeling over de Zuid-Chinese baardmijt. Om deze reden wil ik terugschakelen naar de openingszin en beginnen met een verduidelijking van de begrippen "roosterfout", "colloïdaal" en het meer bekende begrip "kristal", om dan in het tweede deel van deze samenvatting meer de diepte in te gaan.

Hoewel het woord kristal misschien bekend klinkt vanwege het gebruik van kristallen wijnglazen of andere kristallen gebruiksvoorwerpen is dit nu net een geval waar de wetenschappelijke term kristal niet op zijn plaats is. Technisch gesproken is het correcter om aan de dinertafel het bestek, het porselein of het keukenzout aan te duiden met de term kristal, al zullen uw tafelgenoten hier wellicht raar van opkijken. Dit heeft alles te maken met de structuur van deze producten op de allerkleinste schaal. Op dit niveau bestaan alle materialen uit atomen: kleine balletjes die de bouwstenen zijn van alle materialen. Kijken we naar de atomen waar een materiaal uit opgebouwd is dan ziet kristalglas eruit als de ballenbak bij de Ikea: de atomen liggen dwars door elkaar zonder enige ordening. Als we nu naar het bestek kijken, ervan uitgaande dat er metalen bestek op tafel ligt, dan zullen we zien dat alle atomen daar netjes gerangschikt zijn, zoals sinaasappels bij een nette marktkoopman. Dit is karakteristiek voor een kristal. Volgens de definitie is een kristal een regelmatige, repeterende structuur in drie dimensies.
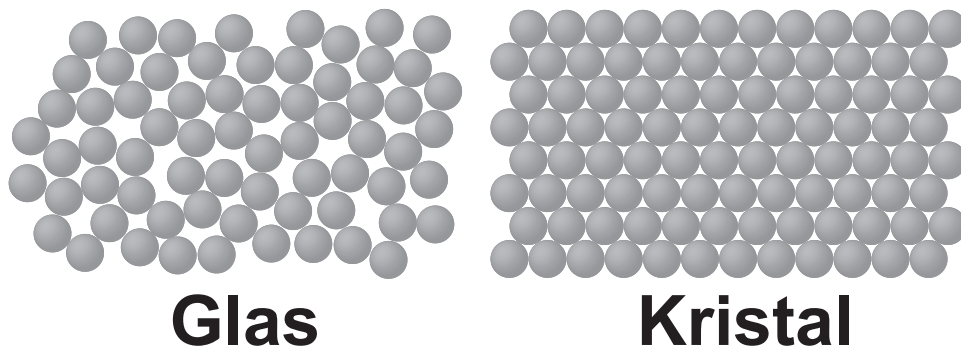

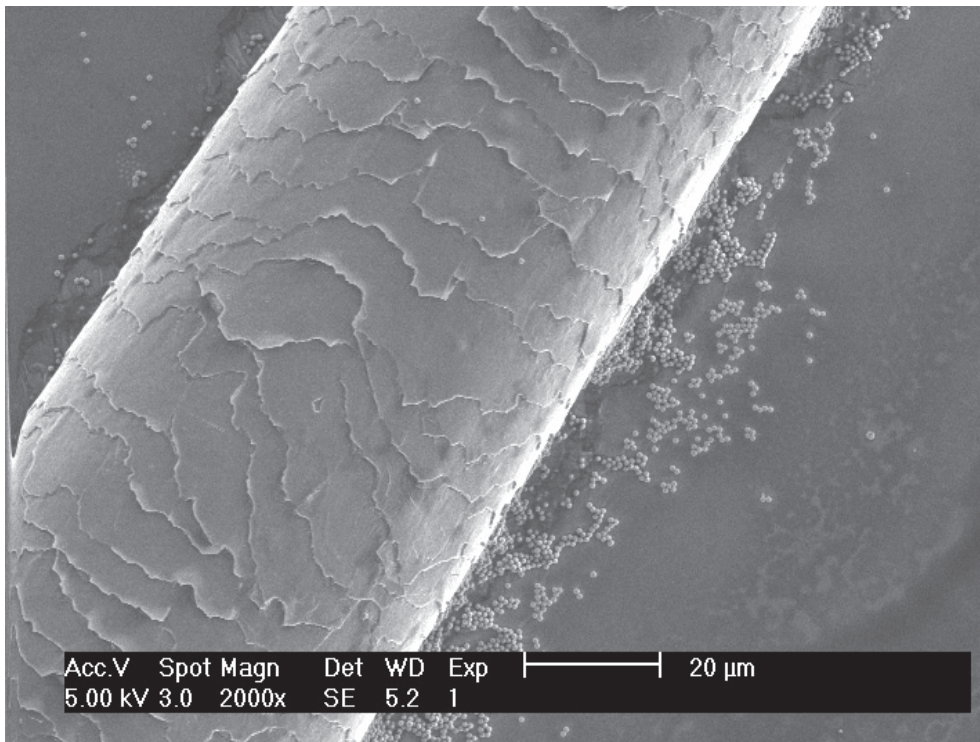Figure 10.1. Schematische weergave van de structuren van een glas en een kristal.

Figure 10.2. Elektronenmicroscopische opname van een menselijke haar met daarnaast bolvormige colloïden van ca. 1 micrometer doorsnee. Opname: B. Erné

Voor de sinaasappels betekent dit dat we, zodra we de eerste sinaasappels hebben liggen, in principe van tevoren kunnen uitrekenen waar alle volgende sinaasappels geplaatst zullen worden. De ongeordende structuur van een glas en de geordende kristalstructuur zijn geïllustreerd in figuur 10.1.

Metalen zijn dus kristallijne stoffen met als bouwstenen atomen. Als we in dezelfde lijn over de stepels sinaasappels op de markt denken, kunnen we deze "sinaasappelkristallen" noemen. In het geval van colloïdale kristallen zijn de bouwstenen colloïden. Volgens de officiële definitie zijn dit deeltjes die in grootte tussen de 1 en 1000 nanometer groot zijn, waarbij de deeltjes in dit proefschrift tegen de bovengrens van 1000 nanometer aanzitten. Of, om het in sinaasappels uit te drukken: 100000 keer zo klein als een sinaasappel. Hoewel dit klein klinkt is dit nog altijd 10000 keer zo groot als een atoom. Aangezien dit allemaal getallen zijn die vrij weinig zeggen is figuur 10.2 toegevoegd. Hierin zijn colloïden afgebeeld naast een menselijke haar, wat een meer intuïtief beeld van de schaal geeft. Atomen zijn op een dergelijk plaatje onzichtbaar, omdat ze te klein zijn. Het oppervlak van de sinaasappel daarentegen zou vlak lijken, zoals de aarde vlak lijkt voor wie erop loopt.

130

Kijkend naar de getallen hierboven kunnen we wel zeggen dat colloïden zich qua grootte vrijwel precies tussen atomen en sinaasappels in bevinden. Daarbij combineren ze de eigenschappen van beiden: Net als sinaasappels zijn ze gemakkelijk te observeren doordat ze veel groter zijn dan atomen. Ondanks hun grootte vertonen ze echter nog wel in grote lijnen hetzelfde gedrag als de allerkleinste deeltjes. Zo kunnen ze eindeloos door een vloeistof heen dwarrelen als "opgeloste" stoffen, daar waar sinaasappels meteen aan het oppervlak zouden gaan drijven. Door deze eigenschappen zijn colloïden een soort modelatomen geworden: ze gedragen zich als atomen, maar zijn toch relatief makkelijk te bestuderen. Ook voor studies van kristallen geldt dit. Als colloïden in hoge concentraties in een vloeistof worden gebracht of als er een aantrekkingskracht is tussen de colloïden, dan kunnen ze spontaan kristalliseren. Deze colloïdale kristallen, met eigenschappen die sterk op atomaire kristallen zoals metalen lijken, kunnen vervolgens met een microscoop nauwkeurig bestudeerd worden.

Zoals beschreven bestaan kristallen uit repeterende structuren. Als de positie van de eerste bouwstenen bekend is kan de structuur van de rest van het kristal uitgerekend worden. Als dit zo is, waarom is het dan interessant om kristallen onder een microscoop te bekijken? We kunnen immers ook gewoon uitrekenen hoe ze eruit zien. Een van de redenen hiervoor is het bestaan van roosterfouten, het laatste begrip uit de eerste zin van deze samenvatting. Roosterfouten zijn onvolkomenheden die in elk kristal voorkomen. Zelfs de meest pure materialen bevatten van nature een kleine concentratie roosterfouten, ook wel defecten genoemd. Roosterfouten komen voor in allerlei soorten en maten. De simpelste hiervan zijn weer terug te voeren op de marktkoopman, maar in dit geval een die onbetrouwbaar is. In de kistjes met netjes gestapelde sinaasappels heeft hij uit het binnenste van de stapeling een sinaasappel verwijderd. Zo lijkt het een perfect kistje sinaasappels, maar in feite ontbreekt er één. In wetenschappelijke termen heet dit een vacature. In colloïdale kristallen kan wel een op de honderd plekken een vacature bevatten. Naast vacatures bestaan er vele soorten roosterfouten waar de marktkoopman nog een puntje aan kan zuigen. Vele zijn zo complex dat het lastig is in te zien hoe ze precies gestapeld zijn. Een voorbeeld hiervan is terug te vinden in hoofdstuk 1, figuur 1.1 of 1.2.

Het belang van roosterfouten ligt in hun invloed op de eigenschappen van kristallijne materialen. Zo kunnen computerchips bijvoorbeeld niet functioneren zonder zorgvuldig aangebrachte roosterfouten. Aan de andere kant kan één enkele verkeerd aangelegde fout een chip waardeloos maken. Op een soortgelijke manier spelen roosterfouten een rol in het bepalen van bijvoorbeeld de hardheid van metalen en de kleur en waarde van edelstenen. Voor studies van dit soort roosterfouten kunnen colloïdale kristallen de rol van modelstructuur vervullen, waarbij de grootte van de deeltjes de visualisatie van roosterfouten vergemakkelijkt.

Figure 10.3. Typisch resultaat van een SAXS-meting aan een colloïdaal kristal

Daarnaast hebben colloïdale kristallen zelf ook interessante optische eigenschappen die goed te zien zijn in opalen. De kleuren die zo karakteristiek zijn voor deze edelstenen worden veroorzaakt door de kristallijne stapeling van colloïden. Deze bijzondere optische eigenschappen, nagemaakt in synthetische opalen, kunnen van belang kunnen zijn voor betere zonnecellen, glasvezelcommunicatie en efficiënte verlichting. Ook in deze structuren spelen roosterfouten een grote rol en is het van belang kennis te vergaren over de eigenschappen hiervan.

Nu de eerste zin van de samenvatting hopelijk een stuk duidelijker is geworden, wil ik hoofdstuk voor hoofdstuk dieper ingaan op de stof.

Hoofdstuk 1 bevat een uitgebreide introductie over colloïdale kristallen, roosterfouten en gebruikte meettechnieken.

Hoofdstuk 2 tot en met 5 bespreken studies die gedaan zijn met behulp van röntgentechnieken. Hoewel hierboven het belang van de grootte van colloïden voor het doen van waarnemingen is besproken, is het toch niet altijd mogelijk om direct met een microscoop naar de stapeling van deeltjes te kijken. Dit kan zijn omdat de colloïden gemaakt zijn van materialen die licht sterk absorberen of verstrooien of omdat de deeltjes toch net te klein zijn om in een microscoop te kunnen zien. In zulke gevallen kunnen röntgentechnieken uitkomst bieden. Hierbij maken we onderscheid tussen verstrooiingsexperimenten (ook wel small angle

X-ray scattering of SAXS genoemd) en röntgenmicroscopie.

Hoewel verstrooiingsexperimenten niet geschikt zijn om direct naar de structuur van de deeltjes te kijken, zijn ze uitermate geschikt om de langeafstandsstructuur van een kristal te onderzoeken. Figuur 10.3 bevat een voorbeeld van een SAXS meting. De afstand tussen het midden van het plaatje en de eerste pieken geeft ons informatie over de gemiddelde afstand tussen de deeltjes in het kristal en de ordening van de pieken geeft informatie over de kristalstructuur. De intensiteit en de breedte van de pieken bevatten informatie over de foutenstructuur in het kristal. Zoals eerder besproken is het in een perfect kristal mogelijk om vanuit de positie van een klein aantal deeltjes de posities van alle andere deeltjes uit te rekenen. Hoe groter een perfect kristal is, hoe scherper en intenser de diffractiepieken worden. Roosterfouten verstoren de perfecte structuur van een kristal en zorgen voor een verbreding van de pieken en een daling van de intensiteit. Ook de strepen in de figuur worden door roosterfouten veroorzaakt.

In hoofdstuk 2 is de bruikbaarheid van SAXS voor het bepalen van de stapelstructuur in colloïdale kristallen onderzocht. Zelfs bij het gebruik van hoogenergetische röntgenstralen, die normaliter weinig interactie met materie zouden moeten hebben, werden effecten van meervoudige verstrooiing gemeten. Dit betekent dat enkele röntgenfotonen meer dan één maal verstrooid worden in een kristal, waardoor ze fantoomeffecten veroorzaken die interpretatie van de metingen kunnen bemoeilijken. Nader onderzoek naar het effect van meervoudige verstrooiing op de data-interpretatie wees echter uit dat dit te verwaarlozen is.

In hoofdstuk 3 werd vervolgens met SAXS gekeken naar de structuur van gedroogde colloïdale kristallen. In deze kristallen zijn twee stapelingen van deeltjes mogelijk: De kristallijne lagen zoals die in figuur 10.1 zijn weergegeven kunnen in een ABABAB patroon of in een ABCABC patroon gestapeld worden. In het eerste geval liggen de deeltjes in de derde laag exact boven de deeltjes in de eerste laag en heeft de laag daartussen een andere positie. Dit heet de hexagonale dichtste stapeling (in het Engels afgekort tot hcp). In het andere geval heeft de vierde laag dezelfde positie als de eerste en hebben de twee lagen ertussen beide een andere positie. Dit wordt de vlakgecentreerd kubische stapeling genoemd (fcc in het Engels).

De kristallen die in hoofdstuk 3 onderzocht zijn lijken over het algemeen een fcc structuur te hebben, wat gunstig is voor de optische eigenschappen. Onze SAXS metingen toonden echter aan dat 10% van de structuur bestaat uit lagen met hcp pakking, ook wel stapelfouten genoemd. Dit verslechtert de optische eigenschappen aanzienlijk.

Zoals aangegeven is SAXS een methode om naar de langeafstandsstructuur van kristallen te kijken. Om een oorzaak te vinden voor het groeien van stapelfouten is het nodig om naar individuele fouten te kijken op een schaal van
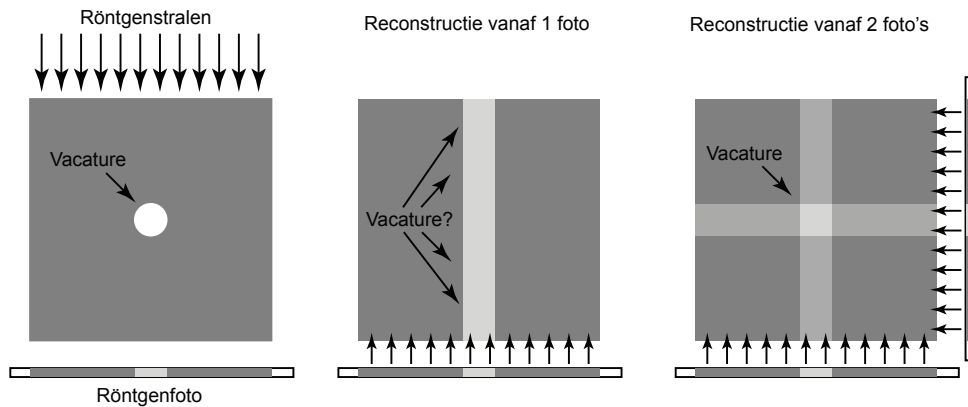
133

Figure 10.4. Illustratie hoe de positie van een ontbrekende sinaasappel (ronde stip links) kan worden bepaald door middel van twee röntgenfoto's onder een hoek van 90 graden met elkaar. Met een enkele foto is de positie niet exact te bepalen.

enkele deeltjes. Aangezien dit met SAXS niet mogelijk is en gedroogde kristallen met lichtmicroscopie niet te onderzoeken zijn, zijn in hoofdstuk 4 experimenten met röntgenmicroscopie gedaan. Studies aan colloïdale kristallen met behulp van röntgenmicroscopie kunnen worden vergeleken met röntgenfoto's van een stapel sinaasappelen. Als een marktkoopman zo oneerlijk geweest is om in een kratje sinaasappelen een vacature te creëren door een sinaasappel uit het binnenste te verwijderen, kan de oplettende koper een miskoop voorkomen door een röntgenfoto te maken waarop het ontbreken van de sinaasappel wordt aangetoond. Op eenzelfde manier is in hoofdstuk 4 onderzocht of kristalstructuren en roosterfouten in colloïdale kristallen kunnen worden aangetoond met behulp van röntgenstraling. Voor dunne kristallen, die bestaan uit maximaal drie lagen bleek deze methode heel geschikt.

Om dikkere kristallen te onderzoeken, wat meestal gewenst is, is het nodig de techniek aan te passen. Een dik kristal kan vergeleken worden met een pallet vol met sinaasappelkistjes, waarin één sinaasappel mist. Een röntgenfoto hiervan zal weliswaar aan het licht brengen dat er ergens op het pallet een sinaasappel ontbreekt, maar of dit in het voorste of in het achterste kratje is, kan niet met zekerheid gezegd worden. Ook in de medische wetenschap is een enkele röntgenfoto vaak niet genoeg om alle informatie te geven die een arts nodig heeft. Op een gewone röntgenfoto is immers niet te zien of iemands ribben zich voor of achter zijn ruggengraat bevinden. Om toch diepte-informatie te kunnen krijgen is de CT-scan ontwikkeld. Hierbij worden vanuit een heleboel hoeken röntgenfoto's van iemand gemaakt, waaruit dan een driedimensionaal beeld van de inwendige mens kan worden berekend. Om terug te gaan naar de sinaasappels: als er een tweede foto van de zijkant van het pallet wordt genomen, is de positie van de

verdwenen sinaasappel exact te bepalen, zie figuur 10.4.

In hoofdstuk 5 wordt een soortgelijke techniek gebruikt om informatie over de inwendige structuur van gedroogde colloïdale kristallen te verzamelen. Omdat deze kristallen veel meer onregelmatigheden bevatten dan een enkele vacature is het nodig om vanuit meer dan twee hoeken metingen te doen. Door middel van 41 metingen onder verschillende hoeken kon voor het eerst de interne structuur van gedroogde colloïdale kristallen van 8 lagen dik worden bepaald, inclusief roosterfouten.

In hoofdstuk 6 wordt dieper ingegaan op de structuur van één specifieke type roosterfout: de dislocatie. De dislocatie is een van de meest bepalende roosterfouten waar het de mechanische eigenschappen van een kristal betreft. Metaalmoeheid wordt bijvoorbeeld onder andere door dislocaties veroorzaakt en ook de hardheid van een metaal wordt mede bepaald door dislocaties.

In deze studie is overgeschakeld van röntgentechnieken naar optische microscopie, waarmee direct naar de interne structuur van de hier gebruikte colloïdale kristallen kan worden gekeken. Door kristallen te groeien van warmtegevoelige colloïden, die krimpen bij verhitting, kon het gedrag van dislocaties als functie van temperatuur bepaald worden. Hierbij werd gevonden dat het kristal sterk verhardt bij verhitting, door een sterkere afstoting tussen de deeltjes als deze krimpen. De metingen kwamen kwalitatief overeen met de 70 jaar oude Peierls theorie die onder meer ook de sterkte van een kristal verbindt aan het gedrag van dislocaties. Een experimentele bevestiging van deze relatie is echter nooit gevonden en is door de metingen in hoofdstuk 6 een stukje dichterbij gekomen.

De laatste twee hoofdstukken bespreken de groei van stapelfouten in kristallen gegroeid van sedimenterende bollen. In hoofdstuk 7 wordt een mechanisme besproken waarbij stapelfouten die onder een hoek van 70 graden met het substraat in het kristal groeien de kristalstructuur beïnvloeden. Van dit groeimechanisme is in hoofdstuk 8 gebruik gemaakt om stapelfouten in kristallen te groeien op vooraf bepaalde posities door middel van substraatsjablonen. Door in een substraat regelmatige patronen te etsen die een structuur hebben die vergelijkbaar is met een kristalvlak, is de groei van een vooraf bepaalde structuur aan een kristal op te leggen. Door middel van deze sjablonen was het mogelijk stapelfouten te groeien, maar ook holle kanaaltjes op plekken waar twee stapelfouten door elkaar heen groeiden. In de toekomst kunnen dergelijke structuren mogelijk gebruikt worden als kanaaltjes voor lichtgeleiding.

Acknowledgements

Acknowledgements

Four years of research crammed into a little booklet. Thousands of hours of work carefully written down in eight chapters. Yet the most important part of this booklet is contained in the next few pages. Without the people mentioned here, my thesis would probably have consisted of blank pages.

I would like to start with my daily supervisor and co-promotor Andrei. Andrei, as your first PhD student, the start of my project was new to both of us. I very much appreciated your dedication and your close involvement in my project. Our joint trips to ESRF and the European Crystallographic Meeting not only served to further science, but were also great occasions to get to know you personally. Thank you for the past four years.

I would also like to thank my promotor, Henk Lekkerkerker, for giving Andrei and myself lots of confidence and freedom in choosing the direction of my research.

In the long list of people that have contributed to the scientific content of this thesis, special thanks go to Matti van Schooneveld. Matti, ever since we started working as "comrades in glass" during the research for our Master's thesis, I have enjoyed working with you. Researching the nanoworld together was always as much stimulating as it was fun. The fact that experiencing loads of dark counts in combination with pickled eggs and sleep deprivation turned out to be one of the highlights of my time as a PhD student is testimony to that.

The research presented in chapter 8 would not have been possible without Matthijs de Winter. The enthusiasm with which you took up the challenge of yet another materials scientist who wanted to use the dual beam setup was contagious. I enjoyed our days at the setup, trying to think of the best structures to burn into the templates. I also want to thank Jan Andries Post for enabling us to use this constantly overbooked setup.

For further scientific contributions to this thesis, I want to thank Michiel Hermes, Matthieu Marechal, Marjolein Dijkstra, Alfons van Blaaderen, Frank de Groot, Willem Kegel, Emiel de Smit, Chris Rétif, Anatoli Snigirev, Vera Abramova, Alexander Sinitskii and Volkert de Villeneuve.

For various forms of technical assistance in the Van 't Hoff lab, my thanks go to Emile, Bonny, Dominique and Kanvaly. Emile for any PC troubleshooting, Bonny for technical expertise on anything, Dominique and Kanvaly for lab related issues.

A large debt of gratitude goes out to the students that I have supervised over the years. Although not all of the results have been taken up in this thesis, all projects have contributed to the contents in one way or another. First year students Paul and Katinka and second year students Hedwich, Simone, Nico, Teun, Arnoud, Casper and Richard, you all showed that a small group of students can make significant

137

Acknowledgements

scientific progress in a short amount of time. Michiel, as my first bachelor student your project was as much a jump into the unknown for me as it was for you. The way you made measuring particle sizes in iTEM look like a fun pastime still brings a smile to my face. Sandy, your project under my joint supervision with Daniela was a small sidestep of little relevance to my thesis. This did not make it any less enjoyable. Your enthusiastic, hard work and thorough experimentation have resulted in new insights, a new colloidal model system and a very nice paper. I guess your goodbye present to Daniela and me has gained us both a few kilos and it pains me to say that I recently clumsily destroyed it… Jan-Willem, although I was never your official supervisor, I ended up being quite involved in your project. Thank you for your contributions to my thesis. Joost, your Master's project has been invaluable to the realization of chapters 7 and 8. Progress was never easy, but your persistence has resulted in a sizeable heap of useful data. Aside from fruitful, it was also fun to supervise you and I am therefore happy to have had you as a colleague after your graduation.

Many chapters in this thesis contain data collected at synchrotrons. Handling the equipment at these facilities is no easy task. I would therefore like to thank the personnel of the BM-26B DUBBLE and ID-11 beamlines at the European Synchrotron Radiation Facility, X07DA PolLux at the Swiss Light Source and 10ID-1 soft X-ray spectromicroscopy beamline at the Canadian Light Source for excellent assistance. Beam trips were always a fun experience, with long working days/nights, short resting nights/days and bad food. Luckily this was all compensated by good company. For this I would like to thank, in order of appearance, Dannis, Johan, Arnout, Vera, Alexander, Esther, Anke, Luis and Inez. Special thanks go to Dima for company, expertise and hiking at every ESRF trip.

A bit closer to home, the temperate zone of the Kruyt north wing was made a better place by my N731 officemates. Again in order of appearance: Volkert, Daniela, Raja, Janne-Mieke, Jaakko and Bas. Aside from the frequent scientific discussions, I enjoyed saving English-speaking-money for a moka pot, eating loads of candy, spending the English-speaking-money-that-should-have-been-spent-on-a-moka-pot on candy, speaking German and only German, Rock & Roll hours and many other things. Thanks for all that!! Outside of that, I want thank the whole of the fcc group for breaks, borrels, whisky nights, new year's dinners and after-borrel wife burgers.

The final thank yous and last paragraphs of this thesis are reserved for my friends and family. My paranymphs Bart and Mikal (thanks for suiting up with me), Loek, Emiel, Yorick, thanks for the fishing, snooker, brewing, movie nights, NK's shuffleboard, alternatief carnaval, festivals, concerts, nekschoten. Looking forward to many more of those in the future!!!

Oscar, Remi, Maarten I "de echte", Maarten II "de andere", Werner, Coen, Jelle,

a similar list applies here, with some overlap. Late autumn canoeing, ribs, minigolf spelunking, ribs, waking up to cowboyhats and Krezip, ribs, ribs, ribs, visits to Groningen and Starlet (slow-)racing are among the absolute highlights of the past four years. Thanks for keeping it real!

Tamara, thank you for the past years.

Maarten (I or II, you'll have to settle that with II or I), I have already thanked you a few lines earlier, but want to thank you here again for your being-a-brother for the past 29 years. Hanna, I have also thanked you already for your contribution to the scientific part of this thesis (who would have guessed), but your contributions outside of chemistry have been way more important in the past four years. Thank you for that.

Pa & ma, I don't even know where to start. Digging back into my first memories, you were already giving guidance to my rather destructive inquisitive nature. Your unconditional support, love and confidence have brought me to where I am now and for that I cannot thank you enough.

Resume

Jan Hilhorst was born on November 10th 1982 in Haarlem, the Netherlands. In 2001 he graduated from secondary school at the Gemeentelijk Gymnasium in Hilversum and in the same year ranked 3rd in the Dutch National Chemistry Olympiad. He proceeded to study chemistry at Utrecht University. He obtained his Bachelor's degree in late 2005, with a Bachelor's thesis on infrared spectroscopy on the adsorption of oleic acid on magnetite nanoparticles. This research was performed in the Van 't Hoff Laboratory for Physical and Colloid Chemistry under dr. Ben Erné.

Also in 2005, he started his Master's thesis in the condensed matter and interfaces group under prof. dr. Andries Meijerink and prof. dr. Daniël Vanmaekelbergh. The topic of this thesis was the synthesis of nanophotonic architectures built from quantum dots, silica and metal nanoparticles. After this, in 2007, he spent six months at the Ludwig-Maximilians-Universität in Munich, Germany for a short research project on fluorescence energy transfer in clustered dispersions of semiconductor quantum dots under dr. Andrey Rogach. He obtained his Master's degree *Cum Laude* in November 2007.

In that same year he started as a Ph.D. student in the Van 't Hoff Laboratory for Physical and Colloid Chemistry under dr. Andrei Petoukhov and prof. dr. Henk Lekkerkerker. This thesis comprises the results of his work as a Ph.D. student. From July 2008 to March 2011 he was a member of the Debye Ph.D. Committee, an organization representing all Ph.D. students in the Debye Institute for Nanomaterials science at Utrecht University.